



THEORETICAL STUDIES ON TRANSITION METAL CATALYZED CARBON DIOXIDE FIXATION

Fernando Simón Castro Gómez

ADVERTIMENT. L'accés als continguts d'aquesta tesi doctoral i la seva utilització ha de respectar els drets de la persona autora. Pot ser utilitzada per a consulta o estudi personal, així com en activitats o materials d'investigació i docència en els termes establerts a l'art. 32 del Text Refós de la Llei de Propietat Intel·lectual (RDL 1/1996). Per altres utilitzacions es requereix l'autorització prèvia i expressa de la persona autora. En qualsevol cas, en la utilització dels seus continguts caldrà indicar de forma clara el nom i cognoms de la persona autora i el títol de la tesi doctoral. No s'autoritza la seva reproducció o altres formes d'explotació efectuades amb finalitats de lucre ni la seva comunicació pública des d'un lloc aliè al servei TDX. Tampoc s'autoritza la presentació del seu contingut en una finestra o marc aliè a TDX (framing). Aquesta reserva de drets afecta tant als continguts de la tesi com als seus resums i índexs.

ADVERTENCIA. El acceso a los contenidos de esta tesis doctoral y su utilización debe respetar los derechos de la persona autora. Puede ser utilizada para consulta o estudio personal, así como en actividades o materiales de investigación y docencia en los términos establecidos en el art. 32 del Texto Refundido de la Ley de Propiedad Intelectual (RDL 1/1996). Para otros usos se requiere la autorización previa y expresa de la persona autora. En cualquier caso, en la utilización de sus contenidos se deberá indicar de forma clara el nombre y apellidos de la persona autora y el título de la tesis doctoral. No se autoriza su reproducción u otras formas de explotación efectuadas con fines lucrativos ni su comunicación pública desde un sitio ajeno al servicio TDR. Tampoco se autoriza la presentación de su contenido en una ventana o marco ajeno a TDR (framing). Esta reserva de derechos afecta tanto al contenido de la tesis como a sus resúmenes e índices.

WARNING. Access to the contents of this doctoral thesis and its use must respect the rights of the author. It can be used for reference or private study, as well as research and learning activities or materials in the terms established by the 32nd article of the Spanish Consolidated Copyright Act (RDL 1/1996). Express and previous authorization of the author is required for any other uses. In any case, when using its content, full name of the author and title of the thesis must be clearly indicated. Reproduction or other forms of for profit use or public communication from outside TDX service is not allowed. Presentation of its content in a window or frame external to TDX (framing) is not authorized either. These rights affect both the content of the thesis and its abstracts and indexes.

UNIVERSITAT ROVIRA I VIRGILI
THEORETICAL STUDIES ON TRANSITION METAL CATALYZED CARBON DIOXIDE FIXATION
Fernando Simón Castro Gómez

UNIVERSITAT ROVIRA I VIRGILI

THEORETICAL STUDIES ON TRANSITION METAL CATALYZED CARBON DIOXIDE FIXATION

Fernando Simón Castro Gómez

Fernando Simón Castro Gómez

Theoretical Studies on Transition Metal Catalyzed Carbon Dioxide Fixation

Ph.D. Thesis

Supervised by Prof. Carles Bo Jané



UNIVERSITAT ROVIRA I VIRGILI



Tarragona

September 2014

UNIVERSITAT ROVIRA I VIRGILI

THEORETICAL STUDIES ON TRANSITION METAL CATALYZED CARBON DIOXIDE FIXATION

Fernando Simón Castro Gómez



ICIQ – Institut Català d'Investigació Química
Av. Països Catalans, 16
43007 Tarragona (Espanya)



**UNIVERSITAT
ROVIRA I VIRGILI**

DEPARTAMENT DE QUÍMICA FÍSICA
I INORGÀNICA

Campus Sescelades
Marcel·lí Domingo, s/n
43007 Tarragona
Tel. +34 977 55 81 37
Fax +34 977 55 95 63
www.quimica.urv.es

Carles Bo Jané, Profesor titular de Química Física del departament de Química Física i Inorgànica de la Universitat Rovira i Virgili, y líder de grupo del Institut Català d'Investigació Química.

HAGO CONSTAR:

Que el presente trabajo, titulado “Theoretical Studies on Transition Metal Catalyzed Carbon Dioxide Fixation”, que presenta el Sr. Fernando Simón Castro Gómez para la obtención del título de Doctor en Química, ha sido realizado bajo mi dirección en mi grupo de investigación del Institut Català d'Investigació Química y que cumple los requisitos para optar a la Mención Europea.

Tarragona, septiembre de 2014

Prof. Carles Bo Jané

UNIVERSITAT ROVIRA I VIRGILI

THEORETICAL STUDIES ON TRANSITION METAL CATALYZED CARBON DIOXIDE FIXATION

Fernando Simón Castro Gómez

Agradecimientos

A pesar de que la frase resulte muy trillada, esta es sin duda la parte más difícil de la redacción de la tesis. Hay muchas personas a quién agradecer, muchas vivencias que resaltar, muchas anécdotas que contar, pero muy poco espacio para plasmarlo en estas cuantas páginas.

Empiezo por agradecer a Dios por haberme regalado esta bonita oportunidad de alcanzar un sueño más en mi vida. Estar redactando estas líneas es prueba fehaciente de su infinita voluntad.

En un plano más terrenal, deseo hacer una mención muy especial y llena de muchos agradecimientos a Carles Bo Jané por haberme introducido en el inquietante mundo de la catálisis homogénea computacional y brindarme la oportunidad de realizar esta tesis doctoral bajo su dirección. Gracias por sus consejos, su paciencia, dedicación y por enseñarme a ver la vida desde otra perspectiva.

Agradezco al Institut Català d'Investigació Química (beca n. 14/10) y al Ministerio de Economía y Competitividad (beca BES-2012-058448) por el financiamiento de esta tesis doctoral a través del proyecto CQT2011-29054-C02-02.

I would like to thank Prof. Gunnar Nyman for his hospitality in his group at University of Gothenburg during my three months research visit in the last summer of 2013. Special thanks to my friend Chamil Sameera for his kindness, teachings, hospitality and uncountable support from him and his family during my short stay in Gothenburg.

Muchas gracias a los profesores Feliu Maseras, Núria López, Arjan Kleij y Rosa Caballol por su ayuda, sus sugerencias, grandes aportes y buenos momentos durante el desarrollo de mi tesis.

Un agradecimiento muy especial lo merece la súper-secre Núria Vendrell por su incalculable ayuda y sobre todo por facilitarme la vida en el tema burocrático del ICIQ, la URV y demás. También agradecer a Martín Gumbau por su constante ayuda en la parte informática y por enseñarme a como “piratear” las cápsulas de la cafetera para poder disfrutar cada día del mejor café del mundo (el colombiano, sin duda). Igualmente, agradezco a Moisés Álvarez por su ayuda en la parte de programación.

Muchas gracias a las jermus y manes del ICIQ por los buenos momentos vividos en el aspecto académico, fiestero, por las bromas, por hacer famosa *el serrucho* en Europa, los incontables grupos de whatsapp, etc: Neyvis Almora (si me exprimes te doy juguito), Dolores Melgar (la jermu futbolera), Maria Besora, Rositha Kuniyil, Elena de Orbe, Miquel García (el presidente del género), Max García (el man del perro paseador), Giuliano Carchini, Guillem Revilla (el man sin frío), Ignacio Funes (el chef), Joan González (mi mindundi, visca Catalunya lliure), Luca Bellarosa (en Barranquilla se baila así), Nuno Bandeira (por cuidarme el coche), Marçal Capdevila (el vice), Víctor Fernández (el man de los torrents), Oier Lazuntza (un verdadero ejemplo de vida), Rodrigo García (el español de las dos solitarias), Marcos Rellán (y su tacto con las mujeres), Xavi Sanz (el perseguidor de TSs), Qiang Li, Charles Goehry, Adiran De Aguirre y Sergey Pogodin. También a los antiguos: Cristina Pubill, Crisa Vargas, Chunhui Liu, Laura Mateus, Ruth Dorel, Laura Estévez, Ainara Nova, Abel Locati (el man del parajo), Mickael Gicquel (el francés salsero y con tumbao blanco), Giovanni Salassa (el verdadero italiano tumba locas, gracias por tu hospitalidad en Italia y las aventuras con el Dr. Gicquel), Chamil Sameera (y su *dark side*), Jesús Jover, Alex Hamilton, Torstein Fjermestad, Adrià Gil, Gerard Novell y Maxime Mercy; por último a los más recientes, pero no menos importantes, Pablito Garrido (el mondadoso), Martica López, Víctor Laserna, Ifunes y Helenica Hernández.

Una mención muy especial la merece mi primer mentor, José Cotuá Valdes, por sus sabios consejos de vida, su amistad y por haberme persuadido con la idea de hacer un doctorado desde que hice mis primeros pininos en Química Computacional en el Grupo Max Planck de la Universidad del Atlántico.

No podía pasar por alto a toda la people elegante que he conocido en Tarragona durante estos años: Magdita Megret (la cubanita que pone el sabor en la *Isla del Mojito* junto a Ramón Masdeu), Mireia Fajardo (la propia Mire), Marina Buendia (la cata bacana), Neus Segura, Ruthcilla, Gloria Alves, Vero Suescún, Normita Peña (la propia Cataleia, la negra del swing, mi chófer favorita :P), Carlos Amaris, Isa Sánchez, Carito Blanco, Tatiana Sánchez, Judith Granados, Isabel Clua (un especial agradecimiento por toda tu ayuda y los buenos momentos vividos), María C. Jaramillo, Andry Cera (el bachatero de moda), las hermanas Castañeda, Iván Tovar y Javier Burgos. Muchas gracias a todos y cada uno que

han aportado con su granito de arena o que bien, han contribuido a que me estancia durante estos cuatro años en Tarragona haya sido genial y llena de muy gratos momentos.

A mi gran amigo y hermano Pedro Castro (el propio Peter), al viejo Alejo Jiménez y a mis compaes firmes terminados en “ón de ...”, Jhon Zapata (el aprendiz del Sensei), Ramón Valencia (el Sensei), Miguel A. Marimón (el bombardero); así como a mis compaes de Barcelona, Jorge Alí, Hansel Gómez, Francisco *pacho* Zarur y Arelita Flores con su Nalita.

Los agradecimientos ahora van para mis grandes amigos del “otro lado del charco”: los de la UA, Aminta Rachel, Argelia *yeya* Rada, Neiris Cárcamo, Dianita Camacho, Karen Moon, Diana Márquez, Evelyn Benavides, Gina Domínguez, mi Tati Sugey, Gina Martínez, Cindy y Nubia Florez, Lia Marcela, Jenny Ortiz, Magalis Silvera, Sandra Moreno, Everyn Escalante, Laura Paternina, Marla Carmen, Lina Hernández, Ivette Acevedo, Lina Paola, Everlys Espitia, Giovanna Medina, Dignora Pérez, Pedro González, Álvaro Gómez, Daniel Sarmiento, Erwin Guzmán, Saúl Ortega, Boris Marchena, Leo Mendoza, Alejo Jiménez, Iván Herrera, y Eric Zayas; a mis apreciados profesores de la UA, en especial a José Meza, Catalino de la Rosa, Gustavo Andrade, Roberto Hernández, Nurys Rebolledo, Katherine Torres y Clara Vargas Lascarro; a mis amigos del INEM, especialmente a mi hermanazo Roberto García y Marleydis De la Hoz; a mis amigos del INVIMA, Goyo Torres, Deisy Lozano, Diana Charry, Sofía Laverde, Adriana Ortiz, Diana Garzón, Eduardo Vergel, Gina A. Díaz, Zulma Valbuena y Carolina Rodríguez; a mis grandes amigos Fab Altahona y Jean Carlos Patiño, la vieja Vero Altahona, mi comadre y amiga Yenifer Llamas, Luzma Bolívar, Adriana *nany* Iglesias, Rox De las Salas, Roberto González y Andersson Olivo; a las familias Calderón Miranda, Cárdenas Orozco, Moreno Gastelbondo y Martínez Crespo.

Esta última parte de los agradecimientos la dedico a toda mi familia, en especial a esas personas a quienes les debo la vida, mi formación personal y profesional, a esos que nunca me alcanzará esta vida ni la otra para agradecer todo lo que han hecho por mí durante todos estos años, esos son mis padres amados, Ruth Mery Gómez y Fernando Casto; a mis hermanitas Keidy y Maye, mis sobrinitos Gianlu y Anto, mi segundo padre Hernán Gómez, mis primos hermanos Blady, Yenis, Dolceys y Mildred, a Gina Sánchez, Mario Montero, Lida Patiño, a todos mis tíos, tías, primos, primas, mis desaparecidos abuelos y tíos, y demás familiares. Zuleima Yanira, mi reina, a ti gracias por ser la musa de mi inspiración, por brindarme tu apoyo incondicional, y sobre todo por tu amor y comprensión.

UNIVERSITAT ROVIRA I VIRGILI

THEORETICAL STUDIES ON TRANSITION METAL CATALYZED CARBON DIOXIDE FIXATION

Fernando Simón Castro Gómez

Funding Agencies



Generalitat de Catalunya
**Departament d'Economia
i Coneixement**



**Agència
de Gestió
d'Ajuts
Universitaris
i de Recerca**



**EXCELENCIA
SEVERO
OCHOA**

UNIVERSITAT ROVIRA I VIRGILI

THEORETICAL STUDIES ON TRANSITION METAL CATALYZED CARBON DIOXIDE FIXATION

Fernando Simón Castro Gómez

List of publications

Related with this thesis

“Structural Studies of Metal Ligand Complexes by Ion Mobility-Mass Spectrometry”, Victoria E. Wright, Fernando Castro-Gómez, Ewa Jurneczko, James C. Reynolds, Andrew Poulton, Steven D. R. Christie, Perdita Barran, Carles Bo, Colin S. Creaser, *International Journal for Ion Mobility Spectrometry* **2013**, *16*, 61–67.

“Structural Studies of Catalytic Reaction Intermediates by Ion Mobility-Mass Spectrometry”, Victoria E. Wright, Fernando Castro-Gómez, Ewa Jurneczko, James C. Reynolds, Andrew Poulton, Steven D. R. Christie, Perdita Barran, Carles Bo, Colin S. Creaser, *submitted*.

“A DFT Study on the Mechanism of the Cycloaddition Reaction of CO₂ to Epoxides Catalyzed by Zn(Salphen) Complexes”, Fernando Castro-Gómez, Giovanni Salassa, Arjan W. Kleij, Carles Bo, *Chemistry - A European Journal* **2013**, *19*, 6289–6298.

“Highly Active Aluminium Catalysts for the Formation of Organic Carbonates from CO₂ and Oxiranes”, Christopher J. Whiteoak, Nicola Kielland, Víctor Laserna, Fernando Castro-Gómez, Eddy Martin, Eduardo C. Escudero-Adán, Carles Bo, Arjan W. Kleij, *Chemistry - A European Journal* **2014**, *20*, 2264–2275.

“Towards Quantitative Evaluation of the Aluminium Catalyzed Formation of Cyclic Carbonates from CO₂ and Epoxides”, Fernando Castro-Gómez, W. M. C. Sameera, Gunnar Nyman, Arjan W. Kleij, Carles Bo, *manuscript in preparation*.

“Aluminium Catalyzed Copolymerization of CO₂ and Cyclohexene Oxide”, Fernando Castro-Gómez, Joan González-Fabra, Arjan W. Kleij, Carles Bo, *manuscript in preparation*.

Not related with this thesis

“Efficient Al(III) Catalyzed Formation of Biorenewable Polycarbonates using CO₂ as Molecular Building Block”, Leticia Peña Carrodegas, Fernando Castro-Gómez, Joan González-Fabra, Carles Bo, Arjan W. Kleij, *manuscript in preparation*.

UNIVERSITAT ROVIRA I VIRGILI
THEORETICAL STUDIES ON TRANSITION METAL CATALYZED CARBON DIOXIDE FIXATION
Fernando Simón Castro Gómez

*“He aprendido que el mundo quiere vivir en la cima de la montaña, sin saber
que la verdadera felicidad está en la forma de subir la escarpada”*

—Gabriel García Márquez

UNIVERSITAT ROVIRA I VIRGILI
THEORETICAL STUDIES ON TRANSITION METAL CATALYZED CARBON DIOXIDE FIXATION
Fernando Simón Castro Gómez

Contents

Chapter 1: General Introduction	1
1.1 Catalysis: basic concepts and quantification of the activity	3
1.2 Carbon dioxide fixation	6
1.2.1 Environmental perspective	6
1.2.2 Carbon dioxide as chemical feedstock	7
1.2.3 Mechanistic aspects of the catalyzed CO ₂ fixation	9
1.3 Ion mobility mass spectrometry (IM-MS)	12
1.3.1 Basic concepts	12
1.3.2 IM-MS instrumentation	14
1.4 Aims and outline	17
1.5 References and notes	20
Chapter 2: Theoretical Background	23
2.1 Introduction	25
2.2 Ab initio wave function-based methods	26
2.2.1 Hartree-Fock method	27
2.2.2 Basis functions	29
2.3 Density functional theory	30
2.3.1 The Hohenberg-Kohn theorems	30
2.3.2 The Kohn-Sham method	32
2.3.3 The local density approximation (LDA)	34
2.3.4 The generalized gradient approximation (GGA)	35
2.3.5 The meta generalized gradient approximation (m-GGA)	35
2.3.6 The hybrid generalized gradient approximation (H-GGA)	36
2.4 Methods used for including dispersion into DFT calculations	36
2.4.1 Parameterized dispersion correction by Truhlar: Minnesota functionals	37
2.4.2 Empirical dispersion correction by Grimme	37
2.5 Potential energy surface (PES)	39
2.6 Thermodynamic properties	40
2.6.1 Ensemble properties and basic statistical thermodynamics	40
2.6.2 Standard state modifications	42
2.7 Evaluation of solvent effects	44
2.8 Methods used in ion mobility mass spectrometry (IM-MS)	46
2.9 References and notes	49

Chapter 3: Structural Studies of Metal-containing Inorganic Compounds by Ion Mobility Mass Spectrometry	53
3.1 Introduction	55
3.2 Motivation	57
3.3 Objectives	58
3.4 Computational details	58
3.5 Results	59
3.5.1 Salen ligands and metallocalen complexes	59
3.5.2 Catalytic intermediates of the Stille reaction	64
3.6 Conclusions	70
3.7 References and notes	71
Chapter 4: Catalytic Formation of Cyclic Carbonates from CO₂ and Epoxides by Zn(salphen) Complexes	75
4.1 Introduction	77
4.2 Motivation	79
4.3 Objectives	80
4.4 Computational details	80
4.5 Results	81
4.5.1 The uncatalyzed CO ₂ addition reaction	81
4.5.2 The Zn(salphen) catalyzed CO ₂ addition reaction	82
4.5.3 The Zn(salphen)/NBu ₄ I catalyzed CO ₂ addition reaction	83
4.5.4 Ring-closing mechanism	89
4.5.5 The Zn(salphen)/NBu ₄ Br catalyzed CO ₂ addition reaction	91
4.5.6 Effect of epoxide substituent	91
4.5.7 Evaluation of the reaction with different DFT functionals	96
4.5.8 The Zn-N ₄ (salen)/NBu ₄ I catalyzed CO ₂ addition reaction	97
4.6 Conclusions	101
4.7 References and notes	102
Chapter 5: A Highly Active Aluminium Catalyst for the Formation of Cyclic Carbonates from CO₂ and Epoxides	107
5.1 Introduction	109
5.2 Motivation	110
5.3 Objectives	111
5.4 Computational details	111
5.5 Results	112
5.5.1 The Al-catalyst/NBu ₄ I catalyzed addition of CO ₂ to propylene oxide	112
5.5.2 The Al-catalyst/NBu ₄ I catalyzed addition of CO ₂ to 1,2-epoxyhexane	116
5.5.3 Evaluation of dispersion corrections on the Al-catalyzed reaction	118
5.5.4 Standard state corrections to the entropy in solution for the Al-catalyzed reaction	119
5.6 Conclusions	125
5.7 References and notes	126

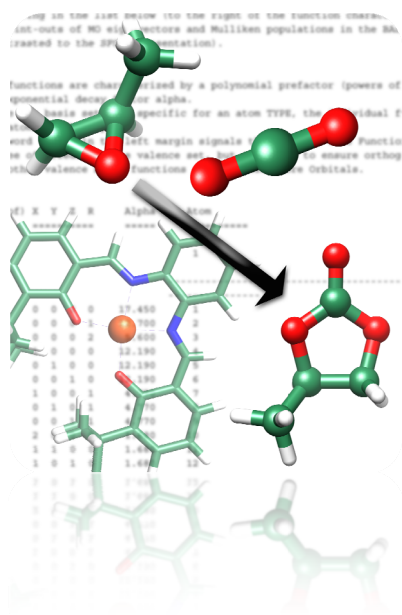
Chapter 6: Aluminum Catalyzed Copolymerization of CO₂ and Cyclohexene Oxide	129
6.1 Introduction	131
6.2 Motivation	133
6.3 Objectives	133
6.4 Computational details	133
6.5 Results	134
6.5.1 Understanding the mechanism of the copolymerization reaction	134
6.5.2 Initiation of the copolymerization reaction	136
6.5.3 Propagation of the copolymerization reaction	139
6.5.3.1 Monometallic mechanism	139
6.5.3.2 Bimetallic mechanism based on the nucleophilic attack by the oxygen Al-O	142
6.5.3.3 Bimetallic mechanism based on the nucleophilic attack by the oxygen C=O	145
6.6 Conclusions	148
6.7 References and notes	149
Chapter 7: General Conclusions	151

UNIVERSITAT ROVIRA I VIRGILI
THEORETICAL STUDIES ON TRANSITION METAL CATALYZED CARBON DIOXIDE FIXATION
Fernando Simón Castro Gómez

Chapter 1

General Introduction

Transition metal complexes have long been employed as mediators in numerous chemical processes comprising homogeneous catalysis. This chapter is devoted to make a general overview to the main issue of the present thesis: the transition metal catalyzed CO₂ fixation. In light of this, the first part of the chapter focuses on the review of some basic concepts of catalysis and the methods used to quantify the activity and efficiency of the catalytic reactions. Then, a brief description of the uses of CO₂ as renewable carbon feedstock to afford important chemicals like polycarbonates and cyclic carbonates will be presented. This section also includes an outline of the mechanistic aspects of the latter reactions and the main structural features of the catalysts used in the same. The next section contains the basic principles of ion mobility mass spectrometry (IM-MS) as a powerful technique used to provide structural information of transition metal complexes used in homogeneous catalysis. The final part will detail the main objectives and the outline of this thesis.



UNIVERSITAT ROVIRA I VIRGILI

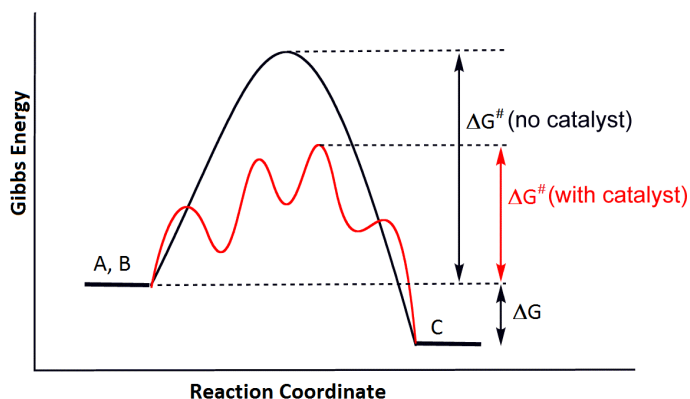
THEORETICAL STUDIES ON TRANSITION METAL CATALYZED CARBON DIOXIDE FIXATION

Fernando Simón Castro Gómez

1.1 Catalysis: basic concepts and quantification of the activity

Catalysis plays a key role in the production of most industrially important chemicals like liquid fuels and bulk and fine chemicals.^[1] The term *catalysis* was first coined by Berzelius in 1836 when he had noticed changes in substances when they were brought in contact with small amounts of certain species called “ferments”.^[2] Although Berzelius had the merit to recognize a common feature in such processes, the nature of the phenomenon was not properly understood for the next 60 years. It was Ostwald who established the *kinetic* nature of catalysis, and the definition he proposed in 1895 is the basis for the current concept of catalysis: “a catalyst is a substance that changes the rate of a chemical reaction without itself appearing into the products”. Indeed, a similar concept has been adopted by the International Union of Pure Chemistry (IUPAC), which defines catalysis as “the action of a substance (i.e., catalyst) that increases the rate of a reaction without modifying the overall standard Gibbs energy change in the reaction”. According to this, a catalyst increases the rate of the reaction without influencing on the thermodynamic equilibrium of reactants and products.

It can be seen in Scheme 1.1 that the overall reaction Gibbs free energy (ΔG) in a catalyzed reaction does not change, but the free energy of activation (ΔG^\ddagger) indeed does it.

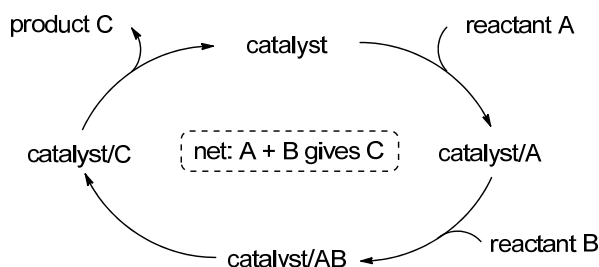


Scheme 1.1 Schematic representation of a generic reaction profile for a catalyzed (curve in red) and uncatalyzed (curve in black) chemical reaction.

For a chemical reaction to be experimentally observed, the thermodynamic and the kinetic changes should not be too unfavorable. The thermodynamic changes are measured in terms of the change in Gibbs free energy (ΔG), while the kinetic requirement is

measured by the free energy of activation (ΔG^\ddagger). A thermodynamically favorable reaction ($\Delta G < 0$) may not take place because ΔG^\ddagger may be too high. On the other hand, a thermodynamically unfavorable reaction ($\Delta G > 0$) may occur if ΔG^\ddagger is too low. The relationship between ΔG and ΔG^\ddagger is normally presented in a diagram as that depicted in Scheme 1.1, where free energies of the reactants, products, intermediates, and transition states are plotted against the reaction coordinate.

The combination of the steps involved in a catalytic reaction is commonly called a *catalytic cycle*. An example of this is shown in Scheme 1.2, in which the initial step involves binding of one or more reactants by the catalyst, and the final step is the release of the product and regeneration of the catalyst. In such Scheme is observed that the starting point of the catalytic reaction is also the ending point of the same, this is precisely what gives the name of cycle.



Scheme 1.2 Generic catalytic cycle for catalytic conversion of reactants A and B into product C.

A widely method used to measure the activity of the species involved in a catalytic cycle (catalytic species) is by calculating the reaction *rate constant* k , which in turn can be derived from the Arrhenius^[3] and van't Hoff formulations. The relationship between equilibrium constant K and free energy change in the standard state (ΔG_o) on the one hand, and *rate constant* k and energy of activation (ΔE) on the other, are given by the van't Hoff (1.1) and Arrhenius (1.2) equations, respectively.

$$\Delta G_o = -RT \ln K \quad (1.1)$$

$$k = Ae^{-\Delta E/RT} \quad (1.2)$$

For calculating the free energy of activation (ΔG_0^\ddagger) of a given reaction, the enthalpy (ΔH_0^\ddagger) and entropy (ΔS_0^\ddagger) of activation of the same reaction are calculated first. This is done by plotting $\ln(k/T)$ against $1/T$, where the slope and the intercept give the measures of ΔH_0^\ddagger and ΔS_0^\ddagger , respectively. This diagram is called an *Eyring*^[4] *plot*, and the resulting expression for the rate constant k is known as *Eyring equation*:

$$k = \frac{k_B T}{h} e^{-\frac{\Delta H_0^\ddagger}{RT}} e^{\frac{\Delta S_0^\ddagger}{RT}} \quad (1.3)$$

On the other hand, a plot of $\ln k$ against $1/T$ is, of course, the *Arrhenius plot* and is used for measuring activation energy (ΔE).

During the catalytic cycle the catalyst may be present in several intermediate forms. An active catalyst will pass a number of times through this cycle of states; in this sense the catalyst remains unaltered. The number of times that a catalyst goes through this cycle is the *turnover number* (TON), which is a measure of the efficiency of a catalytic process, and can be calculated as the total number of moles of product per mole of catalyst:

$$TON = \frac{\text{moles of product}}{\text{moles of catalyst}} \quad (1.4)$$

Other common quantity used for measuring the efficiency of a catalytic reaction is the *turnover frequency* (TOF) that is the turnover number in a certain period of time:

$$TOF = \frac{TON}{\text{time}} \quad (1.5)$$

The calculation of TOFs from a theoretically obtained energy profile was not a straightforward process until few years ago when Kozuch and Shaik introduced the so-called *energetic span model*.^[5] The formulation of this model is based on *Eyring's transition state theory* (developed simultaneously by Eyring and Polanyi in 1935)^[4,6] and corresponds to a steady-state regime. The authors established that in many catalytic cycles only one transition state and one intermediate determine the TOF, corresponding to the TOF-determining transition state (TDTS) and the TOF-determining intermediate (TDI), respectively. These key states can be located by evaluating the degree of TOF control (X_{TOF}); this last term belongs to the family of structure–reactivity coefficients used in classical physical organic chemistry to describe the influence of various factors

(substituents, solvents, equilibrium constants, etc.) on rates.^[7] The energy difference between TDTS and TDI, together with the reaction driving force (ΔG_r), define the energetic span (δE) of the cycle. Whenever the TDTS appears after the TDI, δE is the energy difference between these two states; when the opposite is true, the addition of ΔG_r to this difference is needed. Having δE , the TOF is expressed simply in the Arrhenius–Eyring fashion, wherein δE serves as the apparent activation energy of the cycle. The energetic span model will be used in Chapter 5 in order to evaluate TOFs of the reaction studied and compare them with those from the experiments.

1.2 Carbon dioxide fixation

1.2.1 Environmental perspective

Two major energy-related problems confront the world in the next 50 years. First, increased worldwide competition for gradually depleting fossil fuel reserves (these currently represent 80-85% of the world's energy sources) will lead to higher costs, both monetarily and politically. Second, the ever-increasing levels of atmospheric CO₂ as a result of anthropogenic emissions, with a current level of 399 ppm (Figure 1.1), precisely from those carbon-based fossil fuels is considered to be the major contributor to climate change that may cause extreme events (high or low temperature, heavy rain, and dryness) that are out of human control.

Some technologies have been introduced in order to reduce the CO₂ emissions.^[8] Among these, a method that has received major consideration involves carbon dioxide capture and storage (CCS), which is seen as one of the most important single reduction measures worldwide contributing with 8.2 Gt.^[9] In addition, sequestration in geologic formations is viewed by some as a long-term solution.^[10] However, these technologies involve significant energy and economic costs, as well as their utilization adds value to the waste carbon dioxide, thereby offsetting the cost of capture and storage.

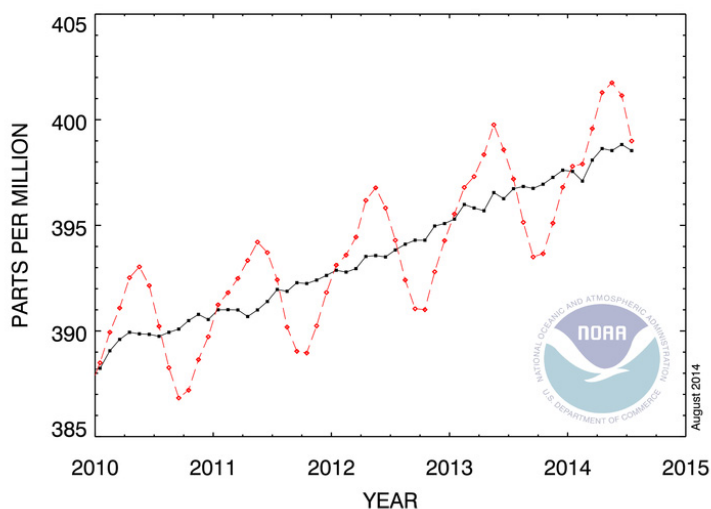


Figure 1.1 The steady increase in CO₂ concentrations in the atmosphere in recent years. The dashed red line and solid black line indicate the monthly mean values and the average seasonal cycle, respectively. Adapted from <http://www.esrl.noaa.gov/gmd/ccgg/trends/>

Providing a future energy supply that is secure and CO₂-neutral will require switching to nonfossil energy sources such as wind, solar, nuclear, and geothermal energy and developing balanced cost-effective methods for transforming the energy produced by these new sources into forms that can be stored, transported, and used upon demand.

1.2.2 Carbon dioxide as chemical feedstock

The use of CO₂ as a renewable carbon feedstock is of both academic and industrial relevance.^[11] Several chemical processes have been successfully developed where CO₂ is used as a reagent, as summarized in Figure 1.2.^[11c] Nevertheless, only in a limited number of cases, those reactions classify as truly sustainable from the point view of energy use and carbon recycling. A widely accepted idea is that CO₂ is so thermodynamically and kinetically stable that it is rarely used to its fullest potential. However, due to the electron deficiency of the carbonyl carbons, CO₂ has a strong affinity toward nucleophiles and electron-donating reagents. In other words, CO₂ is an “anhydrous carbonic acid”, which rapidly reacts with basic compounds.

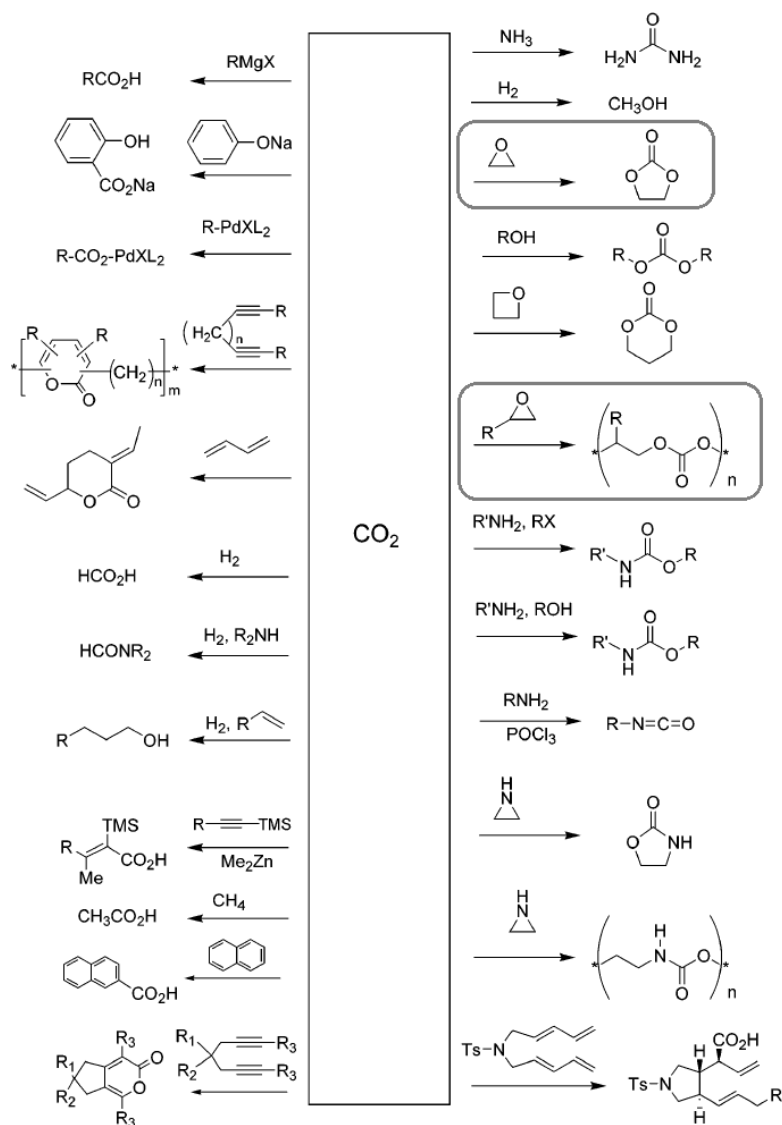


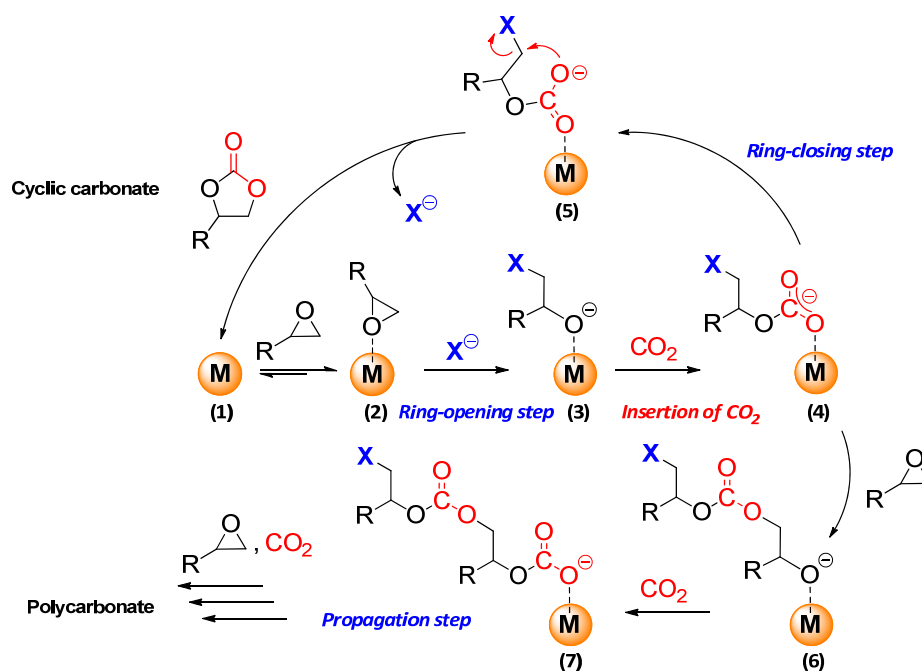
Figure 1.2 Transformations of carbon dioxide. The emphasized reactions correspond to the chemical fixation of CO₂ into epoxides providing either cyclic carbonates or polycarbonates.

Catalysis can be used to effectively lower the barriers associated with the kinetic stability, as well as reacting CO₂ with relatively high free energy substrates like hydrogen, amines or epoxides.^[12] Among these options, the atom-efficient fixation of CO₂ to epoxides can lead to the formation of two relevant products: polycarbonates and cyclic carbonates. The mechanistic study of these reactions (highlighted in Figure 1.2) is the main focus of the present thesis.

1.2.3 Mechanistic aspects of the catalyzed CO₂ fixation

Many families of homogeneous and heterogeneous catalysts involving transition metal complexes have been investigated for the reaction of CO₂ with epoxides.^[13] However, only the first type of catalysts will be considered in the present document.

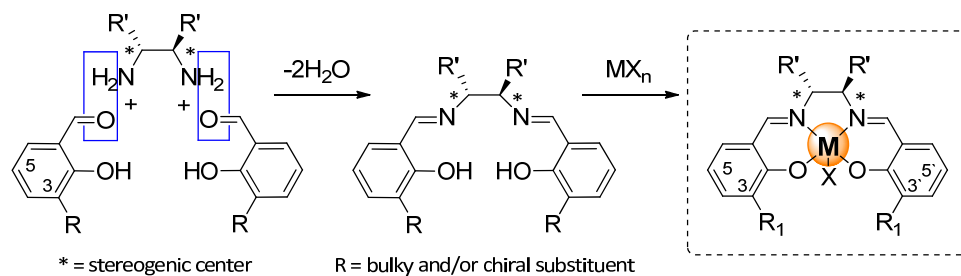
Usually, the catalytic systems employed to mediate this reaction involve a Lewis acid species and a nucleophile, i.e. a binary catalyst system. Scheme 1.3 indicates that the Lewis acidic metal center (1) has the role of activating the epoxide (2) towards subsequent nucleophilic attack by a suitable initiator (X), undergoing ring-opening. The alkoxide intermediate formed (3) reacts with the CO₂ molecule to form a carbonate (4). The latter species can either undergo ring-closing reaction (5) leading to the formation of the cyclic carbonate, or react further through the alternating insertion of epoxide and CO₂ monomers (6 and 7), yielding a polycarbonate (propagation reaction).



Scheme 1.3 Catalytic mechanism for chemical fixation of CO₂ into epoxides leading to formation of polycarbonates and cyclic carbonates.

Two different types of homogeneous catalysts are used in the present thesis: metal-derived salen complexes (or metallosalen complexes)^[14] and metal-derived amine triphenolate complexes.^[15]

Salen ligands (*N,N'*-bis(salicylidene)ethylenediamine), shown in Scheme 1.4, can be synthesized by dehydration condensation reaction of readily available diamine and (substituted) salicylaldehyde precursors. The formation of metallosalen complexes is achieved by simply mixing the above ligand with a metal ion after its conversion to the corresponding phenoxide ion derivative or under basic conditions. Chiral salen complexes combine typical advantages such as ease of variation in steric and electronic features. In contrast, non-chiral complexes have received less attention since their application potential in homogeneous catalyst has been considered limited.



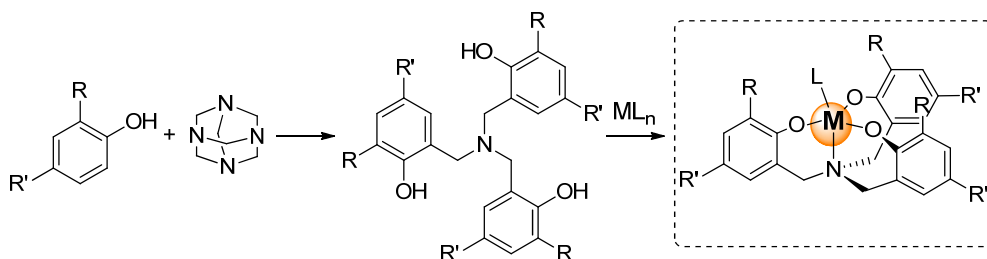
Scheme 1.4 General synthesis of metallosalen complexes.

In general, the important structural features of salen complexes are the existence of an ethylene unit therein located adjacent to a metal ion and that of the large space between the 3- and 3'- positions (Scheme 1.4). These features allow the reaction field around the metal ion, to be tailored to fit with specific reactions through the introduction of suitable substituents at the ethylene and the 3- and 3'-positions. Another important feature of salen complexes is the structural-flexibility that is provided by the existence of the ethylene unit. Most of the salen complexes have an octahedral structure, and in many cases the salen ligand coordinates tetravalently with the central ion on the same plane (*trans*-isomer). Namely, four of the coordinating atoms (N, N, O, O) of the ligand occupy equatorial positions and the other ligands (X, Y) bind at the apical positions (Scheme 1.4).

Although salen ligands coordinate tetravalently on a single plane, this does not mean that the ligands adopt planar structures. A five-ring chelate constituted from ethylene diamine and a central ion can adopt a half-chair conformation, an envelope conformation or a slightly distorted form of one of these.

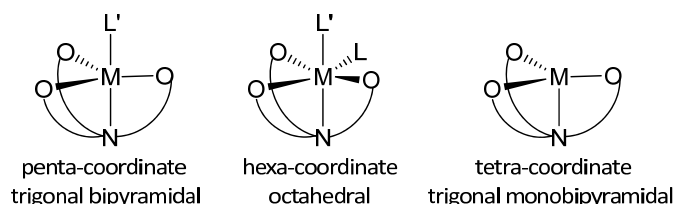
Phenyl-bridged (at the R_2 position in Scheme 1.4) salen ligands are known as *salphens* or *salophens*. These complexes present a rigid geometry around the metal center that can be used to manipulate properties such as the Lewis acid character of the metal and therefore can be effectively applied to increase the reactivity of the resulting complex.

On the other hand, one method to synthesize amino triphenolate ligands is *via* Mannich reaction with 2,4-dialkylphenol and hexamethylenetetraamine,^[16] as depicted in Scheme 1.5. Several examples of amine triphenolate complexes can be found in literature for early transition metals (d^0 , d^5) and main group elements (d^{10}), also late transition metal complexes have been described but they are still rare. For most of these complexes detailed crystallographic and in solution studies are available. This large amount of data arises from the high stability of amine triphenolate complexes, for which the chelate effect coming from the polydentate TPA ligand is a direct responsible. In these complexes, TPA usually binds the metal as a tetradentate ligand: the three anionic oxygen atoms occupying equatorial positions and the tertiary amine occupying one of the axial positions.



Scheme 1.5 General synthesis of amine triphenolate complexes.

In the vast majority of examples mononuclear complexes displaying a 1 : 1 ligand–metal ratio are obtained. The trigonal bipyramidal (TBP) and octahedral (OCT) geometries predominate whereas tetra-coordinate complexes with trigonal monopyramidal (TMP) geometry are unusual (Scheme 1.6).



Scheme 1.6 Common geometries in amine triphenolate complexes.

1.3 Ion mobility mass spectrometry (IM-MS)

1.3.1 Basic concepts

Mass spectrometry (MS) is a key tool for molecular characterization, and the allied technique of ion mobility (IMS) is enhancing many areas of chemical analysis. Strong synergy arises between these two techniques because of their ability to determine complementary information about gas-phase ions. The mobility of a gas-phase ion is a measure of its velocity when traverses a drift tube filled with a neutral buffer gas, typically helium, in the presence of a weak electric field (E). In combination with MS, IMS offers separation on the basis of the drift time (t_d) and mass-to-charge ratio (m/z).

The process of drifting ions through a buffer gas, under the influence of E , can be visualized as a forward acceleration due to the electric field and the retarding effect due to the collisions with the buffer gas until equilibrium is reached. In classical IMS the energy supplied by E is lower than the thermal energy provided by the collisions with the buffer gas molecules. Consequently, a steady state is reached where the drift velocity (V_d) remains constant, and is proportional to E according with the expression:

$$V_d = KE \quad (1.6)$$

This proportionality constant is called ion mobility constant (K) and is related to the ion's collision cross section CCS ($\Omega_{\text{avg}}^{(1,1)}$) by the Mason-Schamp equation:^[17]

$$K = \frac{3q}{16N} \left(\frac{2\pi}{k_B T} \right)^{1/2} \left(\frac{1}{m} + \frac{1}{M} \right)^{1/2} \frac{1}{\Omega_{\text{avg}}^{(1,1)}} \quad (1.7)$$

where q is the charge on the ion, N is the number density of the buffer gas, m and M are the masses of the ion and buffer gas, respectively, T is the gas temperature, k_B is the Boltzmann constant, and $\Omega_{\text{avg}}^{(1,1)}$ is the orientationally averaged cross section (see Section 2.8 of Chapter 2 for further information on this latter). Equation 1.7 indicates that the mobility of an ion depends, besides its nature, on a number of instrumental factors such as pressure, temperature and number density of the buffer gas. If such factors are carefully controlled and kept constant, determining the ion collision cross section is possible by measuring its drift time t_d (in ms). Thus, considering t_d and the drift tube length (l) equation 1.6 can be expressed as:

$$K = \frac{l}{t_d E} \quad (1.8)$$

Once obtained K experimentally, $\Omega_{\text{avg}}^{(1,1)}$ can be calculated using equation 1.7. K value is usually corrected to standard conditions of temperature (T in Kelvin) and pressure (P in Torr). The reduced mobility constant (K_0) is then calculated by:

$$K_0 = K \frac{273 P}{T 760} \quad (1.9)$$

Ion mobility-mass spectrometry (IM-MS) can thus act as a tool to separate complex mixtures, to resolve ions that may be indistinguishable by mass spectrometry alone, or to determine structural information (for instance rotationally averaged CCSs), complementary to more traditional structural approaches.

Even though IM-MS was first described in 1962,^[18] it has only recently become relatively ordinary, mainly owing to commercialization of the necessary instrumentation. Figure 1.3 shows that in the past 10 or so years there have seen an explosion in research using IM-MS, as demonstrated by a rapid increase in the annual number of peer-reviewed publications.^[19]

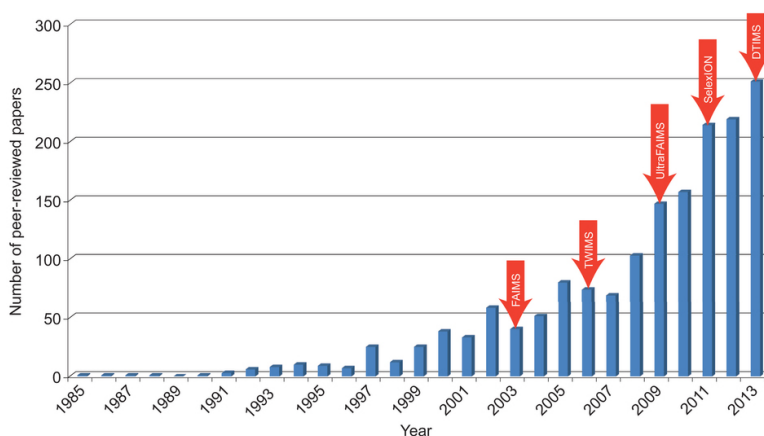


Figure 1.3 Number of peer-reviewed papers published annually (to end of 2013) combining ion mobility and mass spectrometry (IM-MS). Adapted from ref 19

One of the benefits offered by IM-MS is that the outcome from experimental measurements can be compared with that obtained *via* electronic-structure calculations in

order to ascertain structural information of ions. For this purpose CSSs are obtained using both methodologies and then confronted. Alternatively, IM-MS can be employed as a rapid means to analyze a model chemical reaction mixture, offering the potential for real-time reaction monitoring, and thus elucidation of possible reaction mechanisms.^[20] This two features of IM-MS are indeed, demonstrated on Chapter 3.

1.3.2 IM-MS instrumentation

An IM-MS instrument must perform five basic processes: sample introduction, compound ionization, ion mobility separation, mass separation and ion detection.^[21] Schematic representation of a typical IMS drift tube configuration is depicted in Figure 1.4. Ions are generated in an ionization region that may be external to the drift region, as for example in electrospray, or close coupled to the instrument like the ^{63}Ni sources. As above described, a combination of gas flow and electrical fields are used to move the ions towards the drift region, where they encounter an ion shutter or gate which pulses the ions into the drift tube. Once entering the drift tube, the ions are subjected to a uniform weak electric field, which accelerates them towards a detector situated at the end of the drift tube. A drift gas is present in the drift region at a constant pressure, which may be between 1 Torr and atmospheric pressure, depending on the IMS configuration. An ion passing through the buffer gas experiences a number of collisions that impede its progress towards the detector. Larger ions with greater collision cross sections experience more collisions than smaller ions and therefore take longer to traverse the drift tube. The separation of ions of differing shape and size therefore becomes possible.

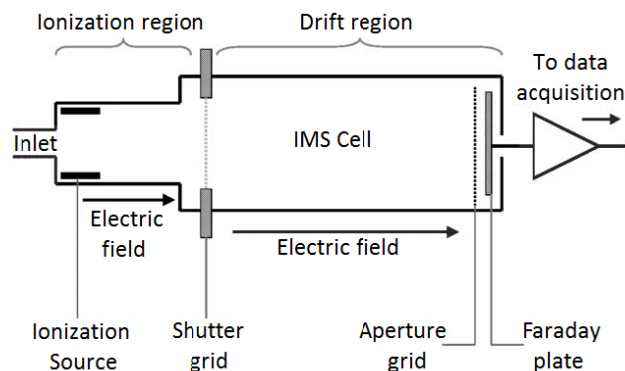
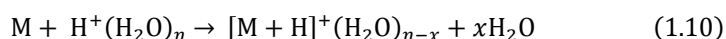


Figure 1.4 Schematic diagram of an ion mobility spectrometer.

The choice of the method for introducing the sample in IMS basically depends on the chemical nature of the sample, analysis requirements and type of ionization used. The most common ionization source is based on ionizing radiation, which is usually produced by ^{63}Ni . The disintegration of this element emits β particles which ionize the drift gas and form thermalized electrons. The ionized buffer reacts with trace impurities of water and, through a series of ion–molecule reactions, reactant ion species such as $\text{H}^+(\text{H}_2\text{O})_n$ are formed. If sample molecules (M) have a greater proton affinity than that of the reactant ions, the dominant process of product ion generation is through proton transfer:



Besides detection of $[\text{M} + \text{H}]^+$ species, some other compounds such as dimers ($[\text{2M} + \text{H}]^+$), clusters containing neutral molecules ($[\text{M} + \text{H}]^+ \cdot \text{L}_n$), and negative ions ($[\text{M} - \text{H}]^-$) can be often detected. Doping materials like ammonia, nitrogen monoxide and acetone are sometimes added to the drift gas for ionization selectivity. IMS has also been combined with variety of ionization sources such as, photoionization (PI)^[22], corona discharge ionization (CDI)^[23] and secondary electrospray ionization (SESI)^[24] for vapor samples, electrospray ionization (ESI)^[25] for liquid samples and matrix assisted laser desorption ionization (MALDI)^[26] for solid samples.

Once generated the ions, these are gated into the drift region by applying a potential to the shutter grid, at the end of the ionization source, for a certain period of time (50-300 μs), after this, the polarity of the shutter grid is changed in about 30 ms to prevent the entry of more ions during their motion through the drift region (discontinuous ion introduction). In this region, the ions are transported to the detector by applying electrical voltages (around 1-500 $\text{V}\cdot\text{cm}^{-1}$) generated by a series of field defining electrodes (circular metal drift rings, Figure 1.4), and the ion mobility spectrum can be obtained easily by chromatographic techniques or mass spectrometry.

The way ions motion is induced by the electric field defines the type of ion mobility separation method used with mass spectrometry, as shown in Figure 1.5. Primarily, four types of IMS techniques are used in IM-MS: drift-time ion mobility spectrometry (DTIMS),^[27] aspiration ion mobility spectrometry (AIMS),^[28] field-asymmetric ion mobility spectrometry (FAIMS),^[29] and travelling-wave ion mobility spectrometry (TWIMS).^[30]

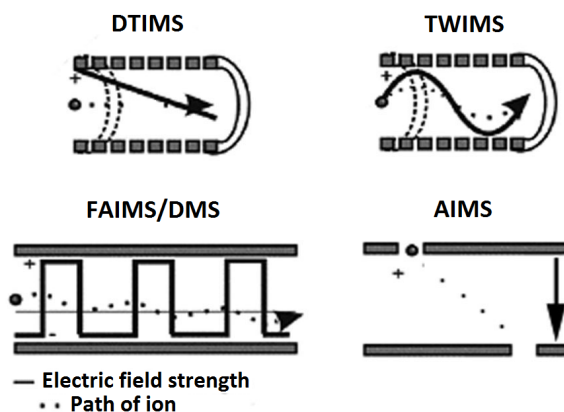


Figure 1.5 Schematic representation of the ion motion induced by the electric field for defining the different types of ion mobility separation methods used in IM-MS. Adapted from ref 21b

DTIMS is the oldest and conceptually simplest form of ion mobility, which is based on the traditional IMS diagram depicted in Figure 1.4. This method provides the highest IMS resolving power, and it is the only IM-MS method that can directly measure CCS. The common disadvantage of DTIMS is that, in order to achieve separation, a narrow pulse of ions must be periodically introduced into the drift region, creating a duty cycle which decreases the sensitivity of the instrument.^[31] Both DTIMS and AIMS operate at atmospheric pressure and low voltages.

Unlike DTIMS, in AIMS the ions are continuously gated into the drift tube by directing the flow of buffer gas perpendicular to the direction of the electric field. The ions are introduced with the buffer gas into the electric field such that they are directed orthogonally to the gas flow and onto a series of segmented electrodes. Ion mobility is measured as a function of the distance they travel through the buffer gas before impinging on an electrode. Both positive and negative ions can be measured simultaneously since they travel in opposite directions and are collected on the two sets of opposing segmented electrodes.

The basic principle of operation of FAIMS (also known as differential IMS, DMS) is that ions are introduced to a region with cylindrical electrodes and a stream of gas acts as a transport medium. An asymmetric waveform is passed across the electrodes, which consists of a high potential electric field for a short time followed by a low potential electric field for a longer time; this typically fixed dispersion voltage (DV) waveform is

superimposed with a variable compensation voltage (CV) to maintain a stable trajectory for the analyte ion. This process will effectively select ions and act as an ion filter.

TWIMS is a novel method whereby ions are separated according to their mobility in a series of voltage pulses in a traveling wave (T-wave) mobility cell utilizing radio-frequency (RF) ion guides. The resolving power is relatively low; however, CCS can be derived by calibration with known standards. In TWIMS a transient DC voltage pulse is applied in order to create an electromotive force via a series of sequentially opposite polarity RF-only rings to create a traveling wave which propels ions through the device, as shown in Figure 1.6. Ions with high IM slip behind the wave less often (or spend more time surfing) than ions of low IM thus enabling separation based on relative IM.

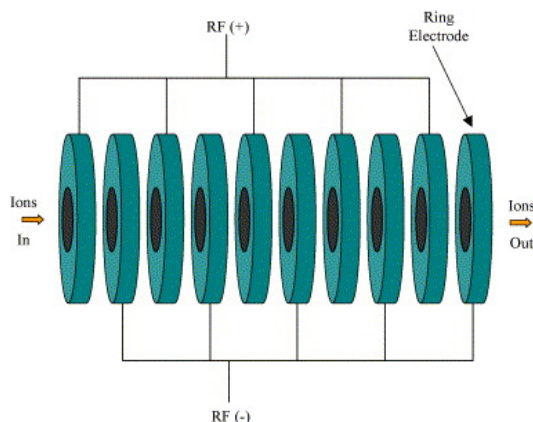


Figure 1.6 Illustration of a stacked ring ion guide used in traveling wave ion mobility spectrometry (TWIMS). Adapted from ref 21b

There are a variety of mass spectrometers that can be used with each of the previous IMS methods. Among these the most common are the Time-of-flight (used with DTIMS),^[32] quadrupole (used with DTIMS),^[33] ion-trap (used with AIMS),^[34] Fourier transform ion-cyclotron (used with FAIMS),^[35] or tandem mass spectrometers (used with TWIMS).^[36]

1.4 Aims and outline

Computational chemistry is certainly a fundamental tool for the study of reaction mechanisms comprising homogeneous catalysis.^[37] Several theoretical studies involving different families of transition metal complexes have been conducted towards the

catalyzed fixation of CO₂, as described in the introduction of *Chapters 4* and *6*. In this context, special attention has been paid to evaluation of the mechanisms describing the formation of useful cyclic carbonate and polycarbonates from CO₂ and epoxides. This latter issue is indeed the main focus of the present thesis.

The synergy between the existing computational methodologies (described in *Chapter 2*) and the outcome from experiments (in close collaboration with specialized researching groups) provides a better understanding of the chemical nature of the reactions and other processes. In light of this, the development of this thesis aims to:

- Provide structural information on a series of transition metal complexes used in homogeneous catalysis by means of ion mobility mass spectrometry (IM-MS).
- Determine collision cross sections (*via* IM-MS) for different metal-containing catalytic compounds, and explore its correlation with experimental results.
- Examine computationally the mechanistic steps (ring-opening, CO₂ insertion and ring-closing) for the catalytic formation of cyclic carbonates from CO₂ and epoxides based on Zn(salen) complexes.
- Establish a comparison between the catalytic activity presented by two different Zn(salen) complexes containing N₂O₂-donor and N₄-donor ligands.
- Understand the reaction mechanism operating for the [Al{amino-tris(phenolate)}]/NBu₄⁺ catalyzed CO₂ fixation into epoxides to yield either cyclic carbonates or polycarbonates.
- Get insights towards quantification of the catalytic activity for the [Al{amino-tris(phenolate)}]/NBu₄⁺ catalyzed CO₂ fixation by determining theoretically turnover frequencies (TOFs) and comparing with experimental results.

Connected to these objectives, *Chapter 2* includes a brief description of the approaches supplied by computational chemistry for studying reactions in homogeneous catalysis, such as the wave function-based methods, density functional theory (DFT), methods for

including solvent effects and dispersion forces in DFT, standard state modifications to thermodynamic properties, and methods used for determining collision cross sections (CCSs) in IM-MS.

In *Chapter 3*, IM-MS is used to explore structural features of a group of three salen ligands and their complexes with Cu and Zn, as well as Pd-containing intermediates within the catalytic Stille reaction. CCSs for all the systems studied were determined theoretically and compared with CCSs obtained through IM-MS experiments, reaching excellent agreement between both methodologies.

Chapter 4 describes in detail the reaction mechanism for the catalytic formation of cyclic carbonates from CO₂ and a series of epoxides based on two different types of Zn(salen) complexes (with N₂O₂-donor and N₄-donor ligands), in conjunction with NBu₄X (X = Br, I), allowing for identification of the critical steps of the reaction and characterization of the different species (transition states and intermediates) involved in the chemical process.

Chapter 5 includes a monometallic mechanism for the [Al{amino-tris(phenolate)}]/NBu₄I catalyzed addition of CO₂ to epoxides (propylene oxide and also 1,2-epoxyhexane) yielding cyclic carbonate products. Unlike the Zn(salen) catalytic reaction (described in *Chapter 4*), for the aluminium-mediated reaction, quantitative evaluation of the activity displayed by the catalyst system was determined through theoretical calculation of the TOFs. Estimation of both solvent and entropic effects was included in order to determine its influence in the TOFs measurements. Results are fully in line with the experimental outcome.

Chapter 6 reports a detailed mechanistic study on the alternating copolymerization of CO₂ and cyclohexene oxide. Three potential mechanisms (one monometallic and two bimetallic) are envisaged for polycarbonates formation, depending on the number of active Al-complexes employing for this purpose. The rate-determining steps were identified for the mechanisms studied, being the CO₂ insertion in the initiation reaction crucial for the two bimetallic mechanisms; whereas for the monometallic reaction, the epoxide ring-opening was found to be rate-determining. According to the barriers found for both bimetallic mechanisms, the alternating copolymerization is favored over the formation of the cyclic carbonate.

1.5 References and notes

- [1] a) P. W. N. M. van Leeuwen, *Homogeneous Catalysis: Understanding the Art*, Kluwer Academic Publishers, Dordrecht, **2004**; b) S. Bhaduri, D. Mukesh, *Homogeneous Catalysis: Mechanisms and Industrial Applications*, Wiley-VCH, Weinheim **2000**.
- [2] J. J. Berzelius, *Annales chimie physiques* **1836**, *61*, 146.
- [3] S. Arrhenius, *Zeit. Phys. Chem.* **1899**, *28*, 317.
- [4] H. Eyring, *J. Chem. Phys.* **1935**, *3*, 107.
- [5] a) S. Kozuch, S. Shaik, *Acc. Chem. Res.* **2010**, *44*, 101; b) S. Kozuch, *WIREs Comput. Mol. Sci.* **2012**, *2*, 795.
- [6] M. G. Evans, M. Polanyi, *Trans. Faraday Soc.* **1935**, *31*, 875.
- [7] C. Ritchie, *Physical organic chemistry: the fundamental concepts*, 2nd Edition, M. Dekker, New York **1990**.
- [8] *Carbon Dioxide as Chemical Feedstock*, M. Aresta (ed), Wiley-VCH, Weinheim **2010**.
- [9] IEA, *Energy Technology Perspectives – Scenarios & Strategies to 2050 978-92-64-08597-8*, OECD/IEA, Paris **2010**.
- [10] *DOE/NETL Carbon dioxide Capture and Storage RD&D Roadmap*, U.S. DOE National Energy Technology Laboratory (NETL), Dec **2010** (full text available at <http://www.netl.doe.gov/File%20Library/Research/Carbon%20Seq/Reference%20Shelf/CCSRoadmap.pdf>).
- [11] a) P. Markewitz, W. Kuckshinrichs, W. Leitner, J. Linszen, P. Zapp, R. Bongartz, A. Schreiber, T. E. Müller, *Energy Environ. Sci.* **2012**, *5*, 7281; b) M. Cokoja, C. Bruckmeier, B. Rieger, W. A. Herrmann, F. E. Kühn, *Angew. Chem. Int. Ed.* **2011**, *50*, 8510; c) T. Sakakura, J. C. Choi, H. Yasuda, *Chem. Rev.* **2007**, *107*, 2365; d) R. Martín, A. W. Kleij, *ChemSusChem* **2011**, *4*, 1259.
- [12] a) W. Leitner, *Acc. Chem. Res.* **2002**, *35*, 746; b) Y. Li, X. Fang, K. Junge, M. Beller, *Angew. Chem., Int. Ed.* **2013**, *52*, 1.
- [13] a) P. P. Pescarmona, M. Taherimehr, *Catal. Sci. Technol.* **2012**, *2*, 2169; b) G. W. Coates, D. R. Moore, *Angew. Chem., Int. Ed.* **2004**, *43*, 6618; c) M. North, R.

- Pasquale, C. Young, *Green Chem.* **2010**, *12*, 1514; d) A. Decortes, A. M. Castilla, A. W. Kleij, *Angew. Chem., Int. Ed.* **2010**, *49*, 9822; e) M. R. Kember, A. Buchard, C. K. Williams, *Chem. Commun.* **2011**, *47*, 141; f) S. Klaus, M. W. Lehenmeier, C. E. Anderson; B. Rieger, *Coord. Chem. Rev.* **2011**, *255*, 1460; g) M. Taherimehr, S. M. Al-Amsyar, C. J. Whiteoak, A. W. Kleij, P. P. Pescarmona, *Green Chem.* **2013**, *15*, 3083; h) D. J. Darensbourg, *Chem. Rev.* **2007**, *107*, 2388.
- [14] a) C. J. Whiteoak, G. Salassa, A. W. Kleij, *Chem. Soc. Rev.* **2012**, *41*, 622; b) T. Katsuki, *Fascination of metallosalen complexes: Diverse catalytic performances and high asymmetry-inducing ability*, TCIMail number 124, **2006**.
- [15] a) G. Licini, M. Mba, C. Zonta, *Dalton Trans.* **2009**, 5265; b) C. J. Whiteoak, E. Martin, M. Martínez Belmonte, J. Benet-Buchholz, A. W. Kleij, *Adv. Synth. Catal.* **2012**, *354*, 469.
- [16] L. J. Prins, M. M. Blázquez, A. Kolarović, G. Licini, *Tetrahedron Lett.* **2006**, *47*, 2735.
- [17] E. A. Mason, H. W. Jr. Schamp, *Ann. Phys.* **1958**, *4*, 233.
- [18] E. W. McDaniel, D. W. Martin, W. S. Barnes, *Rev. Sci. Instrum.* **1962**, *33*, 2.
- [19] F. Lanucara, S. W. Holman, C. J. Gray, C. E. Eyers, *Nat. Chem.* **2014**, *6*, 281.
- [20] C. S. Creaser, J. R. Griffiths, C. J. Bramwell, S. Noreen, C. A. Hill, C. L. P. Thomas, *Analyst* **2004**, *129*, 984.
- [21] a) E. L. Harry, A. W. T. Bristow, I. D. Wilson, C. S. Creaser, *Analyst* **2011**, *136*, 1728; b) C. Laphorn, F. Pullen, B. Z. Chowdhry, *Mass Spectrom. Rev.* **2013**, *32*, 43; c) A. B. Kanu, P. Dwivedi, M. Tam, L. Matz, H. H. Hill, *J. Mass Spectrom.* **2008**, *43*, 1.
- [22] H. Borsdorf, M. Rudolph, *Int. J. Mass Spectrom.* **2001**, *208*, 67.
- [23] C. A. Hill, C. L. P. Thomas, *Analyst* **2005**, *130*, 1155.
- [24] C. Wu, W. F. Siems, J. Klasmeier, H. H. Hill, *Anal. Chem.* **2000**, *72*, 391.
- [25] C. Shumate, *Trends Anal. Chem.; TrAC* **1994**, *13*, 104.
- [26] a) K. J. Gillig, B. Ruotolo, E. G. Stone, D. H. Russell, K. Fuhrer, M. Gonin, A. J. Schultz, *Anal. Chem.* **2000**, *72*, 3965; b) W. E. Steiner, B. H. Clowers, W. A. English, H. H. Hill, *Rapid Commun. Mass Spectrom.* **2004**, *18*, 882.
- [27] G. A. Eiceman, V. J. Vandiver, T. Chen, G. Rico-Martinez, *Anal. Inst.* **1989**, *18*, 227.
- [28] E. Sacristan, A. A. Solis, *IEEE Trans. Instrum. Meas.* **1998**, *47*, 769.

- [29] R. W. Purves, R. Guevremont, S. Day, C. W. Pipich, M. S. Matyjaszczyk, *Rev. Sci. Instrum.* **1998**, *69*, 4094.
- [30] K. Giles, S. D. Pringle, K. R. Worthington, D. Little, J. L. Wildgoose, R. H. Bateman, *Rapid Commun. Mass Spectrom.* **2004**, *18*, 2401.
- [31] B. H. Clowers, W. F. Siems, H. H. Hill, S. M. Massick, *Anal. Chem.* **2006**, *78*, 44.
- [32] a) K. B. Jr. McAfee, D. P. Sipler, D. Edelson, *Phys. Rev.* **1967**, *160*, 130; b) L. G. McKnight, K. B. McAfee, D. P. Sipler, *Phys. Rev.* **1967**, *164*, 62.
- [33] R. Johnsen, H. L. Brown, M. A. Biondi, *J. Chem. Phys.* **1970**, *52*, 5080.
- [34] C. S. Hoaglund, S. J. Valentine, D. E. Clemmer, *Anal. Chem.* **1997**, *69*, 4156.
- [35] D. C. Parent, M. T. Bowers, *Chem. Phys.* **1981**, *60*, 257.
- [36] S.I. Merenbloom, S. L. Koeniger, S. J. Valentine, M. D. Plasencia, D. E. Clemmer, *Anal. Chem.* **2006**, *78*, 2802.
- [37] W. Thiel, *Angew. Chem. Int. Ed.* **2014**, *53*, 8605.

UNIVERSITAT ROVIRA I VIRGILI

THEORETICAL STUDIES ON TRANSITION METAL CATALYZED CARBON DIOXIDE FIXATION

Fernando Simón Castro Gómez

2.1 Introduction

In the late seventies appeared a new science that was oriented towards computer-aided molecular design: *computational chemistry*. This branch of chemistry (also called *molecular modeling*; the two terms mean about the same thing) is a set of techniques used to assist in solving chemical problems on a computer.^[1] It was driven by the big pharmaceutical companies in the world interested in medicinal chemistry and also because the rapid development of computation. Thereafter the phrase "*Chemistry is an experimental science*" lost some validity. Nowadays the theoretical prediction of structures and properties of molecules and solids rivals even advantageously with experimental determinations.^[2] Computational chemistry uses methods of theoretical chemistry, which are incorporated into efficient computer programs, to calculate properties such as structure (i.e., the expected positions of the constituent atoms), absolute and relative (interaction) energies, electronic charge distributions, dipoles and higher multipole moments, vibrational frequencies or other spectroscopic quantities, substrate-enzyme interactions, collision cross sections between particles, and chemical reactivity (with wide application in homogeneous and heterogeneous catalysis, photochemistry, biochemistry, and other fields).

In regards to homogeneous catalysis, this is an area of chemistry where molecular modeling plays a key role. Catalytic cycles are usually multistep complicated processes that involve the formation and evolution of intermediate species often difficult, if not possible, to characterize experimentally. Thus, computational chemistry can be the only way to access to a detailed knowledge of the reaction mechanism that can be a fundamental piece of information in the optimization and design of new processes and catalysts.^[3]

The development of new computational methods (such as local correlation methods, dispersion-corrected methods, combined quantum mechanics/molecular mechanics (QM/MM), Ab initio molecular dynamics methods (AIMD) and more) and the increase in computer power have opened up new opportunities for guiding the design of more efficient catalysts using computational approaches.^[4] However, the study of homogeneous catalytic systems pose many challenges for computational quantum chemists. Many times a first-principle's quantum mechanical calculation (i.e., wave function-based methods) involves a straightforward model that only ambiguously resembles the true system. If large

ligand systems are involved they are most frequently neglected in high level calculations with the hope that they do not substantially influence the nature of the reaction mechanism.^[5] Nevertheless, the surrounding ligand system or the solvent medium can often play a critical role in such reaction mechanisms. One reasonable alternative to these wave function-based methods is the density functional theory (DFT), which allows the implementation of more sophisticated computational models for studying large systems. Both approaches are described below, focusing mainly on the DFT methods that are the basis for the realization of this thesis. Some other important topics like the use of dispersion-based methods, inclusion of solvent effects, as well as the evaluation of thermodynamic properties, collision cross sections and other chemical properties will be also reviewed in this chapter.

2.2 Ab initio wave function-based methods

Ab initio wave function-based methods rest on solving the time-independent Schrödinger equation:^[6]

$$\hat{H}\Psi(\vec{q}) = E\Psi(\vec{q}) \quad (2.1)$$

where \hat{H} is the full time-independent Hamiltonian operator, E is the total energy of the quantum system under study, Ψ is the wave function defined by \vec{q} which contains the nuclear and electronic coordinates of the system. The typical form of the Hamiltonian operator takes into account five contributions to the total energy of the system: the kinetic energies of the electrons and nuclei, the attraction of the electrons to the nuclei, and the interelectronic and internuclear repulsions. Since the mathematical complexity of the terms concerning this operator prevents the exact resolution of the wave function, it is necessary resorting to the use of approximations. One of the most important approximations applied to the Schrödinger equation is the Born-Oppenheimer approximation.^[7] The latter says that due to the big difference in mass between electrons and nuclei, the electron's motion is much more faster and it is assumed that the nuclei are stationary. In this way, the kinetic energy term of the nuclei can be omitted, and the repulsion potential between nuclei can be considered as a parameter. The Hamiltonian is simplified thereby and the time-independent Schrödinger equation gets reduced to an

electronic problem. The Born-Oppenheimer approximation is one of the cornerstones of computational chemistry because it makes the concept of molecular shape (geometry) meaningful, makes possible the concept of Potential Energy Surface (PES), and simplifies the application of the Schrödinger equation to molecules by allowing us to focus on the electronic energy and add in the nuclear repulsion energy later.^[1]

Even after simplification by using the Born-Oppenheimer approximation, the exact resolution of the electronic time-independent Schrödinger equation only is applicable for one-electron systems. However, for many-electron systems (as for instance, molecules involved in chemical reactivity) such electronic interactions obviously become larger, and therefore it is indispensable the use of more approximations, as described below.

2.2.1 Hartree-Fock method

Probably the most representative and simplest Ab initio approximation used for solving the electronic time-independent Schrödinger equation is the Hartree-Fock (HF) method,^[8] which represents the many-electron wave function through a single Slater determinant:

$$\Psi(x_1, x_2, \dots, x_N) = \frac{1}{\sqrt{N!}} \begin{vmatrix} \chi_i(x_1) & \chi_j(x_1) & \cdots & \chi_N(x_1) \\ \chi_i(x_2) & \chi_j(x_2) & \cdots & \chi_N(x_2) \\ \vdots & \vdots & \ddots & \vdots \\ \chi_i(x_N) & \chi_j(x_N) & \cdots & \chi_N(x_N) \end{vmatrix} \quad (2.2)$$

The Slater determinant solution is given by all possible electron permutations along the spin-orbitals χ_i . Each permutation is a product (called Hartree product) of the one-electron functions χ_i . The normalized summation of all possible permutations generates an antisymmetrized wave function that ensures fulfillment of Pauli Exclusion Principle. Each spin-orbital is composed for the product of one spatial function φ_i (spatial orbital) and one spin function (α or β which are orthonormal):^[9]

$$\chi_i(x_j) = \chi_i(\vec{r}_j, s) = \begin{cases} \chi_i^\alpha = \varphi_i(\vec{r}_j)\alpha(s) \\ \text{or} \\ \chi_i^\beta = \varphi_i(\vec{r}_j)\beta(s) \end{cases} \quad (2.3)$$

Through the variation of the spin-orbitals and keeping the orthonormality between them, it is possible to find the Slater determinant having the lowest energy. Due to HF is based on the variational principle the expectation value is always higher than the exact energy. The HF equations have the general form:

$$f_i \chi_j(x_i) = \varepsilon_j \chi_j(x_i) \quad (2.4)$$

where ε_j is the energy of the j -th spin-orbital χ_j and f_i is the Fock operator for the i -th electron, which is defined as:

$$f_i = \hat{h}_i + \sum_j \hat{J}_j(x_i) - \hat{K}_j(x_i) \quad (2.5)$$

This operator includes the one-electron Hamiltonian operator \hat{h}_i , and the Coulomb \hat{J}_j and Exchange \hat{K}_j operators. The \hat{h}_i operator describes the kinetic energy for the i -th electron, and the attraction between the electrons and nuclei. On the other hand, \hat{J}_j defines the repulsive force between electrons through a classical interaction, while \hat{K}_j takes into account the effect of Pauli Exclusion Principle on the energy, which is a purely quantum effect produced by exchanging two electrons with the same spin. Since both \hat{J}_j and \hat{K}_j depend on the set of spin-orbitals χ_j , it is necessary using an iterative procedure, known as Self-Consistent Field (SCF), in order to solve the equations.

It could be demonstrated that the optimal HF function has to verify the equation:

$$FC = SCE \quad (2.6)$$

where F is the Fock matrix, C is the matrix containing the column vectors c_i , S the overlap matrix of χ_j and E the eigenvalues matrix whose diagonalization leads to the energy.

Hartree-Fock formalisms takes into account Pauli formalism but each electron feels only the average Coulomb repulsion of all the other electrons. Although sufficient for a qualitative description of structures, it is not considered sufficient for quantitative description of molecular systems and is therefore a branching point in the HF method.

Simplifications can be done to the HF equations leading to the semiempirical methods. In contrast, the HF approximation can be corrected by explicitly accounting for electron correlation by density functional theory (DFT), many-body perturbation theory (MBPT), configuration interaction (CI), and other Post-Hartree-Fock methods.

2.2.2 Basis functions

In 1951, Clemens Roothaan^[10] and George Hall^[11] proposed to expand the spatial part φ_i of the spin-orbitals as a linear combination of basis functions:

$$\chi_i = \sum_{i=1}^N c_{ai} \varphi_i \quad (2.7)$$

where the set of N -functions φ_i are called *basis functions set*, and have associated the coefficient c_{ai} . Thus, resolution of the HF equations 2.4 corresponds to determine the coefficients c_{ai} of the Roothaan equation 2.7, which are calculated by the SCF method.

The exact representation of the molecular orbitals φ_i implies the use a complete set of basis functions χ_i . This requires an infinite number of basis functions ($N \rightarrow \infty$) and the resolution of the HF equations 2.4 using this infinite basis functions set is known as Hartree-Fock limit. However, in practice, reaching the HF limit is impossible and therefore it is necessary to truncate the expansion to a finite number of basis functions.

The most commonly used basis functions fall in two categories: Slater-type Orbitals (STO)^[12] and Gaussian-type Orbitals (GTO).^[13] The STO functions are known to accurately describe the behavior of electrons around the nucleus, but evaluation of their integrals are more demanding to compute than GTOs. In an attempt to make calculation of integrals easier, GTO functions were introduced. Hence, instead of using individual GTO functions, linear combination of GTOs (called *primitives*) are employed in order to mimic the STO functions.

The smallest possible basis set is called the *minimal basis set*. A double- ξ (or higher order) basis set will use two (or more) basis functions per atomic orbital. Based on the fact that bonds are formed by valence orbitals, a variant of the double- ξ is by doubling those orbitals to generate the double- ξ split valence basis. This latter intends to increase

accuracy, keeping as low as possible the computational cost. In addition, basis sets can be enhanced by polarization and diffuse functions.^[14,15] Polarization functions add a basis function of higher molecular momentum, thus for example, if the valence electrons are p, one d function will be added to let the p orbital polarized, f orbitals will polarize the d ones, and so on. This can be important when using methods that take into account electronic correlation. Meanwhile, diffuse functions can be added to describe more accurately the behavior of the electrons far from the nucleus. Diffuse functions are particularly important when dealing with anions and radicals.

In the case of the heavy elements of the periodic table (mainly transition metals), these have few valence electrons compared to the number of internal electrons (or *core* electrons). Since the *core* electrons are less important in chemical reactivity, they can be represented through reasonably accurate analytical functions known as effective core potentials (ECPs) or pseudopotentials,^[16] whereas the valence electrons can be treated explicitly. In general, ECPs give good results at lower computational cost with respect to calculations involving all the electrons, and also allow incorporating relativistic effects for heavier elements. One example of effective core potentials is the LANL2DZ^[17] pseudopotential, which was employed in this thesis.

2.3 Density functional theory

Density Functional Theory (DFT) is an alternative formulation to the Hartree-Fock (HF) approximation used to evaluate the energy and other properties of a polyelectronic system. The basis of this theory rests on two fundamental mathematical theorems published by Pierre Hohenberg and Walter Kohn^[18] in 1964.

2.3.1 The Hohenberg-Kohn theorems

The first theorem states that the ground-state electronic energy and other properties of an atom or molecule are determined by its electron density function $\rho(\vec{r})$. In other words, there is a one-to-one correspondence between the electron density of a system and any ground-state property. Unlike for the wave function-based methods, the electron density only depends on three coordinates, independently of number of electrons; whereas a wave function for an N -electron system contains $3N$ coordinates, three for each electron

(four if spin is included). Thus, while the complexity of a wave function increases with the number of electrons, the electron density has the same number of variables, independently of the system size.

In the Hohenberg and Kohn formulations, the electronic ground-state energy E_0 is expressed as:

$$E_0 = E[\rho_0] = \int \rho_0(\vec{r}) V_{ne}(\vec{r}) d\vec{r} + F[\rho_0(\vec{r})] \quad (2.8)$$

where $V_{ne}(\vec{r})$ is the potential energy due to the nucleus-electron interaction, and $F[\rho_0(\vec{r})]$ is the universal functional of the electron density. The theorem is “merely” an *existence theorem*: it says that a functional $F[\rho_0(\vec{r})]$ exists, but does not tell us how to find it; this omission is the main problem with DFT. Considering the three coordinates in which the electron density depends on, this functional can be expressed as a sum of various terms:

$$F[\rho(\vec{r})] = T_s[\rho(\vec{r})] + J[\rho(\vec{r})] + E_{Ne}[\rho(\vec{r})] + E_{XC}[\rho(\vec{r})] \quad (2.9)$$

In this expression, $T_s[\rho(\vec{r})]$ is the kinetic energy of the non-interacting electrons, $J[\rho(\vec{r})]$ is the classical electron-electron repulsion, $E_{Ne}[\rho(\vec{r})]$ is the nucleus-electron interaction and $E_{XC}[\rho(\vec{r})]$ is the exchange-correlation energy. This latter functional contains terms of the kinetic correlation energy, exchange energy (consequence of Pauli Exclusion Principle) and the Coulomb correlation energy. From equation 2.9, it is only known the mathematical expression for the term $J[\rho(\vec{r})]$, while the remaining terms are unknown. This is one of the weaknesses of the DFT methodology, and indeed all theoretical efforts have been conducted in order to find a proper description for those terms, especially for the exchange-correlation energy.

It is worth noting that the above theorem only establishes a relationship between the electron density and any ground-state property of the system, but it is unhelpful in providing any indication of how to predict the density of such system. Hohenberg and Kohn demonstrated in a second theorem that the density obeys a variational principle. Through this theorem, they state that any trial electron density function ρ_t will give an energy higher than (or equal to, if it were exactly the true electron density function) the true ground-state energy:

$$E_0[\rho(\vec{r})] \leq \int \rho_t(\vec{r}) V_{ne}(\vec{r}) d\vec{r} + T_s[\rho(\vec{r})] + J[\rho(\vec{r})] + E_{xc}[\rho(\vec{r})] + E_{Ne}[\rho(\vec{r})] \quad (2.10)$$

This trial density ρ_t must satisfy two conditions: **1)** $\int \rho_t(\vec{r}) d\vec{r} = n$, where n is the number of electrons in the molecule (this is analogous to the wave function normalization condition), and **2)** $\rho_t(\vec{r}) \geq 0$ for all \vec{r} (the number of electrons per unit volume can't be negative).

Although energy calculation is possible without using the wave function, the main problem with the DFT methodology lies in that the kinetic energy and the exchange correlation energy terms that define $F[\rho(\vec{r})]$ are difficult to calculate.

2.3.2 The Kohn-Sham method

In 1965 Kohn and Sham^[17] developed an electronic state calculation method (known as the Kohn-Sham method) derived from the Hohenberg-Kohn theorems. The Kohn-Sham (KS) method is a variational approach using the electron-electron interaction potential of the density functional to give the lowest energy and the corresponding molecular orbitals and orbital energies. In this way, Kohn and Sham consider a fictitious system of non-interacting N -electrons that experiment the same potential energy $v_s(r_i)$, which makes the electron probability density of the ground state of the reference system $\rho_s(r)$ be equal to the electron probability density of the exact electronic ground state of the system studied $\rho_0(r)$:

$$\rho_s(r) = \rho_0(r) \quad (2.11)$$

Furthermore, the system of non-interacting N -electrons can be described as the summation of one-electron Hamiltonians:

$$H_s = \sum_{i=1}^N \left[-\frac{1}{2} \nabla_i^2 + v_s(r_i) \right] = \sum_{i=1}^N h_i^{KS} \quad (2.12)$$

where h_i^{KS} is the one-electron Kohn-Sham Hamiltonian. The exact wave function for this system is represented through a single Slater determinant, and the spin-orbitals φ_i^{KS} are given by the eigenvalue equation:

$$h_i^{KS} \varphi_i^{KS} = \varepsilon_i \varphi_i^{KS} \quad (2.13)$$

here, φ_i^{KS} represents the KS spin-orbitals and ε_i is the KS orbital energy. Analogous to the Hartree-Fock method, the Kohn-Sham equation 2.13 is solved through an iterative procedure (SCF). Due to the operator h_i^{KS} depends on the electron density a trial electron density function is used as initial guess. The spatial part of the KS spin-orbitals can be expanded as a linear combination of basis functions, and thus, solving the KS equations involves finding the coefficients of such lineal combination.

Because we are dealing with a non-interacting N -electron system, the exact kinetic energy is given by:

$$T_s = -\frac{1}{2} \sum_{i=1}^N \langle \varphi_i^{KS} | \nabla^2 | \varphi_i^{KS} \rangle \quad (2.14)$$

It is noteworthy that the kinetic energy of the reference system of non-interacting N -electrons is different than the real kinetic energy. Based on this, Kohn and Sham rewrote the functional $F[\rho(\vec{r})]$:

$$F[\rho(\vec{r})] = T_s[\rho(\vec{r})] + J[\rho(\vec{r})] + E_{XC}[\rho(\vec{r})] \quad (2.15)$$

where $E_{XC}[\rho(\vec{r})]$ is the so-called exchange-correlation energy, which is defined as:

$$E_{XC} = (T[\rho(\vec{r})] - T_s[\rho(\vec{r})]) + E_{Ne}[\rho(\vec{r})] \quad (2.16)$$

In equation 2.16, the terms in parenthesis indicate the correlation kinetic energy, whereas the term $E_{Ne}[\rho(\vec{r})]$ contains the non-classical electrostatic contributions. The success of the DFT methodology is to find functionals for the exchange-correlation energy E_{XC} because the exact form of such functionals is unknown. Some methods have been developed in order to find approximations to the exchange-correlation functional and are briefly described in next sections. These approximations conform the rungs of the so-called DFT Jacob's ladder, drawn by Perdew^[19] and which connects the "Hartree world" (where there is no exchange or correlation energy) with the "Heaven of Chemical Accuracy" (where the error in bonding energies are less than 1 kcal·mol⁻¹).

2.3.3 The local density approximation (LDA)

The simplest approximation to $E_{xc}[\rho(\vec{r})]$ is to assume that the density can be treated locally as a uniform electron gas (*Jellium*);^[20] the exchange-correlation energy at each point in the system is the same as that of the uniform electron gas of a same density ρ . This approximation was originally introduced by Kohn and Sham and holds for a slowly varying density. Using this approximation the exchange-correlation energy for a density ρ is given by:

$$E_{xc}^{LDA}[\rho] = \int \rho(r) \varepsilon_{xc}(\rho) dr \quad (2.17)$$

where $\varepsilon_{xc}(\rho)$ is the exchange-correlation energy per particle of a uniform electron gas of density ρ . The LDA exchange part $\varepsilon_x(\rho)$ is represented by the known exchange energy of one electron in a uniform electron gas at one particular density:

$$\varepsilon_x(\rho) = -\frac{3}{4} \left(\frac{3}{\pi} \right)^{1/3} (\rho(r))^{1/3} \quad (2.18)$$

Thus, the LDA exchange energy becomes:

$$E_x^{LDA}[\rho] = -\frac{3}{4} \left(\frac{3}{\pi} \right)^{1/3} \int [\rho(r)]^{4/3} dr \quad (2.19)$$

However, there is no analytical expression for the correlation part $\varepsilon_c(\rho)$ and therefore a variety of LDA functionals were derived from very accurate Monte-Carlo simulations for a homogeneous electron gas.^[21] Such functionals were obtained using different analytic expressions for the correlation part as Vosko-Wilk-Nusair (VWN),^[22] Perdew-Zunger (PZ81),^[23] Cole-Perdew (CP),^[24] Perdew-Wang (PW92),^[25] etc.

The spin-polarized version of LDA is termed as Local-Spin Density Approximation (LSDA). This approach allows difference between the spatial parts of ρ^α and ρ^β for atoms and molecules with unpaired electrons:

$$E_{xc}^{LSDA}[\rho^\alpha, \rho^\beta] = \int \varepsilon_{xc}(\rho^\alpha, \rho^\beta) \rho(r) d^3r \quad (2.20)$$

2.3.4 The generalized gradient approximation (GGA)

Since both methods LDA and LSDA approximate the energy of the true density by the energy of a local constant density, it fails in situations where the density undergoes rapid changes, such as in molecules. An improvement to this can be made by considering the gradient of the electron density; thus arises, the so-called Generalized Gradient Approximation (GGA). Mathematically this can be written as:

$$E_{xc}^{GGA}[\rho] = \int \rho(r) \varepsilon_{xc}[\rho(r), \nabla \rho(r)] dr \quad (2.21)$$

GGA can also be extended to spin-polarised systems:

$$E_{xc}^{GGA}[\rho^\alpha, \rho^\beta] = \int \varepsilon_{xc}(\rho^\alpha, \rho^\beta, \nabla \rho^\alpha, \nabla \rho^\beta) \rho(r) d^3r \quad (2.22)$$

One of the earliest and most popular GGA exchange functionals E_x^{GGA} was proposed by A. D. Becke (B or B88) as a correction to the LSDA exchange energy.^[26] Other E_x^{GGA} functionals were introduced by Perdew and Wang in 1986 (PW86 or PWx86)^[27] and 1991 (PWx91).^[28] Examples of GGA correlation functionals E_c^{GGA} are the LYP (Lee, Yang and Parr)^[29] and the P86 (Perdew 1986)^[30] functionals.

2.3.5 The meta generalized gradient approximation (m-GGA)

The *meta*-GGA is essentially an extension of the GGA by including the second derivative of the density (Laplacian, ∇^2) to the exchange-correlation energy. In these functionals, the non-interacting kinetic energy density τ_S is used as input to the functional as well as the electron density and its gradient. The spin-independent form of this functional is thus:

$$E_{xc}^{m-GGA}[\rho] = \int \rho(r) \varepsilon_{xc}[\rho(r), \nabla \rho(r), \nabla^2 \rho(r), \tau_S(r)] dr \quad (2.23)$$

One of the earliest attempts to include kinetic energy functionals was by Becke and Roussel (BR).^[31] Some other examples of *meta*-GGA functionals are the TPSS (Tao-Perdew-Staroverov-Scuseria),^[32] PKZB (Perdew-Kurth-Zupan-Blaha),^[33] VSXC (Voorhis-Scuseria)^[34] and the B96 (Becke)^[35] functionals.

2.3.6 The hybrid generalized gradient approximation (H-GGA)

An additional step in the accuracy of finding approximations to the exchange-correlation potential is reached by combination of GGA methods with a percentage of exchange as described by the HF theory. Such functionals are called Hybrid-GGA (or H-GGA). This percentage of exchange that has to be included is essentially empirical. An example of H-GGA functionals is the well-known B3LYP functional (from combination of the B88 and LYP functionals), which contains three parameters ($a=0.20$, $b=0.72$ and $c=0.81$) that have been taken without modification from Becke's original fitting of the analogous B3PW91 functional to a set of atomization energies, ionization potentials, proton affinities, and total atomic energies. The exchange-correlation energy of the B3LYP functional is given by:

$$E_{xc}^{B3LYP} = (1 - a)E_x^{LSDA} + aE_x^{HF} + b\Delta E_x^{B88} + (1 - c)E_c^{LSDA} + cE_c^{LYP} \quad (2.24)$$

The B3LYP functional is so far one of the most used functionals in DFT calculations because of its robustness for describing many chemical properties.

A new class of functional called meta-hybrid GGA are nowadays in development. Those functionals use the first derivative of ρ and its second derivative, or the kinetic energy density, and HF exchange. They are the highest-level functionals in routine use. An example is the M06 suite of functionals, which are briefly described in next section.

2.4 Methods used for including dispersion into DFT calculations

Many successes have been achieved through the use of DFT methods in chemical reactivity. Although today DFT is the most widely used theoretical approach to molecular structure, this method consistently includes exchange-correlation effects, in an approximate way, for short intermolecular distances. However, there are still difficulties for describing medium-range, and long-range (non-covalent) interactions such as the van der Waals interactions, weak hydrogen bonds and π - π stacking interactions.

Below are described two well-established methods for including dispersion corrections into DFT calculations: these are the proposals by Donald Truhlar and Stefan Grimme.

2.4.1 Parameterized dispersion correction by Truhlar: Minnesota functionals

One of the most common ways nowadays to include dispersion effects in DFT functionals is by introducing certain empirical parameters that are adjusted to take into account such dispersion forces. That kind of functionals (the M06 family) were mainly developed by the group of Donald Truhlar at the University of Minnesota, thus they are known as the Minnesota functionals. The M06 suite of functionals are a set of four meta-hybrid GGA DFT functionals that are constructed with empirical fitting of their parameters, but constraining to the uniform electron gas. The family includes the functionals M06,^[36] M06-L,^[37] M06-2X^[36] and M06-HF,^[38] with a different amount of exact exchange on each one. M06-L is fully local without HF exchange (thus it cannot be considered hybrid), M06 has 27% of HF exchange, M06-2X 54% and M06-HF 100%.

The exchange-correlation energy for the M06 functional can be written as:

$$E_{XC}^{hyb} = \frac{X}{100} E_X^{HF} + \left(1 - \frac{X}{100}\right) E_X^{M06} + E_C^{M06} \quad (2.25)$$

The M06 and M06-2X functionals were used in some parts of this thesis. The utilities and advantages of M06 are for main group thermochemistry and non-covalent interactions, transition metal thermochemistry and organometallics. It is usually the most versatile of the 06 functionals and because of this large applicability, it can be slightly worse than M06-2X for specific properties that require high percentage of HF exchange, such as thermochemistry and kinetics.

2.4.2 Empirical dispersion correction by Grimme

In this methodology developed by Stefan Grimme,^[39] the dispersion corrected total energy is calculated as:

$$E_{DFT-D} = E_{KS-DFT} + E_{disp} \quad (2.26)$$

where E_{KS-DFT} is the usual energy obtained with any KS functional above described and E_{disp} is an empirical dispersion correction given by:

$$E_{disp} = -s_6 \sum_{i=1}^{N-1} \sum_{j=i+1}^N \frac{C_6^{ij}}{R_{ij}^6} f_{dmp}(R_{ij}) \quad (2.27)$$

Here, N is the number of atoms in the system, C_6^{ij} denotes the dispersion coefficient for atom pair ij , s_6 is a global scaling factor (which only depends on the functional used) and R_{ij} is the interatomic distance. The term f_{dmp} is a damping function that decays at small R fast enough to zero such that the dispersion corrections between atoms well below typical van der Waals distances are negligible and thus, “normal” bonds are not significantly affected by the correction. The damping function f_{dmp} is given by:

$$f_{dmp}(R) = \frac{1}{1 + e^{-\alpha(R/R_0-1)}} \quad (2.28)$$

In this expression, R_0 is the sum of atomic van der Waals radii.

Some variants to the original formulation were also introduced by Grimme et al.^[40] In the DFT-D2^[40a] variant, dispersion coefficients, C_6^{ij} , obtained from the geometric mean of tabulated elemental values, are summed over interatomic distances, R_{ij} , modulated by a damping function, f_{dmp} , that gradually activates the dispersion correction (at a rate characterized by α_6) over a distance characterized by the sum of the two atomic vdW radii, R_0 , while an overall scaling term, s_6 , is optimized to be unique to each E_{XC} functional. Empirical dispersion correction for DFT-D2 E_{disp}^{D2} takes the explicit form:

$$E_{disp}^{D2} = -s_6 \sum_{i,j>i}^N \frac{C_6^{ij}}{R_{ij}^6} f_{dmp}(R_{ij}) \quad (2.29)$$

and the new damping function is given by:

$$f_{dmp}(R) = \frac{1}{1 + e^{-\alpha_6(R/R_0-1)}} \quad (2.30)$$

Grimme recently presented a refined method, DFT-D3,^[40b] which incorporates an additional R^{-8} term in the dispersion series and adjusts the C_6^{ij} combination formula and damping function. The individual atomic C_6^i are interpolated from several reference values based upon coordination numbers extracted from the molecular structure, rather than assigned solely by atomic identity as in DFT-D2, and thereby incorporate some awareness

of the chemical environment into an otherwise largely heuristic correction. The DFT-D3 dispersion has the following form, where s_r , s_6 and s_8 are the usual non-unity parameters fitted for individual functionals:

$$E_{disp}^{D3ZERO} = - \sum_{n=6,8} s_n \sum_{i,j>i}^N \frac{C_n^{ij}}{R_{ij}^n} f_{dmp}(R_{ij}) \quad (2.31)$$

$$f_{dmp}(R) = \frac{1}{1 + 6(R_{ij} / (s_r n R_0^j))^{-\alpha_n}} \quad (2.32)$$

Even more recently, a modified damping scheme for DFT-D3 using the rational damping form of Becke and Johnson was introduced.^[40c] The parameters fit for individual functionals are now s_6 , s_8 , α_1 , α_2 :

$$E_{disp}^{D3BJ} = - \sum_{n=6,8} s_n \sum_{i,j>i}^N \frac{C_n^{ij}}{R_{ij}^n + (f_{dmp})^n} \quad (2.33)$$

$$f_{dmp} = \alpha_1 \sqrt{\frac{C_8^{ij}}{C_8^{ij}}} + \alpha_2 \quad (2.34)$$

Some functionals including Grimme's empirical dispersion were used in this thesis, like B97D (includes the -D2 variant), ω B97XD (includes the -D3ZERO variant) and B97D3 (includes the -D3BJ variant).

2.5 Potential energy surface (PES)

The Potential Energy Surface (PES) can be thought of as a conceptual tool for aiding the analysis of molecular structure and chemical reactivity. As already indicated in section 2.2, the PES concept arises from the Born-Oppenheimer approximation, and basically describes the potential energy hypersurface defined by a collection of atoms in terms of certain parameters, normally the positions of the atoms.

PES are important because they help us in visualizing and understanding the relationship between potential energy and molecular geometry, and in understanding how computational chemistry programs locate and characterize structures of interest. Among the main tasks of computational chemistry are to determine the structure and energy of

molecules and of the transition states involved in chemical reactions: our “structures of interest” are molecules and the transition states linking them.

A PES contains several points along the reaction coordinate, but from a chemical point of view, the most significant are the so-called *stationary points* that essentially correspond to *local energy minima* or *local minima* and first-order *saddle points*. Mathematically, a minimum is a minimum in all directions, but a saddle point is a maximum along the reaction coordinate and a minimum in all other directions. Chemically, the saddle points stand for transition state structures that are connected by two local minima (called intermediates), and which have important meaning in chemical reactivity. The characterization of stationary points either as local minima or transition states is conducted computationally through calculation of the Hessian matrix, which is the square matrix of second-order partial derivatives of the energy with respect to the nuclear position (also called force constant matrix). If all eigenvalues resulting of the diagonalization of the Hessian matrix are positive, the structure corresponds to a minimum, whereas if one (and only one) of those eigenvalues is negative, the structure corresponds to a transition state.

2.6 Thermodynamic properties

2.6.1 Ensemble properties and basic statistical thermodynamics

Thermodynamic data are crucial in the understanding and design of chemical processes. Next to the experimental evaluation of such data, computational methods are valuable and sometimes indispensable tools in obtaining some of the fundamental variables of thermodynamics such as zero-point energy, enthalpy, entropy, Gibbs free energy, and others. While electronic-structure calculations are usually performed on single molecules, experimental data are obtained with macroscopic quantities of matter that are made up of unimaginably large number of molecules. Therefore, connection between the microscopic and macroscopic regimes is required.^[14,15] This bridge is provided by the *statistical thermodynamics*.

Statistical thermodynamics involves a series of formulations for calculating the thermodynamic properties of such ensembles of molecules. Its key feature is the *partition function* Q , which is obtained according to the well-known canonical ensemble, in which

the constants are the total number of particles N , the volume V , and the temperature T . This partition function is written as:

$$Q(N, V, T) = \sum_i e^{-E_i(N, V)/k_B T} \quad (2.35)$$

where i runs over all possible energy states of the system having energy E_i and K_B is the Boltzmann's constant.

Once the partition function is known, thermodynamic functions such as the internal energy U and Helmholtz free energy A may be calculated according to:

$$\begin{aligned} U &= k_B T^2 \left(\frac{\partial \ln Q}{\partial T} \right)_V \\ A &= -k_B T \ln Q \end{aligned} \quad (2.36)$$

Macroscopic observables, such as pressure P or heat capacity at constant volume C_V , may be calculated as derivatives of thermodynamic functions:

$$\begin{aligned} P &= - \left(\frac{\partial A}{\partial V} \right)_T = k_B T \left(\frac{\partial \ln Q}{\partial V} \right)_T \\ C_V &= \left(\frac{\partial U}{\partial T} \right)_V = 2k_B T \left(\frac{\partial \ln Q}{\partial T} \right)_V + k_B T^2 \left(\frac{\partial^2 \ln Q}{\partial T^2} \right)_V \end{aligned} \quad (2.37)$$

Other thermodynamic functions like the enthalpy H , the entropy S and Gibbs free energy G , may be constructed from above relations:

$$\begin{aligned} H &= U + PV = k_B T^2 \left(\frac{\partial \ln Q}{\partial T} \right)_V + k_B TV \left(\frac{\partial \ln Q}{\partial V} \right)_T \\ S &= \frac{U - A}{T} = k_B T \left(\frac{\partial \ln Q}{\partial T} \right)_V + k_B \ln Q \\ G &= H - TS = k_B TV \left(\frac{\partial \ln Q}{\partial V} \right)_T - k_B \ln Q \end{aligned} \quad (2.38)$$

In order to obtain the partition function Q , it is assumed that the ensemble behaves like an ideal gas, so molecules do not interact with one another. Consequently, the many-body problem is reduced from finding the ensemble partition function Q to finding the

molecular partition function q_M . The total partition function q_M is defined as a product of the individual contributions of the electronic, translational, rotational and vibrational terms:

$$q_M = q_{elec} q_{trans} q_{rot} q_{vib} \quad (2.39)$$

The electronic partition function q_{elec} is usually the simplest to compute. To evaluate the remaining partition functions, some additional approximations are made. Thus for example, for calculating q_{trans} it is assumed that the molecule acts as a particle in a three-dimensional cubic box, the rigid rotor is taken to solving q_{rot} , and the harmonic oscillator to find q_{vib} .

2.6.2 Standard state modifications

Ideal gas assumption is considered in order to obtain the different molecular partition functions. Hence, all the equations used in electronic-structure calculations are applicable to a hypothetical ideal gas at concentrations equivalent to standard state, where pressure $P = 1$ atm. Because of this choice, we may replace V by RT/P and specify a standard state pressure instead, corresponding to a standard-state molar volume of 24.5 L at 298.15 K. Thus, a concentration of 1/24.5 M can be derived from the well-known expression:

$$\frac{n}{V} = \frac{P}{RT} \quad (2.40)$$

This logarithmic concentration is used to calculate the translational entropy contribution S_{trans} by means of the partition function:

$$q_{trans} = \left(\frac{2\pi mRT}{h^2} \right)^{3/2} \frac{RT}{P} \quad (2.41)$$

In real chemical processes where an ensemble of molecules are interacting each other or with the solvent medium, the ideal gas-phase translational entropy significantly overestimates the condensed-phase translational entropy, as a result of the restriction of motion of molecules in solution.^[41] In addition, we do not have solutions whose concentration is 1/24.5 M, and therefore it is necessary to obtain results applicable at the

concentration of the system under study. At this point it should be highlighted that accurate prediction of the translational entropy contribution S_{trans} to the total entropy in solution is still challenging in electronic-structure calculations, and so far no standard approach is available. However, many authors have proposed some methods for dealing with this issue, as discussed below.

The most simple of these approximations is maybe the one introduced by Morokuma and coworkers.^[42] They suggest neglecting directly the translational entropy term in the calculation of the total entropy in solution.

Alternatively, Martin and coworkers^[43] proposed to determine the pressure $P = \frac{n}{V}RT$ (from equation 2.40) applicable at the concentration of the solvent used from its experimental density. Thus, for example the liquid water, with a density $\rho = 997.02 \text{ kg}\cdot\text{m}^{-3}$, requires a pressure of 1354 atm to correct the aqueous solution concentration. The actual concentration (1354 atm/ RT) is incorporated then to the calculation of the translational partition function in equation 2.41. By applying this approximation for the solvent 1,2-epoxyhexane ($\rho = 831.0 \text{ kg}\cdot\text{cm}^{-3}$) we obtained a pressure of 203 atm, which is used for adjusting the solvent concentration of the gas-phase entropy in the reactions studied in Chapter 5.

The third approximation employed in this thesis (Chapter 5) is the method of Wertz^[44] and Ziegler,^[45] which is broken up into three steps. In the first step based on this method, the ideal-gas solute is compressed from standard conditions (having a molar volume $V_{m,gas}$ of $24450 \text{ mL}\cdot\text{mol}^{-1}$) to the standard volume of the solvent ($V_{m,liq}$). Then the compressed solute gas is transferred to the solvent, forming a hypothetical solution that has the intermolecular interactions of a dilute solution. In this step the solute loses the same fraction of its entropy as would be lost by the solvent in going from gas (at its liquid-phase density) to liquid. This fraction α can be calculated by use of equation 2.42, in which the numerator represents the change in entropy in the process of transfer. In the third step, the solute is expanded to the concentration of the desired solution (i.e., $1.0 \text{ mol}\cdot\text{L}^{-1}$, and thus having molar volume of $V_m^\circ = 1000 \text{ mL}\cdot\text{mol}^{-1}$).

The solute entropy change for the first and third steps, which are strictly changes in molar volume, is given by $\Delta S = R \ln(V_{m,f}/V_{m,i})$, where $V_{m,f}$ is the final solute molar volume

and $V_{m,i}$ is the initial solute value. The entropy fraction α lost in the second step can be determined from the absolute entropies of the solvent in its gas (S_{gas}°) and liquid (S_{liq}°) phases (see Table 2.1), as shown in equation 2.42:

$$\alpha = \frac{S_{\text{liq}}^{\circ} - (S_{\text{gas}}^{\circ} + R \ln V_{m,\text{liq}}/V_{m,\text{gas}})}{S_{\text{gas}}^{\circ} + R \ln V_{m,\text{liq}}/V_{m,\text{gas}}} \quad (2.42)$$

Substituting the appropriate parameters for 1,2-epoxyhexane^[46] (see Table 2.1) in equation 2.42, we have $\alpha = -0.19$. The sum of the entropy changes involved in each of the three steps then gives the total solvation entropy. Using the data reported in Table 2.1 we are able to calculate the entropy ($\text{cal}\cdot\text{mol}^{-1}\cdot\text{K}^{-1}$) of solvation for a given species of the reaction in 1,2-epoxyhexane ΔS_{sol} , at a temperature of 298.15 K:

$$\Delta S_{\text{sol}} = (-10.56 \text{ cal}\cdot\text{mol}^{-1}\cdot\text{K}^{-1}) - 0.19(S_{\text{gas}}^{\circ} - 10.56 \text{ cal}\cdot\text{mol}^{-1}\cdot\text{K}^{-1}) + (4.20 \text{ cal}\cdot\text{mol}^{-1}\cdot\text{K}^{-1}) \quad (2.43)$$

Table 2.1 Experimental data^[46] for the solvent 1,2-epoxyhexane used in equations 2.42 and 2.43.

M^a ($\text{g}\cdot\text{mol}^{-1}$)	ρ^a ($\text{kcal}\cdot\text{mol}^{-1}$)	$S_{\text{liq}}^{\circ b}$ ($\text{J}\cdot\text{mol}^{-1}\cdot\text{K}^{-1}$)	$S_{\text{gas}}^{\circ b}$ ($\text{kcal}\cdot\text{mol}^{-1}$)	$R \ln V_{m,\text{liq}}/V_{m,\text{gas}}$ ($\text{cal}\cdot\text{mol}^{-1}\cdot\text{K}^{-1}$)	$R \ln V_m^{\circ}/V_{m,\text{liq}}$ ($\text{cal}\cdot\text{mol}^{-1}\cdot\text{K}^{-1}$)
100.16	0.831	196.27	287.40	-10.56	4.20

^a These values were taken from the thermochemistry data for propylene oxide. ^b These values were considered for 1,2-epoxyhexane.

2.7 Evaluation of solvent effects

In general, most of chemical reactions are carried out in the presence of a solvent, which sometimes plays a vital role as for example, in stabilizing species in the reaction, acting as reactant, etc. Hence, in order to study chemical reactions is very important an appropriate description of the solvent effects. There are two conventional ways to include solvent effects in electronic-structures calculations: one is by considering the individual solvent molecules explicitly and another where the solvent is treated as a *continuous medium*. The former implies a high computational cost since it involves dealing with a high number of molecules, which increases the number of degrees of freedom. In addition, some extra

errors could be added to the calculations as for instance, either the way that the molecules are placed around the reactant species or the number of molecules that should be considered.

The second alternative (implicit treatment of molecules) is most commonly used, and is called *continuum methods*. Among such methods, the *Self-Consistent Reaction Field (SCRF)*^[47] method is perhaps the most widely used. In this method, the solvent is considered as a uniform polarizable medium with a dielectric constant ϵ (also known as relative permittivity, ϵ_r), where the solute is placed in a suitable shaped cavity inside a dielectric medium. The latter acts back on the solute, and thus, producing an electrostatic stabilization. The method is iteratively repeated until the mutual polarization between the solute and solvent reach the self-consistency.

The solvation *free energy* ΔG_{sol} in the SCRF method is calculated as a sum of different energy contributions:

$$\Delta G_{sol} = \Delta G_{cav} + \Delta G_{disp} + \Delta G_{rep} + \Delta G_{el} \quad (2.44)$$

where ΔG_{cav} is the cavitation energy, i.e., the energy needed to create the cavity for the solute (it is a destabilizing term and therefore is always positive), ΔG_{disp} is the dispersion energy between solute and solvent that contributes positively to the solvation (it is stabilizing term), ΔG_{rep} is associated to the repulsive interactions between solute and solvent (it is also a destabilizing term). Finally, the term ΔG_{el} is a stabilizing term, which correspond to the electrostatic interactions due to the instantaneous polarization caused by the charge distribution of the solute molecules in the solvent, and vice versa.

There are several SCRF methods for calculating solvation energies. However, only the *Polarizable Continuum Model (PCM)*^[48] and the *Conductor-like Screening Model (COSMO)*^[49] were used in this thesis. In the first model (PCM), the cavity is constructed as an assembly of atom-centered overlapping spheres with radius approximately 1.2 times larger than the van der Waals radius. Alternatively, the COSMO model is a variant of the continuum solvation models, which uses a much simpler boundary condition of vanishing electrostatic potential for a scaled conductor ($\epsilon \rightarrow \infty$) in the calculation of the polarization charges of a molecule in a continuum.

In all PCM methods, the radii of the spheres used to create the cavity can be further defined in different ways, but only the UFF radii was considered in this thesis. UFF uses the united atom topological model applied on atomic radii of the UFF force field for heavy atoms and describes the hydrogen atoms as individual spheres (explicit hydrogens).

In the course of this thesis, all geometries studied were fully optimized in gas phase. Solvent effects are incorporated in the results by adding a PCM single-point on the final gas-phase geometry obtained after optimization. The Gibbs free energy in solvent ΔG_{sol} can be obtained by using the following scheme:

$$\Delta G_{sol} = \Delta G_{gas} + (\Delta E_{gas} - \Delta E_{sol}) \quad (2.45)$$

2.8 Methods used in ion mobility mass spectrometry (IM-MS)

The algorithms used in this thesis to theoretically calculate collision cross sections (CCS) are based in three main methods: the Trajectory Method (TM),^[50] the Projection Approximation (PA),^[51] and the Exact Hard-Spheres Scattering (EHSS).^[52]

The most accurate (and therefore, computationally expensive) of those methods is the Trajectory Method TM, which models the ion as a collection of atoms, each one represented by a 12-6-4 potential (Lennard-Jones + ion-induced dipole). TM seeks the cross section $\Omega_{avg}^{(1,1)}$ that is related to the scattering angle χ , which is the angle between the trajectory before and after a collision between the ion and a buffer gas atom (usually helium). $\Omega_{avg}^{(1,1)}$ is obtained by integrating the momentum transfer cross section over the relative velocities g and the impact parameter b for all possible ion orientations defined by the three angles θ , ϕ , and γ :

$$\Omega_{avg}^{(1,1)} = \frac{1}{8\pi^2} \int_0^{2\pi} d\theta \int_0^\pi d\phi \sin \phi \int_0^{2\pi} d\gamma \frac{\pi}{8} \left(\frac{\mu}{k_B T} \right)^3 \int_0^\infty dg e^{-\mu g^2 / (2K_B T)} g^5 \int_0^\infty db 2b(1 - \cos \chi(\theta, \phi, \gamma, g, b)) \quad (2.46)$$

where μ is the reduced mass. Since the scattering angle $\chi(\theta, \phi, \gamma, g, b)$ depends on the pairwise potential between the ion and the buffer gas molecules, the accuracy of computed cross-section values is determined by the quality of the interaction potential

model. The potential term employed in this method is based on the two body 12-6-4 potential model:

$$\Phi(\theta, \phi, \gamma, b, r) = 4\varepsilon_i \sum_i^n \left[\left(\frac{\sigma_i}{r_i} \right)^{12} - \left(\frac{\sigma_i}{r_i} \right)^6 \right] - \frac{\alpha}{2} \left(\frac{ze}{n} \right)^2 \left[\left(\sum_i^n \frac{x_i}{r_i^3} \right)^2 + \left(\sum_i^n \frac{y_i}{r_i^3} \right)^2 + \left(\sum_i^n \frac{z_i}{r_i^3} \right)^2 \right] \quad (2.47)$$

here, the first term (short-range van der Waals interactions) is a sum of the Lennard-Jones (12-6) potential between a gas buffer atom and individual atom i in the molecular ion. The Lennard-Jones parameters, ε_i (depth of the potential) and σ_i (finite distance at which the inter-particle potential is zero) are usually obtained by fitting measured mobilities as a function of temperature. The second term represents the long-range ion-induced dipole interactions, in which α is the polarizability of the buffer gas atom, n is the number of atoms in the ion, and r_i , x_i , y_i and z_i are coordinates that define the relative positions of the atoms with respect to the buffer gas atom. The effective potential is further obtained by summing over the individual atomic contributions and trajectories are run in this potential to obtain the scattering angle. Thus, the orientationally averaged collision integral $\Omega_{\text{avg}}^{(1,1)}$ is determined by averaging over all possible collision geometries.

A common, computationally efficient, approximation for equation 2.46 is to assume that both the individual atoms in the molecular ion and the buffer atom are hard spheres. Thus, the orientationally averaged hard-sphere collision integral $\Omega_{\text{avg}}^{(1,1)}$ is approximated by:

$$\Omega_{\text{avg}}^{(1,1)} \approx \frac{1}{8\pi^2} \int_0^{2\pi} d\theta \int_0^\pi d\phi \sin \phi \int_0^{2\pi} d\gamma \pi b_{\text{min}}^2 \quad (2.48)$$

where b_{min} is the minimum impact parameter for a collision geometry defined θ , ϕ , and γ that avoids a hard sphere contact with any atom of the ion. This model is known as the hard sphere projection approximation (PA). Besides ignore the long-range interactions between the ion and the buffer gas atom, this approach also ignore all the details of the scattering process and effectively replaces the collision integral with the collision integral of a sphere of the same average projection as that of the polyatomic ion. It has been shown that for any finite, locally convex surface, the exact orientationally averaged hard

sphere collision integral Ω_{avg}^{HS} is equal to the orientationally averaged projection, P ($\Omega_{\text{avg}}^{HS} = \int db 2b(1 - \cos \chi) = \pi b_{\text{min}}^2$), and therefore, the hard sphere projection approximation is exact. However, for bodies with partially concave surfaces this equality does not hold ($\Omega \neq P$), and multiple scattering and shadowing can occur. Thus, a rigorous hard sphere scattering model was developed which accurately accounts for the details of the scattering process. This is accomplished by solving equation 2.48 numerically:

$$\Omega_{\text{avg}}^{(1,1)} = \frac{1}{8\pi^2} \int_0^{2\pi} d\theta \int_0^\pi d\phi \sin \phi \int_0^{2\pi} d\gamma \int_0^\infty db 2b(1 - \cos \chi(\theta, \phi, \gamma, g, b)) \quad (2.48)$$

where χ is the aforementioned scattering angle. This model is called the Exact Hard Sphere Scattering (EHSS) and considers the ions as a collection of overlapping hard spheres with radii equal to hard-sphere collision distances. The orientationally-averaged momentum transfer cross section is calculated by determining the scattering angles between the incoming buffer gas atom trajectory and the departing buffer gas atom trajectory.

As stated above, TM should give the most reliable estimation. Furthermore, the PA model generally gives numbers that are smaller than TM, while EHSS generally gives values that are greater than those obtained by TM. The deviations increase with increasing size of the ion. This is because the PA ignores multiple scattering (where the ion and buffer gas have more than one encounter) and EHSS tends to overestimate the effects of multiple scattering.

2.9 References and notes

- [1] *Computational chemistry: Introduction to theory and applications of molecular and quantum mechanics*, E. G. Lewars (Ed.), 2nd Edition, Springer, Dordrecht **2011**.
- [2] G. Cuevas, F. Cortés, *Introducción a la Química Computacional*, Fondo de cultura económica, México D.F. **2003**.
- [3] *Computational modeling of homogeneous catalysis*, F. Maseras, A. Lledós (Eds.), Vol. 25, Kluwer Academic Publishers, Dordrecht **2002**.
- [4] *Computational modeling for homogeneous and enzymatic catalysis*, K. Morokuma, D. G. Musaev (Eds.), Wiley-VCH, Weinheim **2008**.
- [5] T. K. Woo, P. M. Margl, L. Deng, L. Cavallo, T. Ziegler, *Catalysis Today* **1999**, *50*, 479.
- [6] E. Schrödinger, *Phys. Rev.* **1926**, *28*, 1049.
- [7] M. Born, J. R. Oppenheimer, *Ann. Phys.* **1927**, *84*, 457.
- [8] D. R. Hartree, *Proc. Camb. Philos. Soc.* **1928**, *24*, 89.
- [9] A. Szabo, N. S. Ostlund, *Modern Quantum Chemistry: Introduction to Advanced Electronic Structure Theory*, Dover Publications, New York **1982**.
- [10] C. C. J. Roothaan, *Rec. Mod. Phys.* **1951**, *23*, 69.
- [11] G. G. Hall, *Proc. R. Soc. A* **1951**, *205*, 541
- [12] J. C. Slater, *Phys. Rev.* **1930**, *36*, 57.
- [13] S. F. Boys, *Proc. R. Soc. Lond. A* **1950**, *200*, 542.
- [14] C. J. Cramer, *Essentials of Computational Chemistry: Theories and Models*, 2nd Edition, John Wiley & Sons, Chichester **2004**.
- [15] F. Jensen, *Introduction to Computational Chemistry*, 2nd Edition, John Wiley & Sons, Chichester **2007**.
- [16] H. Hellmann, *J. Chem. Phys.* **1935**, *3*, 61.
- [17] P. J. Hay, W. R. Wadt, *J. Chem. Phys.* **1985**, *82*, 270.
- [18] W. Kohn, L. J. Sham, *Phys. Rev. A* **1965**, *140*, 1133.
- [19] J. P. Perdew, A. Ruzsinszky, L. A. Constantin, J. W. Sun, G. I. Csonka, *J. Chem. Theory Comput.* **2009**, *5*, 902.

- [20] *Jellium* is a hypothetical electrically neutral system with infinite volume, consisting of an infinite number of interacting electrons moving in a space through which the positive charge is distributed continuously and uniformly. For further information see a) L. H. Thomas, *Proc. Camb. Philos. Soc.* **1927**, 23, 542; b) E. Fermi, *Rend. Accad. Naz. Lincei* **1927**, 6, 602; c) Dirac, P. A. M. *Proc. Camb. Philos. Soc.* **1930**, 26, 376.
- [21] D. M. Ceperley, B. J. Alder, *Phys. Rev. Lett.* **1980**, 45, 566.
- [22] S. H. Vosko, L. Wilk, M. Nusair, *Can. J. Phys.* **1980**, 58, 1200.
- [23] J. P. Perdew, A. Zunger, *Phys. Rev. B* **1981**, 23, 5048.
- [24] L. A. Cole, J. P. Perdew, *Phys. Rev. A* **1982**, 25, 1265.
- [25] J. P. Perdew, Y. Wang, *Phys. Rev. B* **1992**, 45, 13244.
- [26] A. D. Becke, *Phys. Rev. A* **1988**, 38, 3098.
- [27] J. P. Perdew, W. Yue, *Phys. Rev. B* **1986**, 33, 8800.
- [28] J. P. Perdew, J. A. Chevary, S. H. Vosko, K. A. Jackson, M. R. Pederson, D. J. Singh, C. Fiolhais, *Phys. Rev. B* **1992**, 46, 6671.
- [29] a) C. T. Lee, W. T. Yang, R. G. Parr, *Phys. Rev. B* **1988**, 37, 785, b) B. Miehlich, A. Savin, H. Stoll, H. Preuss, *Chem. Phys. Lett.* **1989**, 157, 200.
- [30] J. P. Perdew, *Phys. Rev. B* **1986**, 33, 8822.
- [31] A. D. Becke, M. R. Roussel, *Phys. Rev. A* **1989**, 39, 3761.
- [32] J. M. Tao, J. P. Perdew, V. N. Staroverov, G. E. Scuseria, *Phys. Rev. Lett.* **2003**, 91.
- [33] J. P. Perdew, S. Kurth, A. Zupan, P. Blaha, *Phys. Rev. Lett.* **1999**, 82, 2544.
- [34] T. Van Voorhis, G. E. Scuseria, *J. Chem. Phys.* **1998**, 109, 400.
- [35] A. D. Becke, *J. Chem. Phys.* **1996**, 104, 1040.
- [36] Y. Zhao, D. G. Truhlar, *Theor. Chem. Acc.* **2008**, 120, 215.
- [37] Y. Zhao, D. G. Truhlar, *J. Chem. Phys.* **2006**, 125.
- [38] Y. Zhao, D. G. Truhlar, *J. Phys. Chem. A* **2006**, 110, 13126.
- [39] S. Grimme, *J. Comp. Chem.* **2004**, 25, 1463.
- [40] a) S. Grimme, *J. Comp. Chem.* **2006**, 27, 1787; b) S. Grimme, J. Antony, S. Ehrlich, H. Krieg, *J. Chem. Phys.* **2010**, 132, 154104; c) S. Grimme, S. Ehrlich, L. Goerigk, *J. Comp. Chem.* **2011**, 32, 1456.

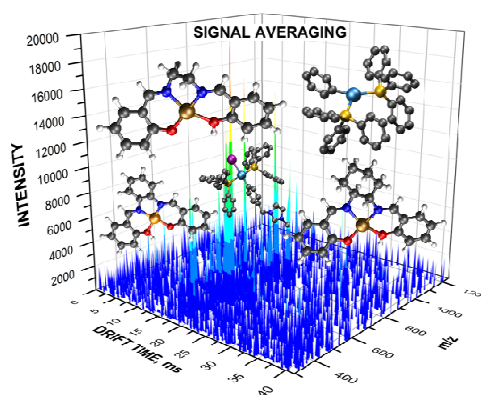
- [41] For discussion on entropy overestimation in solution, see: a) J. Hermans, L. Wang, *J. Am. Chem. Soc.* **1997**, *119*, 2707; b) Z.-X. Yu, K. N. Houk, *J. Am. Chem. Soc.* **2003**, *125*, 13825; c) Y. Chen, S. Ye, L. Jiao, Y. Liang, D. K. Sinha-Mahapatra, J. W. Herndon, Z.-X. Yu, *J. Am. Chem. Soc.* **2007**, *129*, 10773; d) Y. Liang, S. Liu, Y. Xia, Y. Li, Z.-X. Yu, *Chem. Eur. J.* **2008**, *14*, 4361; e) S. Qu, Y. Dang, C. Song, M. Wen, K.-W. Huang, Z.-X. Wang, *J. Am. Chem. Soc.* **2014**, *136*, 4974; f) M.-A. Courtemanche, M.-A. Légaré, L. Maron, F.-G. Fontaine, *J. Am. Chem. Soc.* **2014**, *136*, 10708.
- [42] R. Tanaka, M. Yamashita, L. W. Chung, K. Morokuma, K. Nozaki, *Organometallics* **2011**, *30*, 6742.
- [43] R. L. Martin, P. J. Hay, L. R. Pratt, *J. Phys. Chem. A* **1998**, *102*, 3565.
- [44] D. H. Wertz, *J. Am. Chem. Soc.* **1980**, *102*, 5316.
- [45] a) J. Cooper, T. Ziegler, *Inorg. Chem.* **2002**, *41*, 6614; b) G. Morales, R. Martínez, T. Ziegler, *J. Phys. Chem. A* **2008**, *112*, 3192.
- [46] NIST Chemistry WebBook, at <http://webbook.nist.gov/chemistry/>
- [47] J. Tomasi, M. Persico, *Chem. Rev.* **1994**, *94*, 2027.
- [48] a) S. Miertus, E. Scrocco, J. Tomasi, *J. Chem. Phys.* **1981**, *55*, 117; b) M. Cossi, V. Barone, R. Cammi, J. Tomasi, *Chem. Phys. Lett.* **1996**, *255*, 327.
- [49] A. Klamt, *J. Phys. Chem.* **1995**, *99*, 2224.
- [50] M. F. Mesleh, J. M. Hunter, A. A. Shvartsburg, G. C. Schatz, M. F. Jarrold, *J. Phys. Chem.* **1996**, *100*, 16082.
- [51] G. von Helden, M. T. Hsu, N. Gotts, M. T. Bowers, *J. Phys. Chem.* **1993**, *97*, 8182.
- [52] A. A. Shvartsburg, M. F. Jarrold, *Chem. Phys. Lett.* **1996**, *261*, 86.

UNIVERSITAT ROVIRA I VIRGILI
THEORETICAL STUDIES ON TRANSITION METAL CATALYZED CARBON DIOXIDE FIXATION
Fernando Simón Castro Gómez

Chapter 3

Structural Studies of Metal-containing Inorganic Compounds by Ion Mobility Mass Spectrometry

A set of three salen ligands, together with their complexes with Cu and Zn, as well as Pd-containing intermediates within the catalytic Stille reaction, have been investigated using ion mobility mass spectrometry (IM-MS). Collision cross sections (CCS) for all the studied systems were obtained theoretically via the projection approximation (PA), the exact hard-spheres scattering (EHSS), and the trajectory method (TM) from either X-ray or DFT-optimized structures. Some parameters involving trajectories calculation were evaluated in order to gain insights into the accuracy of the methods. Excellent correlation between theoretical CCS and IM-MS experiments was reached for all the systems.



Parts of this chapter are published and another has been submitted: V. E. Wright, F. Castro-Gómez, E. Jurneczko, J. C. Reynolds, A. Poulton, S. D. R. Christie, P. Barran, C. Bo and C. Creaser, *Int. J. Ion Mobil. Spec.* **2013**, *16*, 61-67; V. E. Wright, F. Castro-Gómez, E. Jurneczko, J. C. Reynolds, A. Poulton, P. Barran, S. D. R. Christie, C. Bo and C. Creaser, *submitted*.

UNIVERSITAT ROVIRA I VIRGILI
THEORETICAL STUDIES ON TRANSITION METAL CATALYZED CARBON DIOXIDE FIXATION
Fernando Simón Castro Gómez

3.1 Introduction

Ion mobility spectrometry (IMS) is an electrophoretic-like technique that allows ionized molecules to be separated by measuring the time (drift time) taken for an ion to traverse a drift tube under the influence of an electric field in the presence of a buffer gas (usually helium or nitrogen).^[1] The mobility of an ion in the gas phase is determined by the collision cross section (CCS), which is a function of the size and shape of the ionized molecule and may be correlated directly with its molecular structure.^[2] IMS has found wide application in the detection of illegal or dangerous substances, most noticeably for chemical warfare agents and for explosives and narcotics at border crossings and airports.^[3] Combined with mass spectrometry (IM-MS), the technique offers separation on the basis of the CCS and mass-to-charge (m/z) ratio, i.e., the coupling of the two strategies allows a two-dimensional separation based on size and mass.^[4] The basic principles of IM-MS are described in Section 1.3 of Chapter 1.

Among the IMS techniques employed in IM-MS, three are widely used nowadays: drift-time ion mobility spectrometry (DTIMS),^[1a] travelling-wave ion mobility spectrometry (TWIMS)^[5] and field-asymmetric ion mobility spectrometry (FAIMS).^[6] Experimental results reported in this thesis have been carried out in collaboration with a research group at Loughborough University in UK (Victoria Wright, Dr. Colin Creaser, and Dr. Steve Christie), using DTIMS and TWIMS.

In a TWIMS drift tube the relationship between drift time and mobility is nonlinear and therefore standards with known CCS, that have been previously determined using a linear DTIMS drift cell, are needed to calibrate the system. A graph is plotted of known CCS modified to account for reduced mass and charge, against effective drift time and from this the CCS of the analytes can be determined. Calibrants have included peptides,^[7] tetraalkylammonium halides (TAAHs), and pharmaceutical compounds^[8] with structures that are usually different to that of the analyte ion under investigation. There are several reports on the application of this method to the study of metabolites,^[8,9] proteins and peptides.^[10]

The study of metal-containing ions by IM-MS including both DTIMS and TWIMS is a well-documented area. The CCS of biological molecules binding small metals such as the alkali metals^[11] as well as transition metals,^[12] have been widely studied. The CCS of

cationized polystyrene with Li^+ , Na^+ , Cu^+ and Ag^+ were also reported.^[13] In contrast, little work has been carried out on small nonbiological metal-ligand complexes containing transition metals. Ruthenium anticancer complexes have been studied and their CCS determined using TWIMS-MS.^[7a,b] In this chapter we report the structural analysis of salen ligands and their complexes of copper and zinc using IM-MS. Metal derived salen (metallo-salen) complexes are versatile compounds.^[14] that have proven to be effective catalysts for many chemical conversions including asymmetric epoxidations,^[15] epoxide^[16] and oxetanes^[17] ring-opening reactions and stereo-selective polymerizations.^[18] Indeed, one of the main goals on this thesis is the study of such reactions mediated by metallo-salen complexes and other metal-containing inorganic compounds.

IM-MS also plays a vital role on mechanistic studies, wherein catalytic intermediates are important in reaction understanding, design and process control.^[19] Electrospray ionization mass spectrometry (ESI-MS) has been widely used in reaction monitoring, due to its ability to detect a range of ionized and neutral species in solution, and to provide information on reaction kinetics.^[20] ESI is a soft ionization technique which provides information on the composition of reaction solutions in which solution phase structure is conserved in the gas phase.^[19,21] The combination of ESI with ion mobility spectrometry (IMS) and mass spectrometry (ESI-IM-MS) has recently shown to have the potential to significantly enhance selectivity and data quality in reaction monitoring.^[22] The Stille cross-coupling reaction is one of the most general and selective Palladium-catalyzed processes that has been studied using ESI-MS.^[23] In such systems, Pd-containing species have been reported as by-products or in equilibrium with other species in the catalytic cycle.

Experimentally-derived CCS may be compared with CCS calculated from structures obtained *via* DFT calculations or from X-ray structures, using a mobility calculator such as MOBCAL.^[24] The open source program MOBCAL is used to theoretically determine the CCS based on three algorithms: the projection approximation (PA),^[25] the exact hard-spheres scattering (EHSS),^[26] and the trajectory method (TM).^[27] Each of these methods depends on the ion's interaction with the IM buffer gas, and their basic principles are briefly described in Section 2.8 of Chapter 2.

Herein CCS derived from DTIMS and TWIMS experiments for salen ligands and their corresponding complexes are compared to theoretical CCS obtained from X-ray and DFT

structures. It is also reported the study of the Stille reaction by ESI-IM-MS, using free and tagged iodobenzene as the reactant, and shown the first observation of a Pd-containing catalytic intermediate within the catalytic cycle. We demonstrate that the incorporation of IMS analysis into mass spectrometric reaction monitoring provides a powerful new approach for simultaneous structural studies of low level catalytic reaction intermediates.

3.2 Motivation

Ion mobility mass spectrometry (IM-MS) in conjunction with molecular modeling and electronic structure calculations has become a powerful tool used to explore the three-dimensional shape of polyatomic ions. This is possible since CCSs generated theoretically can be compared with the experimentally determined CCSs to identify the conformations present in the IM-MS experiments.

In addition to the ability of providing information about ion conformations, IM-MS has shown great potential use in reaction monitoring, as alternative method to current infrared spectroscopy (IR), near infrared spectroscopy (NIR), nuclear magnetic resonance (NMR), and liquid chromatography (LC). Each of these techniques comes with limitations for the simultaneous monitoring of trace levels of catalytic intermediates in complex reaction mixtures. IM-MS would afford rapid information about the reaction that would not be possible with either instrument alone.

Considering the aforementioned advantages of IM-MS, and due the fact that only few studies have been carried out on inorganic transition metal complexes, we found of great interest to study structural features of salen ligand complexes of copper and zinc using IM-MS. Metallosalen complexes are versatile and they have proven to be very attractive compounds for a range of catalytic applications.

We also found fascinating the idea of using IM-MS in real-time Stille reaction monitoring in order to “catch catalytic intermediates on-the-fly”. In close collaboration with the group at Loughborough University in UK we focused on the study of reaction mechanisms by combining synthetic chemistry with IM-MS and DFT calculations. Comparison of theoretical outcome with IM-MS experiments could allow exploring a novel approach to the structural analysis of reaction intermediates and thus helping to the elucidation of reaction mechanisms.

3.3 Objectives

The aim of this chapter is to provide structural information and identification of metal-containing inorganic compounds by means of IM-MS. Our main objective is exploring the correlation between experimental measured CCSs and theoretical calculated CCSs.

Initially we focus our study on the evaluation of three salen ligands and their complexes with copper and zinc. We will generate optimized structures and atomic charges for all the complexes through DFT calculations. Then we will compute the CCSs using the MOBCAL program. In this stage, the accuracy of algorithms used for computing mobilities will be determined by evaluating some parameters of the program.

Additionally we will study Pd-containing catalytic intermediates of the Stille reaction and demonstrate proof of principle that IM-MS can afford simultaneous structural information on intermediates present in a reaction mixture. Herein we will calculate CCS for different isomers of key intermediates in the proposed Stille catalytic cycle.

3.4 Computational details

All structures in this study have been determined using DFT with the Gaussian 09 package.^[28] For salen ligands and metallosalen complexes, the B3LYP^[29] functional was used, together with the standard 6-31G(d,p) basis set to describe the H, C, N and O atoms. Besides B3LYP, the B97D^[30] functional was also used for the intermediates of the Stille reaction. In this case, the standard 6-311G(d,p) basis set was employed to describe the H, C, N and P atoms. The relativistic effective core pseudo potential LANL2DZ^[31] was used, in conjunction with its associated basis set for Zn, Cu, Pd, P and I atoms, depending on the system studied. Full geometry optimizations were performed without constraints. The nature of the stationary points encountered was characterized by harmonic vibrational frequencies analysis.

The open source program MOBCAL^[24] was used to calculate the CCSs *via* the projection approximation (PA), the exact hard-spheres scattering (EHSS), and the trajectory method (TM). Molecular structures were taken either from X-ray crystallographic data (for neutral salen ligands and metallosalen complexes) or DFT-optimized structures (for protonated salen ligands, metallosalen complexes and intermediates of the Stille reaction). Helium parameters were assumed when carrying out MOBCAL calculations. For H, C, N, and O

atoms, the default Lennard-Jones (12-6) parameters^[26] were considered as well as recently developed sets from Siu and coworkers^[32] and from Campuzano and coworkers.^[8] Since the He interactions with Cu, Zn, Pd, P and I are not defined within the original MOBCAL code, we incorporated them by using the Lennard-Jones parameters for the silicon-He interaction ($\epsilon=1.35$ meV, $\rho=3.5$ Å). Two important parameters involving the number of TM and EHSS trajectories (inum and imp, respectively) used for calculating CCS were initially modified in order to evaluate the accuracy of both methods and its influence on computing times. For all the atoms charge-induced dipole interactions were included from Mulliken atomic charges computed at the DFT level.

The MOBCAL code was compiled and optimized using the PGI Portland Group Compiler and some Shell scripts were built for submitting several jobs.

3.5 Results

3.5.1 Salen ligands and metallosalen complexes

The focus of the first part of the present study is on protonated compounds for neutral species of the Schiff base ligands (L1-L3) and their corresponding metal complexes (L1M-L3M) with Cu(II) and Zn(II), shown in Figure 3.1.

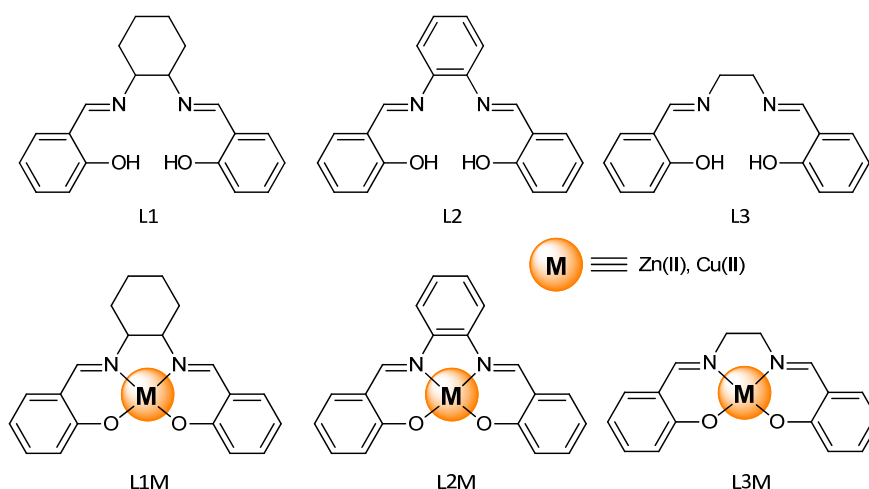


Figure 3.1 Neutral species of the salen ligands (above) and metallosalen complexes (below).

Since these compounds form singly charged ions of the type $(L + H)^+$ or $(LM + H)^+$ in the IM-MS experiments, we first determined the most stable protonation sites for each set of molecules. In case of the ligands, the additional proton could be placed on either the N or the O atoms depicted in Figure 3.2. The formation of a metal hydride was also considered for the metal complexes in addition to the N and O sites.

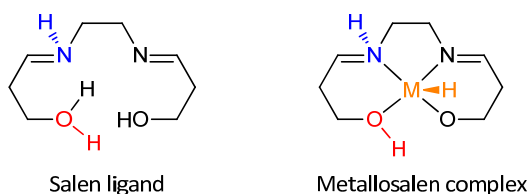


Figure 3.2 Possible protonated sites for salen ligands and metallosalen complexes.

Table 3.1 collects the relative energies calculated at the B3LYP/6-31G(d,p) level for the protonated molecules described above. As expected for metallosalen complexes, the most stable structures were by far those protonated on the most basic oxygen site. The formation of a metal hydride resulted in very unstable structures in all the cases. Protonation of nitrogen on salen ligands was shown to be favored; that is due to the unsaturated nitrogen atoms in the imines are known for being good proton acceptors.

Table 3.1 Relative energies (in kcal·mol⁻¹) for salen ligands and metallosalen complexes.

Compound	Protonation sites		
	M-H	N-H	O-H
Ligand 1	-	0.0	10.2
Ligand 2	-	0.0	unstable
Ligand 3	-	0.0	10.3
L1Cu	77.9	20.2	0.0
L2Cu	79.4	24.9	0.0
L3Cu	74.4	15.4	0.0
L1Zn	unstable	7.8	0.0
L2Zn	70.0	10.5	0.0
L3Zn	unstable	5.6	0.0

Once identified the most stable protonated structures for both sets of compounds, their CCSs are determined using the MOBCAL program.

First, we probed the accuracy of the methods employed for obtaining CCSs by evaluating some relevant parameters involved in the calculation of the TM and EHSS trajectories. It is worth noting that the methods used to calculate mobilities are based on classical Monte Carlo simulations. In order to consider a greater number of trajectories, the parameter (**imp**) that defines the number of points in Monte Carlo integrations of impact parameter and orientation in TM, was varied from its default value of 25 to 1250 as well as 2500. Similarly, the number of Monte Carlo trajectories employed by the EHSS method, which is defined by **inum**, was incremented by factors of 10 and 20 times from the default value of 250000. The L1Zn and L2Cu protonated systems were selected in order to evaluate both parameters, as summarized in Table 3.2.

Table 3.2 Collision cross sections (in Å²) calculated for the L1Zn and L2Cu protonated systems using the default and adjusted **Inum** and **Imp** trajectory parameters.

Parameters	L1Zn Protonated			L2Cu Protonated			
	PA	EHSS	TM	PA	EHSS	TM	
Default ^a	122.13	129.21	119.44 ± 5.5	118.19	123.08	114.95 ± 5.9	
imp	1250	122.18	129.05	121.62 ± 4.0	118.26	123.16	115.91 ± 4.0
	2500	122.19	129.06	121.26 ± 3.8	118.28	123.16	116.94 ± 4.3
inum	2500000	122.13	129.21	119.27 ± 1.1	118.19	123.08	114.65 ± 1.1
	5000000	122.13	129.21	118.92 ± 0.4	118.19	123.08	114.37 ± 0.4

^a **imp**=25; **inum**=250000

In general, minor changes can be observed in the CCSs calculated with the modified parameters compared to those obtained with the default ones. However, since much more trajectories were examined during determination of mobilities, a considerable improvement in the accuracy of TM was achieved. In addition, computation times consistently increases between 10–20 minutes. Due to these results and the fact that the standard deviation associated to the computed values using the default parameters falls in the same order of magnitude as the uncertainty of the experimental measurements (~5 Å²), the default values for **imp** and **inum** were used for calculating CCSs for the remaining systems.

The X-ray structures of the ligands and their metal complexes were obtained from the Cambridge Structural Database (CSD), and input into MOBCAL in order to obtain theoretical CCSs. Mulliken charges were included from single point calculations on the

X-ray coordinates. Table 3.3 collects both experimental and theoretical results for this step. There was generally good agreement between the PA and TM approximations. However, the EHSS method overestimates the CCS, which is consistent with previously reported data.^[7a,b] Experimental CCSs determined by TWIMS using the peptide standards show better correlation with both the PA and TM derived from the X-ray data, than with the data calibrated using the TAAH, with the exception of the free ligands L2 and L3. It should be noted that the CCS values derived from the X-ray data decrease in the order $L2 \geq L1 > L3$, which differs from the order observed experimentally ($L1 > L2 > L3$). This may be due to protonation in the gas-phase restricting out of plane rotation of the phenol rings, which does not occur in the solid state. The DTIMS experimental data is poorly correlated with both the PA and TM derived CCS from the X-ray structures, showing consistently smaller CCS radius. These observations suggest that CCSs derived from X-ray coordinates should be used with caution in structural studies of small ligands and metal-ligand complexes measured by IM-MS.

Table 3.3 Experimental CCS from DTIMS and TWIMS and theoretical CCS (in Å²) calculated from X-ray and DFT-optimized structures for salen ligands and metallosalen complexes.

Compound	Experimental CCS ^a			X-ray CCS			DFT CCS		
	TWIMS (TAAHs)	TWIMS (Peptides)	DTIMS	PA	EHSS	TM	PA	EHSS	TM
Ligand 1	120	113	109	115	123	116	120	128	117
Ligand 2	113	108	105	117	124	116	117	123	115
Ligand 3	103	97	94	110	115	106	106	112	105
L1Cu	122	115	109	116	122	114	121	128	118
L2Cu	116	110	104	113	117	110	118	123	115
L3Cu	103	98	94	105	108	101	107	112	105
L1Zn	123	117	110	118	124	118	122	129	119
L2Zn	119	112	106	113	117	114	119	124	115
L3Zn	105	100	97	103	107	101	108	113	106

^a DTIMS data measured in helium, TWIMS data measured in nitrogen and extrapolated to helium.

As already shown in Table 3.3, CCSs from the DFT-optimized structures show reasonable agreement with those derived from the X-ray data. Both DFT and X-ray results

correlate better with the experimental data using the TAAH standards than the peptide standards and DTIMS data. This suggests that MOBCAL overestimates the CCS for these small ions.

At this point of the study, two new sets of Lennard-Jones (12-6) parameters were introduced by Siu and coworkers^[32] and also by Campuzano and coworkers,^[8] thus, we decided to use them in our investigation. Theoretical CCSs calculated using the new LJ-parameters (ϵ and ρ) are shown in Table 3.4. There is good agreement between the PA and TM approximations for both sets of data. The TM and PA CCS data obtained using the Siu LJ-parameters on the X-ray structures are within 5 Å² of the DTIMS experimental data, which is at the upper end of the range for measurement uncertainty. The Campuzano TM optimized data set indicates a slight overestimation of the CCS with the calculated CCS displaying increased correlation with the peptide standard data.

Table 3.4 Theoretical CCS calculated from X-ray and DFT-optimized structures using MOBCAL with the LJ-parameters sets by Siu and Campuzano.

Compound	X-ray CCS				DFT CCS			
	Siu		Campu- zano		Siu		Campu- zano	
	PA	EHSS	TM	TM	PA	EHSS	TM	TM
Ligand 1	104	112	107	110	110	113	109	114
Ligand 2	107	112	107	112	107	111	106	113
Ligand 3	99	100	97	102	97	99	97	102
L1Cu	107	112	104	111	112	114	110	116
L2Cu	104	110	101	108	109	112	106	113
L3Cu	96	98	92	99	99	100	97	103
L1Zn	109	113	108	114	113	114	111	116
L2Zn	104	110	107	112	110	113	106	113
L3Zn	95	99	92	99	100	100	98	103

Figure 3.3 shows a comparison of the experimental data (shown in Table 3.3) and the X-ray and DFT-based data using the Siu parameters (collected in Table 3.4), for the L1Cu complex. A comparison of the experimental CCS data against the DFT-based CCS data calculated using the new LJ-parameters displays excellent agreement between the DTIMS and the PA and TM data using the Siu parameters within on average ~ 3 Å². This illustrates

the need for refinement of the methods used to calculate CCS and highlights the sensitivity of this approach. The peptide data also correlates well with the Siu PA parameter data allowing for the slight (3%) overestimate for the TWIMS data using the peptide standards. There is poorer correlation between the DTIMS and TWIMS experimental measurements and the TM results using the Campuzano parameters. The presented data demonstrates that the PA and TM calculations with the optimized parameters for the DFT-based structures show better correlation with the experimental data for the ligands and complexes studied and that TWIMS CCS measurements using peptide standards may be correlated with calculated data for structural studies of low molecular weight metal complexes.

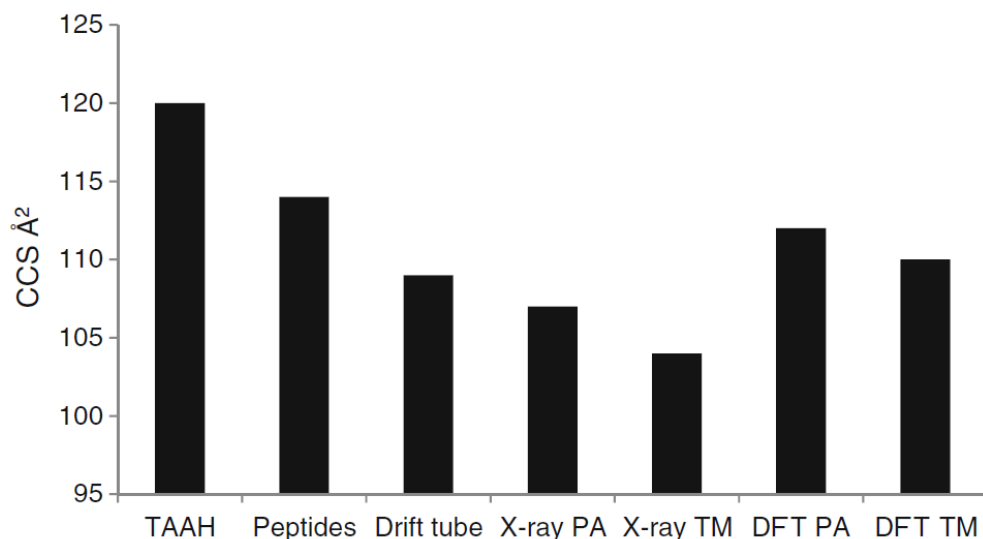
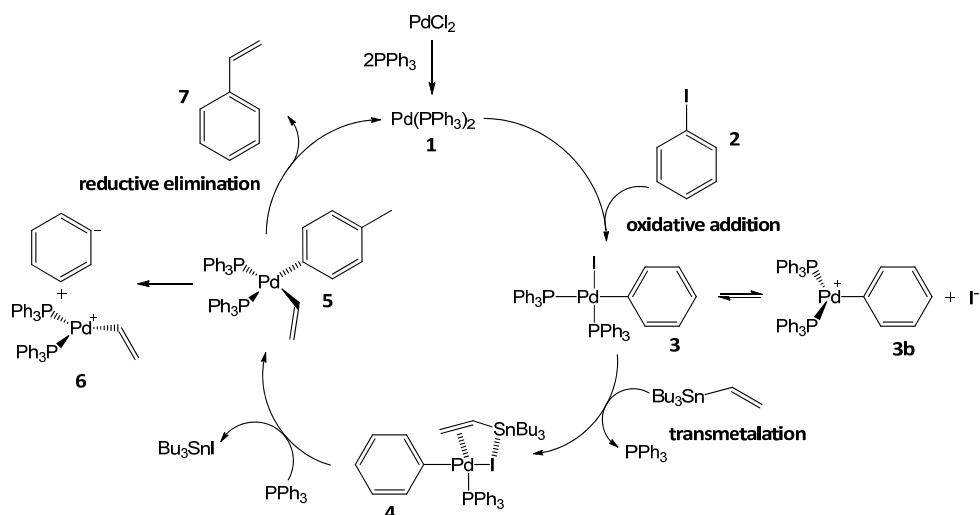


Figure 3.3 Comparison between the experimental data from DTIMS and TWIMS and the theoretical data from X-ray and DFT-optimized structures using the Siu parameters for L1Cu.

3.5.2 Catalytic intermediates of the Stille reaction

The Stille cross-coupling reaction is one of the most general, selective, and versatile palladium-catalyzed reactions used to generate carbon-carbon bonds.^[23a,b] This reaction involves the Pd-catalyzed coupling of organic electrophiles such as unsaturated halides, sulfonates, or triflates with functionalized organostannanes. The well-known mechanism for the Stille reaction is based on three main steps, oxidative addition, transmetalation,

and reductive elimination (Scheme 3.1), besides a *cis-to-trans* isomerization preceding the transmetalation step in the case of organic halides as electrophiles.^[23c] Although it is nowadays one of the most extensively used catalytic systems in organic synthesis, Pd-containing intermediates implicated in the reaction have been isolated and characterized only outside the real catalytic cycle. Herein we focus in the detection and characterization of catalytic intermediates of the Stille reaction by IM-MS. Many of these intermediates are neutral species with low proton affinities and, therefore, are not suitable for ESI-IM-MS detection. For that reason charge bearing groups need to be attached to those species to allow them to be detected by ESI-MS.^[20d,e] Hence, iodobenzene was tagged with 1-methylimidazole by reaction with 1,4-iodobenzylbromide to give **2_{tag}** (Figure 3.4), resulting in a permanent charge, which was incorporated into subsequent intermediates and products. Also, the intermediate **3_{tag}** shown in Figure 3.4 was generated by reaction of **2_{tag}** with the palladium catalyst and is the first reported palladium-containing intermediate within the proposed Stille catalytic cycle. The tag was incorporated in the *para* position to minimize the effect on the reaction.



Scheme 3.1 The Stille reaction catalytic cycle used in this study.

We selected the Pd-containing intermediate **3_{tag}** and the un-tagged intermediate **3b** (Scheme 3.1) for further study. Optimized structures of these species were obtained *via* DFT calculations with the hybrid B3LYP and the B97D functionals.

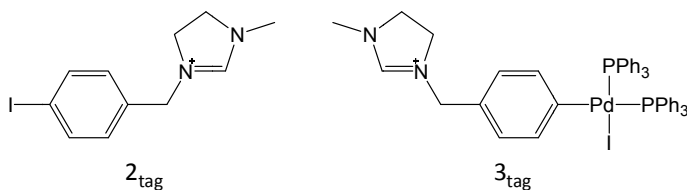


Figure 3.4 Methyl imidazole tagged intermediates of the Stille reaction.

The relative position of the phosphine groups with respect to the metal center defines isomers *cis* and *trans* for species **3b** (Figure 3.5). The optimized structures of both isomers present a T-shape conformation. According to their relative energies, the *trans* isomer is slightly more stable than the *cis* isomer. At the B97D level, the *trans* isomer is favored by only 1.0 kcal·mol⁻¹, whereas the energy difference increases to 6.0 kcal·mol⁻¹ at the B3LYP level.

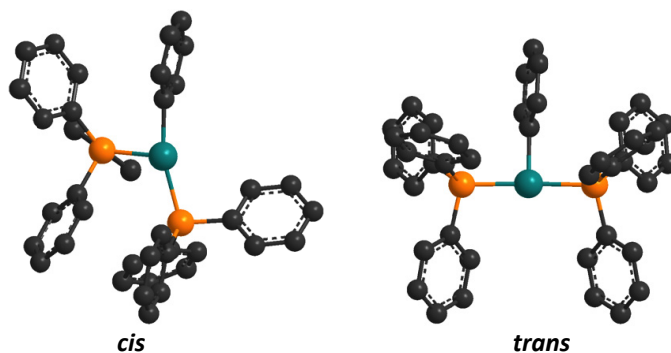


Figure 3.5 Optimized structures of intermediate **3b** isomers at B97D/6-311G(d,p) level. Hydrogen atoms omitted for clarity.

The two first entries of Table 3.4 and Table 3.5 show the comparison between the experimental and the theoretical CCS values calculated for the *cis* and *trans* isomers of species **3b** with the default set of Lennard-Jones (6-12) parameters and the LJ-parameters optimized by Siu and coworkers and by Campuzano and coworkers. Unlike for the default and Campuzano LJ-parameter sets, CCSs obtained using the Siu LJ-parameters show better agreement with the experiment. For this reason, further analysis on CCS was performed based only on the Siu set.

Table 3.4 Experimental CCS as well as theoretical CCS for intermediates **3b** and **3_{tag}** calculated with the default LJ-parameters in MOBCAL.^a

Exp. CCS	Intermediate	Theoretical CCS (SD = 0.7%)					
		B3LYP			B97D		
		PA	EHSS	TM	PA	EHSS	TM
3b 178 ± 2	trans	181	206	198	179	203	195
	cis	178	203	193	172	195	186
3_{tag} 204 ± 3	trans-1	206	235	213	203	232	221
	trans-2	205	235	225	200	229	207
	cis-1	204	234	210	200	227	217
	cis-2	203	232	225	199	227	205

^a The program was configured for calculating CCS with the default number of Monte Carlo trajectories: imp=1250; inum=2500000

Table 3.5 Theoretical CCS for intermediates **3b** and **3_{tag}** calculated with LJ-parameter sets by Siu and Campuzano using MOBCAL.^a

Intermediate		Theoretical CCS (SD = 0.7%)							
		B3LYP				B97D			
		Siu		Campuzano		Siu		Campuzano	
		PA	EHSS	TM	TM	PA	EHSS	TM	TM
3b	trans	169	185	183	190	167	183	182	189
	cis	166	181	180	187	161	174	174	181
3_{tag}	trans-1	194	212	210	218	191	209	207	214
	trans-2	194	212	211	218	189	206	205	211
	cis-1	193	210	208	216	188	204	203	210
	cis-2	192	209	207	214	188	203	202	208

^a The program was configured for calculating CCS with the default number of Monte Carlo trajectories: imp=1250; inum=2500000

In the case of intermediate **3b**, the TM method correlates well with the experimental measurements, followed closely by EHSS; whereas the PA consistently underestimates the CCS values. B97D values are systematically lower than those obtained with B3LYP because all metal-ligand bond lengths are slightly shorter. It is worth noting that small changes in the geometry of the metal complexes may significantly affect the calculated CCS, by as much as 4 Å², which is close to the uncertainty of the experimental measurement. Although the *trans* isomer is the most energetically stable structure, comparison of the

theoretical CCS values for *cis* and *trans* isomers indicates that it is not possible to distinguish between the two configurations based on the resulting CCS. The standard deviation in the computed values falls in the same order of magnitude as the uncertainty associated with the experimental measurements. Nonetheless, the difference in computed CCS values between the two isomers provides a larger value for the *trans* isomer than for the *cis* isomer.

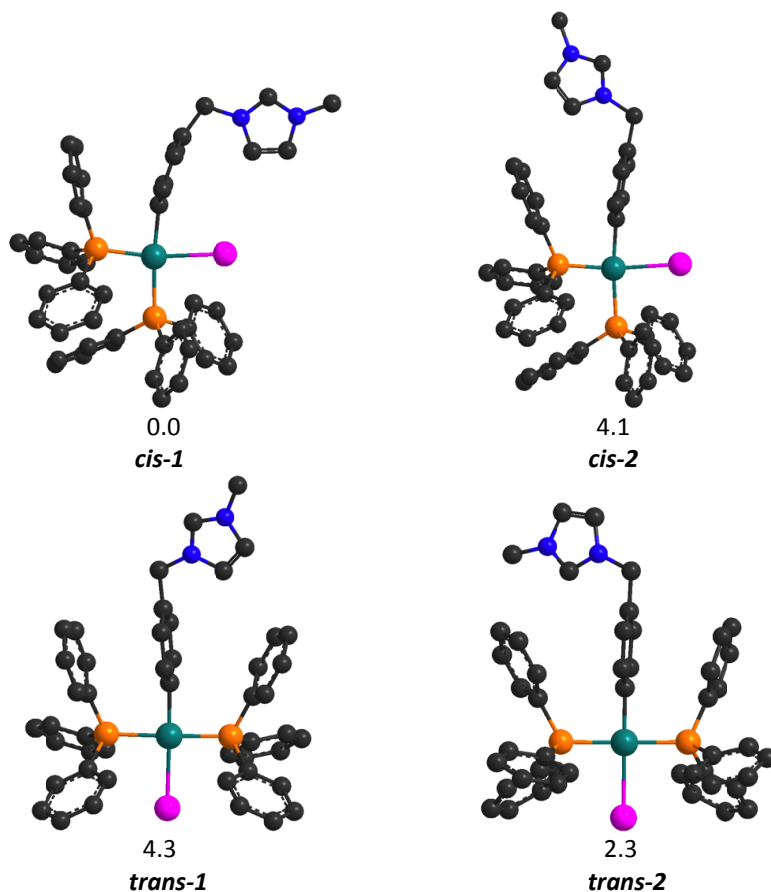


Figure 3.6 Optimized structures and relative energies ($\text{kcal}\cdot\text{mol}^{-1}$) of the different isomers of intermediate $\mathbf{3}_{\text{tag}}$ at B97D/6-311G(d,p) level. Hydrogen atoms omitted for clarity.

Species $\mathbf{3}_{\text{tag}}$ also presents *cis* and *trans* configurations, but taking into account the relative orientation of the 1-methylimidazole moiety, we considered the four structures depicted in Figure 3.6. DFT-optimized geometries correspond to square-planar complexes for all the isomers, with intermediate *cis-1* being the most stable structure according to

their relative energies. Collision cross sections obtained with both DFT methods show the PA to give systematically lower values than the EHSS and TM. The B3LYP method results in systematically larger CCS values than the BP97D method. However, the computed CCS values for the four isomers fall in a very narrow range, 4 \AA^2 on average, which is close to the uncertainty in the experimental data.

The DFT method used has a more pronounced effect on CCS than the integration method EHSS or TM. This is because, in these particular systems, B97D reproduces the π -stacking interactions between the phenyl rings in the structures better than B3LYP, thus small differences in the geometries are obtained. The agreement between the measured and computed TM values for the B97D method is excellent, although isomeric separation could not be achieved at the resolution of the TWIMS drift tube.

3.6 Conclusions

A detailed structural study for a set of three salen ligands, together with their complexes with Cu and Zn, and also Pd-containing intermediates of the catalytic Stille reaction was accomplished by ion mobility mass spectrometry (IM-MS).

No significant changes were observed on the absolute values of CCS obtained with the modified trajectories parameters for the selected protonated systems. However, a better accuracy for the Trajectory Method (TM) was achieved.

The accuracy of both the experimental setup and the computational methodology reached the same level and the agreement between the measured and computed values was excellent.

Even better agreement between experimental and theoretical CCS was obtained using the Siu and coworkers Lennard-Jones parameter sets for all the compounds under study.

We report the first observation of a catalytic intermediate within the Stille cycle and demonstrate proof of principle that IM-MS can provide simultaneous structural information on intermediates present in a reaction mixture, including low level catalytic species that cannot be studied by other techniques.

Due to the similarity of the size and shape of the different isomers, isomeric resolution could not be achieved for catalytic intermediates of the Stille reaction. However, where more bulky and sophisticated phosphine and phosphite ligands are commonly used, we envision new opportunities to improve the selectivity of this technique.

3.7 References and notes

- [1] a) C. S. Creaser, J. R. Griffiths, C. J. Bramwell, S. Noreen, C. A. Hill, C. L. P. Thomas, *Analyst* **2004**, *129*, 984; b) F. Lanucara, S. W. Holman, C. J. Gray, C. E. Eyers, *Nat. Chem.* **2014**, *6*, 281.
- [2] G. A. Eiceman, Z. Karpas, *Ion Mobility Spectrometry*, CRC Press: Boca Raton, 2nd Ed, **2004**.
- [3] P. A. D'Agostino, C. L. Chenier, *Rapid Commun. Mass Spectrom.* **2010**, *24*, 1617.
- [4] R. Mukhopadhyay, *Anal. Chem.* **2008**, *80*, 7918.
- [5] K. Giles, S. D. Pringle, K. R. Worthington, D. Little, J. L. Wildgoose, R. H. Bateman, *Rapid Commun. Mass Spectrom.* **2004**, *18*, 2401.
- [6] R. W. Purves, R. Guevremont, *Anal. Chem.* **1999**, *71*, 2346.
- [7] a) J. P. Williams, J. A. Lough, I. Campuzano, K. Richardson, P. J. Sadler, *Rapid Commun. Mass Spectrom.* **2009**, *23*, 3563; b) J. Williams, T. Bugarcic, A. Habtemariam, K. Giles, I. Campuzano, P. M. Rodger, P. Sadler, *J. Am. Soc. Mass Spectrom.* **2009**, *20*, 1119; c) T. W. Knapman, J. T. Berryman, I. Campuzano, S. A. Harris, A. E. Ashcroft, *Int. J. Mass Spectrom.* **2010**, *298*, 17.
- [8] I. Campuzano, M. F. Bush, C. V. Robinson, C. Beaumont, K. Richardson, H. Kim, H. I. Kim, *Anal. Chem.* **2011**, *84*, 1026.
- [9] F. Cuyckens, C. Wassvik, R. J. Mortishire-Smith, G. Tresadern, I. Campuzano, J. Claereboudt, *Rapid Commun. Mass Spectrom.* **2011**, *25*, 3497.
- [10] a) K. Thalassinou, M. Grabenauer, S. E. Slade, G. R. Hilton, M. T. Bowers, J. H. Scrivens, *Anal. Chem.* **2008**, *81*, 248; b) C. A. Scarff, K. Thalassinou, G. R. Hilton, J. H. Scrivens, *Rapid Commun. Mass Spectrom.* **2008**, *22*, 3297; c) I. Michaelevski, M. Eisenstein, M. Sharon, *Anal. Chem.* **2010**, *82*, 9484; d) C. Atmanene, S. Petiot-Bécard, D. Zeyer, A. Van Dorsselaer, V. Vivat Hannah, S. Sanglier-Cianférani, *Anal. Chem.* **2012**, *84*, 4703; e) R. Salbo, M. F. Bush, H. Naver, I. Campuzano, C. V. Robinson, I. Pettersson, T. J. D. Jørgensen, K. F. Haselmann, *Rapid Commun. Mass Spectrom.* **2012**, *26*, 1181.
- [11] a) T. Wyttenbach, J. J. Batka Jr, J. Gidden, M. T. Bowers, *Int. J. Mass Spectrom.* **1999**, *193*, 143; b) T. Wyttenbach, M. Witt, M. T. Bowers, *J. Am. Chem. Soc.* **2000**,

- 122, 3458; c) B. H. Clowers, H. H. Hill, *J. Mass Spectrom.* **2006**, *41*, 339; d) R. M. Moision, P. B. Armentrout, *J. Phys. Chem. A* **2006**, *110*, 3933.
- [12] a) J. A. Taraszka, J. Li, D. E. Clemmer, *J. Phys. Chem. B* **2000**, *104*, 4545; b) M. Leavell, S. Gaucher, J. Leary, J. Taraszka, D. Clemmer, *J. Am. Soc. Mass Spectrom.* **2002**, *13*, 284; c) E. S. Baker, M. J. Manard, J. Gidden, M. T. Bowers, *J. Phys. Chem. B* **2005**, *109*, 4808; d) T. Wyttenbach, D. Liu, M. T. Bowers, *J. Am. Chem. Soc.* **2008**, *130*, 5993; e) Y. Berezovskaya, C. T. Armstrong, A. L. Boyle, M. Porrini, D. N. Woolfson, P. E. Barran, *Chem. Commun.* **2011**, *47*, 412; f) O. Chepelin, J. Ujma, P. E. Barran, P. J. Lusby, *Angew. Chem. Int. Ed.* **2012**, *51*, 4194.
- [13] J. Gidden, M. Bowers, A. Jackson, J. Scrivens, *J. Am. Soc. Mass Spectrom.* **2002**, *13*, 499.
- [14] P. G. Cozzi, *Chem. Soc. Rev.* **2004**, *33*, 410; b) C. J. Whiteoak, G. Salassa, A. W. Kleij, *Chem. Soc. Rev.* **2012**, *41*, 622.
- [15] a) Y. Sawada, K. Matsumoto, T. Katsuki, *Angew. Chem. Int. Ed.* **2007**, *46*, 4559; b) A. M. Castilla, S. Curreli, E. C. Escudero-Adán, M. M. Belmonte, J. Benet-Buchholz, A. W. Kleij, *Org. Lett.* **2009**, *11*, 5218.
- [16] a) J. M. Ready, E. N. Jacobsen, *Angew. Chem.* **2002**, *114*, 1432; b) J. M. Ready, E. N. Jacobsen, *Angew. Chem. Int. Ed.* **2002**, *41*, 1374.
- [17] R. N. Loy, E. N. Jacobsen, *J. Am. Chem. Soc.* **2009**, *131*, 2786.
- [18] a) W. Hirahata, R. M. Thomas, E. B. Lobkovsky, G. W. Coates, *J. Am. Chem. Soc.* **2008**, *130*, 17658; b) X.-B. Lu, D. J. Darensbourg, *Chem. Soc. Rev.* **2012**, *41*, 1462; c) D. J. Darensbourg, A. D. Yeung, *Polym. Chem.* **2014**.
- [19] *Reactive Intermediates: MS Investigations in Solution* (Ed.: L. S. Santos), Wiley, Weinham, **2010**.
- [20] a) A. O. Aliprantis, J. W. Canary, *J. Am. Chem. Soc.* **1994**, *116*, 6985; b) C. Hinderling, C. Adlhart, P. Chen, *Angew. Chem.* **1998**, *110*, 2831; c) C. Hinderling, C. Adlhart, P. Chen, *Angew. Chem. Int. Ed.* **1998**, *37*, 2685; d) C. Adlhart, P. Chen, *Helv. Chim. Acta* **2000**, *83*, 2192; e) K. L. Vikse, Z. Ahmadi, C. C. Manning, D. A. Harrington, J. S. McIndoe, *Angew. Chem. Int. Ed.* **2011**, *50*, 8304; f) K. L. Vikse, Z. Ahmadi, C. C. Manning, D. A. Harrington, J. S. McIndoe, *Angew. Chem.* **2011**, *123*, 8454.

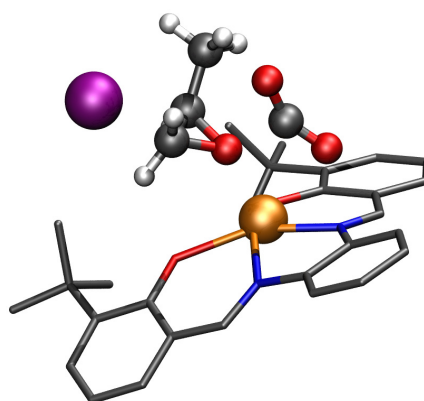
- [21] a) L. S. Santos, C. H. Pavam, W. P. Almeida, F. Coelho, M. N. Eberlin, *Angew. Chem.* **2004**, *116*, 4430; b) L. S. Santos, C. H. Pavam, W. P. Almeida, F. Coelho, M. N. Eberlin, *Angew. Chem. Int. Ed.* **2004**, *43*, 4330.
- [22] a) E. L. Harry, A. W. T. Bristow, I. D. Wilson, C. S. Creaser, *Analyst* **2011**, *136*, 1728; b) K. M. Roscioli, X. Zhang, S. X. Li, G. H. Goetz, G. Cheng, Z. Zhang, W. F. Siems, H. H. Hill, *Int. J. Mass Spectrom.* **2013**, *336*, 27.
- [23] a) P. Espinet, A. M. Echavarren, *Angew. Chem.* **2004**, *116*, 4808; b) P. Espinet, A. M. Echavarren, *Angew. Chem. Int. Ed.* **2004**, *43*, 4704; c) A. Nova, G. Ujaque, F. Maseras, A. Lledós, P. Espinet, *J. Am. Chem. Soc.* **2006**, *128*, 14571; d) L. S. Santos, G. B. Rosso, R. A. Pilli, M. N. Eberlin, *J. Org. Chem.* **2007**, *72*, 5809.
- [24] M. F. Jarrold, *Mobcal*, website at <http://www.indiana.edu/~nano/software.html>.
- [25] G. von Helden, M. T. Hsu, N. Gotts, M. T. Bowers, *J. Phys. Chem.* **1993**, *97*, 8182.
- [26] A. A. Shvartsburg, M. F. Jarrold, *Chem. Phys. Lett.* **1996**, *261*, 86.
- [27] M. F. Mesleh, J. M. Hunter, A. A. Shvartsburg, G. C. Schatz, M. F. Jarrold, *J. Phys. Chem.* **1996**, *100*, 16082.
- [28] Gaussian, Revision A.02, M. J. Frisch, G. W. Trucks, H. B. Schlegel, G. E. Scuseria, M. A. Robb, J. R. Cheeseman, G. Scalmani, V. Barone, B. Mennucci, G. A. Petersson, H. Nakatsuji, M. Caricato, X. Li, H. P. Hratchian, A. F. Izmaylov, J. Bloino, G. Zheng, J. L. Sonnenberg, M. Hada, M. Ehara, K. Toyota, R. Fukuda, J. Hasegawa, M. Ishida, T. Nakajima, Y. Honda, O. Kitao, H. Nakai, T. Vreven, J. A. Montgomery, Jr., J. E. Peralta, F. Ogliaro, M. Bearpark, J. J. Heyd, E. Brothers, K. N. Kudin, V. N. Staroverov, R. Kobayashi, J. Normand, K. Raghavachari, A. Rendell, J. C. Burant, S. S. Iyengar, J. Tomasi, M. Cossi, N. Rega, N. J. Millam, M. Klene, J. E. Knox, J. B. Cross, V. Bakken, C. Adamo, J. Jaramillo, R. Gomperts, R. E. Stratmann, O. Yazyev, A. J. Austin, R. Cammi, C. Pomelli, J. W. Ochterski, R. L. Martin, K. Morokuma, V. G. Zakrzewski, G. A. Voth, P. Salvador, J. J. Dannenberg, S. Dapprich, A. D. Daniels, Ö. Farkas, J. B. Foresman, J. V. Ortiz, J. Cioslowski, D. J. Fox, **2009**, Gaussian, Inc., Wallingford CT.
- [29] a) A. D. Becke, *Phys. Rev. A* **1988**, *38*, 3098; b) A. D. Becke, *J. Chem. Phys.* **1993**, *98*, 5648.
- [30] S. Grimme, *J. Comput. Chem.* **2006**, *27*, 1787.

- [31] P. J. Hay, W. R. Wadt, *J. Chem. Phys.* **1985**, *82*, 270.
- [32] C. K. Siu, Y. Z. Guo, I. S. Saminathan, A. C. Hopkinson, K. W. M. Siu, *J. Phys. Chem. B* **2010**, *114*, 1204.

Chapter 4

Catalytic Formation of Cyclic Carbonates from CO₂ and Epoxides by Zn(salphen) Complexes

The reaction mechanism for the Zn(salphen)/NBu₄X (X = Br, I) mediated addition of CO₂ to a series of epoxides, affording cyclic carbonate products has been investigated in detail using DFT. The ring-opening step of the process was examined and the preference for opening at the methylene (C_β) or methine carbon (C_α) was established. Furthermore, calculations were performed to clarify the reasons for the lethargic behavior of internal epoxides in the presence of the binary catalyst. Also the CO₂ insertion and the ring-closing steps have been explored for six differently substituted epoxides and these proved to be significantly more challenging compared with the ring-opening step. The reaction profile obtained for the N₂O₂-donor Zn(salphen) complex was compared with the relative barriers calculated using a Zn(salen) catalyst containing N₄-donor Schiff base ligands.

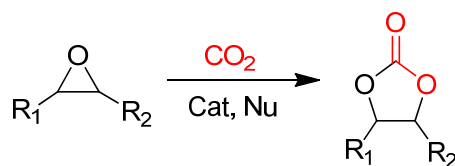


The work described in this chapter has been published: F. Castro-Gómez, G. Salassa, A. W. Kleij, C. Bo, *Chem. Eur. J.* **2013**, *19*, 6289. Results of the last part of the chapter, involving the Zn-N₄(salen), are unpublished: F. Castro-Gómez, Lorraine Christ, C. Bo, *in preparation*.

UNIVERSITAT ROVIRA I VIRGILI
THEORETICAL STUDIES ON TRANSITION METAL CATALYZED CARBON DIOXIDE FIXATION
Fernando Simón Castro Gómez

4.1 Introduction

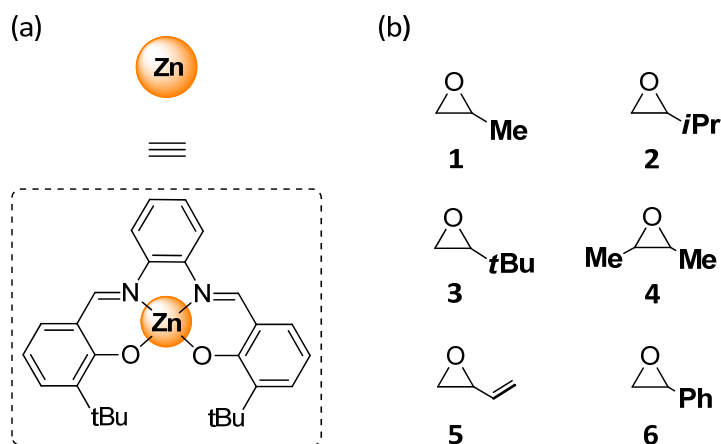
The growing concerns about climate change and the need to find suitable alternatives for our depleting fossil fuel based feedstocks have resulted in extensive research to find new renewable carbon sources. Carbon dioxide (CO₂) may indeed be considered an abundant and renewable carbon source. In light of this, it has become a popular building block from a sustainability point of view^[1] and can thus be seen as an interesting starting point for the synthesis of various organic molecules.^[2] One reaction that utilizes CO₂ as a carbon source and which is currently attracting a great deal of interest is the atom-efficient addition of CO₂ to epoxides, resulting in useful cyclic carbonate products (Scheme 4.1).^[3] The conventional industrial way of organic carbonate formation uses phosgene as a (toxic) reagent and results in hazardous waste streams.^[4] Therefore, new and greener methodologies able to mediate this transformation have become increasingly interesting. Cyclic carbonates are employed as polar aprotic solvents and electrolytes in rechargeable batteries, intermediates for organic polycarbonate synthesis, and in the production of pharmaceuticals and fine chemicals.^[1,5]



Scheme 4.1 The addition reaction of CO₂ with epoxides generating five-membered cyclic carbonates using a Lewis acidic metal catalyst (Cat) and a co-catalyst (Nu; nucleophile).

The addition reaction of CO₂ with epoxides has been widely studied and can be catalyzed by a variety of catalyst types such as quaternary ammonium salts,^[6] alkali metal halides,^[7] ionic liquids,^[8] functional polymers^[9] and transition metal complexes.^[10] However, there are still disadvantages to overcome upon using these catalyst systems such as low catalyst reactivity/stability, use of high pressures and/or temperatures, high catalyst loadings required for efficient turnover, toxicity issues, cost effectiveness and availability of the catalyst system, or a combination of these features. Hence, it is crucial to know how the performance of any given catalyst can be improved, and mechanistic understanding provides a means to unravel the obstacles associated with the observation of low reactivity and/or selectivity.

To date, a limited series of theoretical studies on the mechanism for the catalytic addition of CO₂ to epoxides have been reported involving either heterobimetallic Ru-Mn complexes,^[11] ionic liquids,^[12] N-heterocyclic carbenes,^[13] polyoxometalates,^[14] polyphenolic compounds^[15] or carboxylate-tagged biopolymers.^[16] Zhang and coworkers^[17] thoroughly elucidated the mechanism of conversion of ethylene oxide with CO₂ catalyzed by quaternary ammonium salts. In these studies, they obtained structural and energetic information concerning each step of the catalytic cycle and also evaluated the effect of the N-alkyl chain length and the type of anion. Furthermore, Han and coworkers^[18] studied in detail the KI catalyzed addition of CO₂ to propylene oxide, and also investigated the (co)catalytic role of glycerol and propylene glycol.



Scheme 4.2 (a) Schematic drawing of the Zn(salphen) catalyst; (b) substrates **1-6** used in this investigation.

Kleij and coworkers recently reported on the use of Zn(salphen) complexes (Scheme 4.2a) in conjunction with NBu₄I as efficient binary catalysts for the formation of cyclic carbonates under mild reaction conditions ($p\text{CO}_2 = 2\text{-}10$ bar; $T = 25\text{-}45^\circ\text{C}$).^[19] From these previous studies it has become clear that terminal epoxides are conveniently converted into their carbonates in high yield, whereas the same binary catalyst system proved to be rather ineffective for the conversion of internal and more sterically congested substrates. At a later stage, Kleij and coworkers found that more efficient catalysis of these latter substrates can be achieved when working under solvent-free, supercritical CO₂ conditions,^[20] giving highly improved conversion levels in much shorter time frames. As

reported extensively in literature, there are a variety of well-defined binary catalytic systems based on metallosalens^[21] and halide salts which provide efficient CO₂/epoxide addition catalysts under mild reaction conditions. Thus, the metallosalen family of catalysts could be regarded as privileged systems in the context of (cyclic) organic carbonate formation.

Furthermore, neutral and cationic chromium(II) salen-based complexes with N₄ Schiff base ligands have been reported to be very active catalysts for the coupling of CO₂ and epoxides in CH₂Cl₂ solutions and supercritical CO₂ conditions.^[22] Some tetradentate N₄-donor salen ligands have been earlier synthesized in high purity and were able to coordinate easily to a wide variety of metals (such as Cu, Co and Ni),^[23] but there is no application of these complexes as catalysts for CO₂ transformations.

Herein, a detailed DFT study on the mechanism for the formation of cyclic carbonates from CO₂ with a series of epoxides (Scheme 4.2b, compounds 1-6) catalyzed by the binary system Zn(salphen)/NBu₄X (X = Br, I) is reported. We have calculated the full energy profiles for various substrates and particularly focused on those aspects that help to explain the lower reactivities found for the more challenging substrates, providing new insights that are potentially useful for the development of more powerful catalyst systems. Moreover, the mechanistic profile involving N₂O₂-donor Zn(salphen) catalysts has been compared with the catalytic pathway obtained for a Zn(salen) complex containing N₄-donor Schiff base ligands, as mediator of the CO₂ addition reaction.

4.2 Motivation

Although various mechanistic proposals involving the catalyzed CO₂ addition had been put forward when we started this research, and in some cases even verified by experimental data,^[24] there was surprisingly limited information available regarding the major obstacles associated with the use of relatively more challenging substrates including those based on sterically congested oxiranes and internal epoxides. This in combination with previous findings by Kleij and coworkers^[19,20] using Zn(salphen)s as catalyst systems, prompted us to investigate these challenging conversions in more detail using computational methods.

We also became interested in the study of the reaction catalyzed by the Zn(salen) complexes based on N₄-donor Schiff base ligands, developed by Dr. Lorraine Christ from

Université de Lyon¹. Christ and coworkers employed those complexes for catalyzing the addition of CO₂ to epoxides affording excellent cyclic carbonates yields, but lower turnover frequencies (TOFs).

4.3 Objectives

Our main goal in this chapter is to investigate computationally the catalytic formation of cyclic carbonates from CO₂ and epoxides using Zn(salphen) complexes. We firstly address our efforts to understand every single step of the reaction mechanism by characterizing and computing relative free energies for all the intermediates and transition states in the catalytic process.

Once the energy profile for the coupling of CO₂ and propylene oxide is established, our objective is to evaluate the reaction mechanism including more sterically congested oxiranes and internal epoxides, and identify the factors controlling the catalytic process (steric or electronic).

Finally, a comparison regarding the activity of two different Zn(salen) catalysts including either “N₂O₂-donor” or “N₄-donor” Schiff base ligands will be established.

4.4 Computational details

All calculations were carried out by using the Amsterdam Density Functional (ADF v2010.01) package.^[25] DFT-based methods were employed at the generalized-gradient-approximation (GGA) level, with the Becke exchange^[26] and the Perdew correlation^[27] functional (BP86). A triple- ξ plus polarization Slater basis set was used on all atoms. Relativistic corrections were introduced by scalar-relativistic zero-order regular approximation (ZORA).^[28]

Full geometry optimizations were performed without constraints, and the nature of the stationary points in the potential energy hypersurface, were characterized either as minima or transition states by means of harmonic vibrational frequencies analysis. In order to match with the experimental conditions reported previously,^[19] standard corrections to Gibbs free energy were evaluated at 298 K and pressure of 1 bar. Additional corrections to adjust the experimental pressure (10 bar) were considered according to the expression of an ideal gas $G_m(p) = G_m^\circ + RT \ln \frac{p}{p^\circ}$.^[29] Solvent effects for dichloromethane (DCM) were

introduced through single point calculations on the gas-phase optimized structures by using the conductor-like screening model COSMO.^[30]

Calculations involving the hybrid B3LYP and M06 functionals were performed by using the Gaussian 09 package.^[31] The standard 6-311G(d,p) basis set was used to describe the H, C, N, and O atoms. The relativistic effective core pseudopotential LANL2DZ was used, together with its associated basis set, for Zn and I atoms. The zero-point, thermal, and entropy corrections were evaluated to compute enthalpies and Gibbs free energies ($T=298,15$ K, $p=1$ atm). Solvent effects for DCM have been introduced through single point calculations using the Polarizable Continuum Model (PCM).

4.5 Results

4.5.1 The uncatalyzed CO₂ addition reaction

The uncatalyzed addition of CO₂ to propylene oxide **1** can be achieved through a single step, leading to the formation of propylene carbonate (**PC**). The reaction in the absence of catalyst proceeds *via* nucleophilic attack either from an oxygen atom of CO₂ on the α carbon (most substituted carbon) or the β carbon (least substituted carbon) atom of **1**. The two calculated reaction pathways are shown in Figure 4.1, together with the optimized structures of the two transition states (TS).

The unique imaginary vibrational frequencies of TS- α and TS- β correspond to the simultaneous breaking of the C $_{\alpha}$ -O or C $_{\beta}$ -O bond of the epoxide and the simultaneous formation of two new C-O bonds which originate from the insertion of CO₂.

High energy barriers of 48.6 (α pathway) and 53.7 kcal·mol⁻¹ (β pathway) are involved to form the cyclic carbonate product. The α pathway is favored by 5.1 kcal·mol⁻¹ compared to β pathway. Previous DFT calculations reported by Zhang and coworkers^[12a] (at the B3PW91/6-311G(d) level) showed somewhat higher energy barriers of 53.4 kcal·mol⁻¹ for α pathway and 58.1 kcal·mol⁻¹ for the β pathway. Similar to the work from Zhang, Han and coworkers^[18] reported energy barriers of 55.3 and 61.4 kcal·mol⁻¹ (at the B3LYP/6-311++G(d,p)//B3LYP/6-31+G(d) level) for the α and β pathways, respectively.

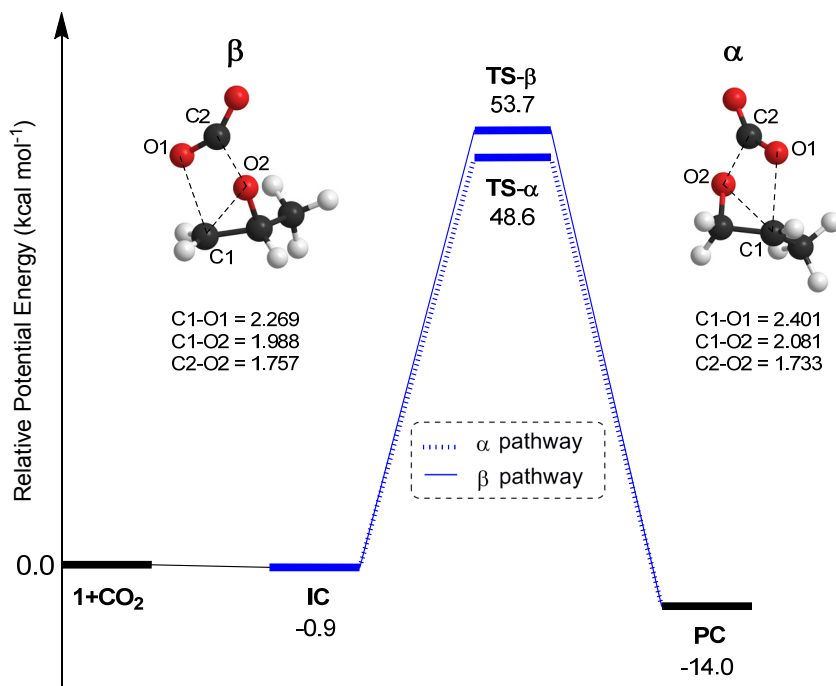


Figure 4.1 Potential energy profile for the uncatalyzed addition of CO₂ with propylene oxide **1** to give propylene carbonate (**PC**). **IC** stands for initial complex formation. Note that potential energy is here used to make a possible comparison with the literature data.

4.5.2 The Zn(salphen) catalyzed CO₂ addition reaction

Similar to the uncatalyzed reaction, the addition reaction of CO₂ to propylene oxide **1** catalyzed by the Zn(salphen) complex of Scheme 2 can involve two possible reaction pathways. The relative free energy profile of the α and β pathways are depicted in Figure 4.2, where the sum of energies of the isolated reactants (**1** + CO₂) and Zn(salphen) were set to zero. The initial step is the coordination of the epoxide to the Zn(salphen) complex forming an initial complex (**IC**) followed by a concerted ring-opening and CO₂ insertion step. For both pathways the only transition state relates to the simultaneous stretching/breaking of the C_α-O or C_β-O bond of the epoxide, and the bending of the CO₂ molecule leading to the formation of two new C-O bonds.

Once the coordinated cyclic carbonate is formed (**FC**) it is released from the Zn(salphen) complex allowing for further epoxide turnover. The calculated barriers for the exothermic reaction show that the α pathway is favored by 15.2 kcal·mol⁻¹ compared to the β pathway. The relative potential energy barrier for the Zn(salphen) catalyzed addition

(Figure 4.2, energy values in brackets) is reduced by 19.9 kcal·mol⁻¹ compared to the uncatalyzed reaction (i.e., 48.6 – 28.7 kcal·mol⁻¹) likely as a result of the formation of a Zn(salphen)/epoxide complex polarizing the C–O bond of the substrate and thus playing an important role in its activation.

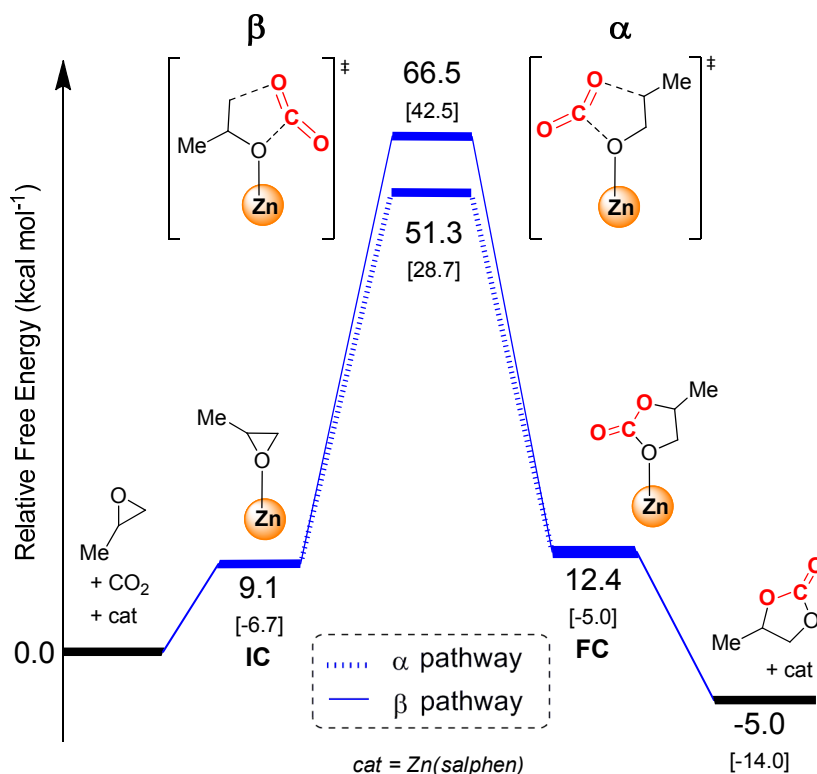


Figure 4.2 Free-energy profile for the Zn(salphen) catalyzed addition of CO₂ to propylene oxide **1**; the relative potential energy values are reported in brackets. IC stands for initial complex formation; FC stands for the final complex having the carbonate product coordinated.

4.5.3 The Zn(salphen)/NBu₄I catalyzed CO₂ addition reaction

In the previous discussion, the investigation of the uncatalyzed and the Zn(salphen) catalyzed mechanisms highlight that the ring-opening step is initiated by CO₂ leading to the direct formation of the cyclic carbonate. The high energy barriers found for this ring-opening process suggest that these reactions can thus only occur under harsh reaction conditions, i.e. high temperatures and/or pressures. As reported extensively in the literature,^[21] generally a binary catalytic system is needed in order to obtain good

conversions/yields under mild reaction conditions. The binary catalytic system usually combine a Lewis acid and a suitable nucleophile (most often a halide) that make the ring-opening procedure less energetically demanding and the subsequent CO₂ insertion easier. It should be noted that the nucleophiles themselves are able to catalyze the CO₂ addition to epoxides.^[6a,15,17,18] The most relevant computational result to the present study is the KI catalyzed ring-opening of propylene oxide reported by Han^[18] showing gas phase barriers in the range 36.3–37.6 kcal·mol⁻¹ depending on the reaction pathway. Maseras, Kleij and coworkers found a fairly similar barrier (38.9 kcal·mol⁻¹) when using NBu₄I as catalyst.^[3g] Thus, halide nucleophiles are able to significantly lower the transition state related to ring-opening of the epoxide (cf., values reported for the uncatalyzed reaction in Figure 4.1).

Zn(salphen) complexes have recently been shown to efficiently catalyze the addition reaction under mild reaction conditions, using quaternary ammonium halide salts as nucleophiles.^[19,20] Next we evaluated computationally the effect of combining both the Zn(salphen) as well as halide nucleophile (NBu₄X; X = Br, I) in the DFT analysis. Upon evaluation of this binary system the potential for two different catalytic pathways (α or β attack on the epoxide) was identified similar to the uncatalyzed and Zn(salphen) catalyzed addition reaction (Figures 4.1 and 4.2). DFT calculations were performed in the first instance on the simplest substrate, propylene oxide **1**.

It should be noted that for the envisioned mechanisms we have only considered pentacoordinated rather than hexacoordinated reaction intermediates. Hexacoordinated species have been frequently observed and proposed for other metallosalen catalysts comprising of Al,^[32] Mn,^[33] Co,^[34] and Cr^[35] metal ions, and in some of these cases (preliminary) mechanistic work has revealed that bimetallic pathways lead to more efficient catalytic processes. However, in the case of Zn(salphen)s, hexacoordination is an extremely rare phenomenon and is only observed in condensed solid phases.^[36] Furthermore, Kleij and coworkers^[37] and others^[38] have clearly demonstrated that pentacoordination in Zn(salphen)s is highly favored both in the solid state as well as in solution phases.^[37b,39] Therefore, the consideration of pentacoordination in the Zn(salphen) case seems to give a reasonable starting point in the mechanisms discussed below.

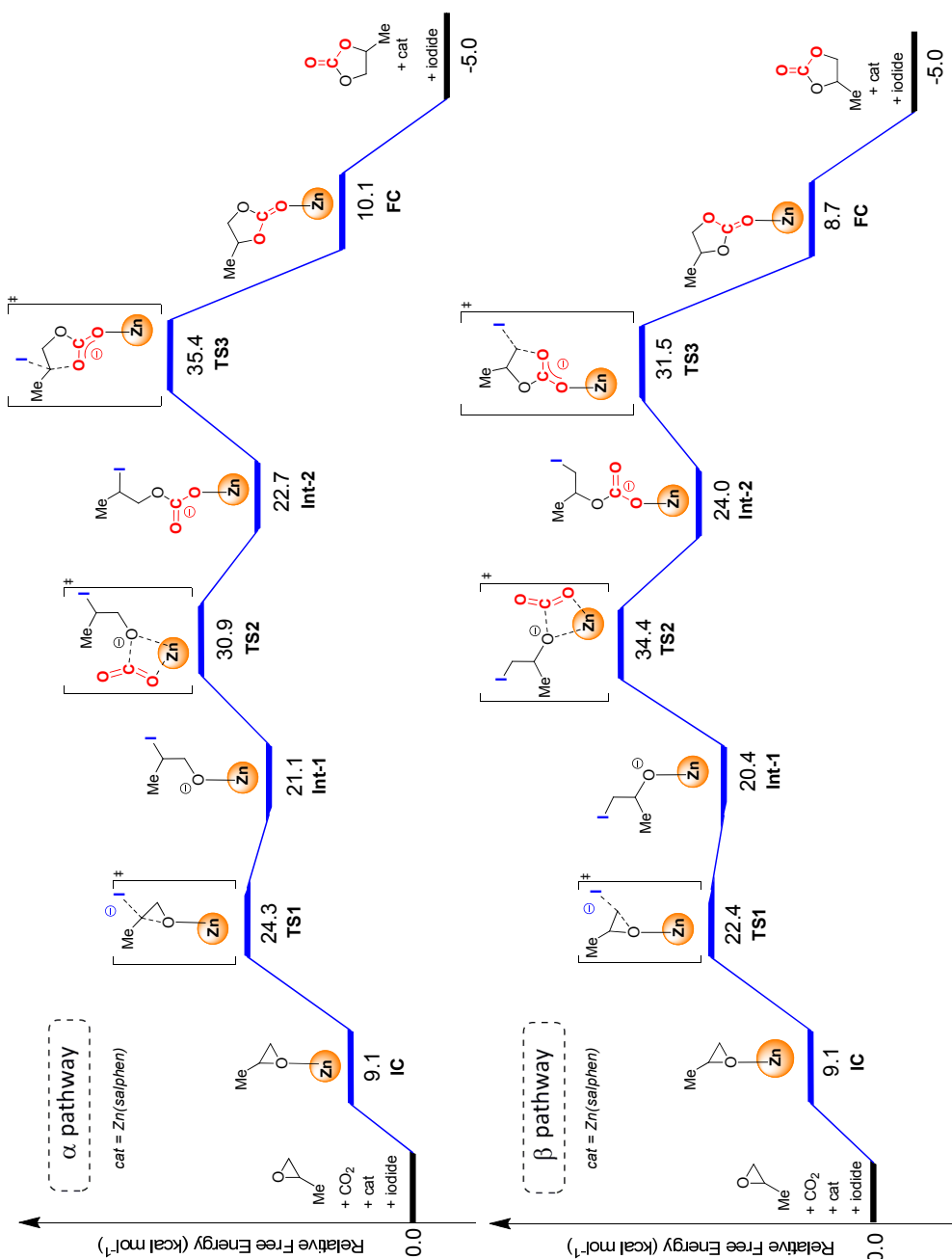
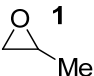
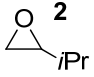
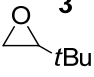
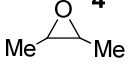
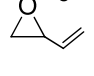
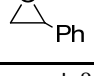


Figure 4.3 Free-energy profile for the addition of CO₂ to propylene oxide **1** catalyzed by Zn(salphen)/NBu₄I considering the α and β pathway. IC stands for initial complex formation; FC stands for the final complex having the carbonate product coordinated.

The resulting energy profiles of the α and β pathways are shown in Figure 4.3 with schematic representations of the involved intermediates and transitions states; in both cases the first step involves the coordination of **1** (**IC**) to the Zn(salphen) which, as mentioned before, polarizes the C–O epoxide bond thereby facilitating the ring-opening step.

It should be noted that the higher free energy for **IC** compared with the separate components is mainly due to an entropic cost for bringing together the Zn(salphen) and the epoxide ($-10.0 \text{ kcal}\cdot\text{mol}^{-1}$). The C–O bond polarization is supported by charge analysis of the carbon atoms of the epoxide revealing that both C_α and C_β become more electron-deficient (Table 4.1) compared with a non-coordinated epoxide.

Table 4.1 Calculated Mulliken populations for free and epoxides **1-6** coordinating to Zn(salphen).

Substrate ^a	Epoxide ^b	Epoxide-Zn(salphen)
 1	1 C_α	0.47
	1 C_β	0.50
 2	2 C_α	0.52
	2 C_β	0.50
 3	3 C_α	0.55
	3 C_β	0.49
 4	4 C_α	0.48
	4 C_β	0.48
 5	5 C_α	0.44
	5 C_β	0.49
 6	6 C_α	0.40
	6 C_β	0.49

^a The α and β designations relate to their respective carbon atoms. ^b Mulliken population in electronic charge.

After initial coordination of the epoxide to the Zn(salphen) complex (cf., **IC**), the ring-opening step occurs *via* nucleophilic attack of the iodide. The first transition state (**TS1**) is

characterized by the breaking of C_{αβ}-O bond and the simultaneous formation of a C_{αβ}-I bond as confirmed by the unique imaginary frequency for the attack at C_α and for C_β (Figure 4.4).

In the case of β pathway, the epoxide ring-opening is energetically more favorable by almost 2.0 kcal·mol⁻¹ compared with the α pathway. In the subsequent step, a molecule of CO₂ reacts with the negatively charged oxygen atom (insertion) of the intermediate **Int-1** leading to the formation of linear carbonate **Int-2**. The second transition state **TS2** involves the formation of new C-O and Zn-O bonds that involve the CO₂ molecule as shown in the relative imaginary frequencies at 58.3i cm⁻¹ for the α pathway and 51.7i cm⁻¹ for the β route (Figure 4.4). In the pathway related to the β attack, this step is rate-determining with a free energy value of 34.4 kcal·mol⁻¹, in the α pathway this step has a free energy of 30.9 kcal·mol⁻¹ and is thus more facile. The reason for this difference between the two pathways has mainly a steric origin; the position of the methyl group in the β pathway is closer to the O-atom of the epoxide making the insertion of CO₂ more difficult (see Figure 4.4).

The linear carbonate intermediate **Int-2** undergoes an intramolecular ring-closing with the concomitant release of the iodide nucleophile and formation of the **FC**. In this latter step the carbon atom bound to the iodide binds to the nearest oxygen atom forming a new C-O bond; at the same time, the iodide bond elongates until it breaks (Figure 4.4). The ring-closing step is found to be the rate-determining step in the α pathway with free energy of 35.4 kcal·mol⁻¹. Similar to the CO₂ insertion step, the methyl group on the C_α makes the ring-closing step more difficult in the α pathway, whereas in the β pathway the intermediate linear carbonate is in a more suitable conformation for the ring-closing event.

Once formed, the cyclic carbonate is released from the Zn(salphen) complex allowing further epoxide turnover. The overall reaction is exergonic with a release of 5.0 kcal·mol⁻¹. The synergistic effect of the binary Zn(salphen)/NBu₄I catalyst system makes the synthesis of the cyclic carbonate much more accessible.

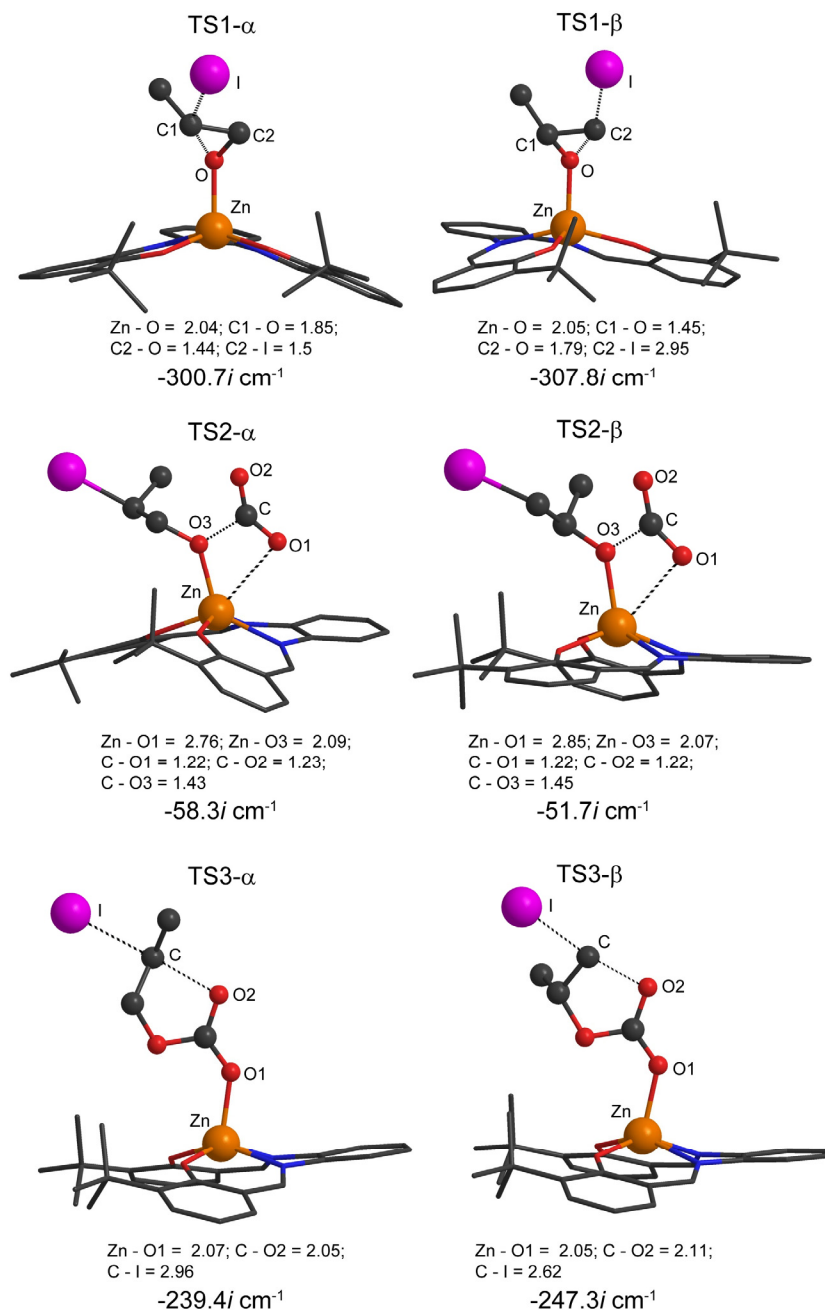


Figure 4.4 Optimized structures for the transition states **TS1–TS3** for both the α and β pathway together with the most relevant calculated distances (in Å) and value of the negative (imaginary) vibrational frequencies using propylene oxide **1** as substrate.

In particular, the high Lewis acidity of the Zn(salphen) complex^[40] strongly reduces the energy barrier for the ring-opening step through a polarization of the epoxide carbon atoms (48.6 kcal·mol⁻¹ for the uncatalyzed reaction to 7.0 kcal·mol⁻¹ for the binary catalyst; both energy values refer to potential energy), allowing the nucleophile to attack more easily.

As shown in the energetic profiles in Figure 4.3 there are some important differences between the α and β pathway using propylene oxide **1** as substrate. First, in the ring-opening step, in contrast with the uncatalyzed reaction, the attack at the β carbon is favored. Second, the rate-determining steps of the α and β pathways are at different points during the catalytic cycle; the ring-closing step in the α pathway and the CO₂ insertion step in the β pathway. This is a consequence of the different position in which the methyl substituent is located during the two possible pathways.

4.5.4 Ring-closing mechanism

As already shown in Figure 4.3, the ring-closing step involves the formation of a new C–O bond in both pathways, but when considering the linear intermediate **Int-2** there are two possible routes leading to the cyclic carbonate product through either O–atom of the carbonate (Figures 4.5a and 4.6a, O1 and O2).

In order to establish which ring-closing mechanism is preferred, the energy profiles for both possible intramolecular nucleophilic pathways were calculated. It can be seen in Figures 4.5 and 4.6 that when ring-closing occurs *via* the non-coordinating O-atom O2 (**RC1**) only one step is required evolving through **TS3** giving the final intermediate **FC**. When the nucleophilic attack is made by O1 (i.e., through pathway **RC2**), a multi-step mechanism would be operative going first through **TS3'** that after skeletal rearrangement affords **Int-3** followed by ring-closing in **TS4** giving **FC'**. The distinction between complexes **FC** and **FC'** is a consequence of which O–atom (O1 or O2) takes part in the ring closing step.

The comparison between the two pathways indicates that **RC1** is favored over **RC2** as a result of the fewer steps required and also the lower energy requirement for **TS3** regarding **TS4** (35.4 kcal·mol⁻¹ for **RC1** compared to 37.9 kcal·mol⁻¹ for **RC2** in case of the α pathway; and 31.5 kcal·mol⁻¹ for **RC1** compared to 32.7 kcal·mol⁻¹ for **RC2** in case of the β pathway).

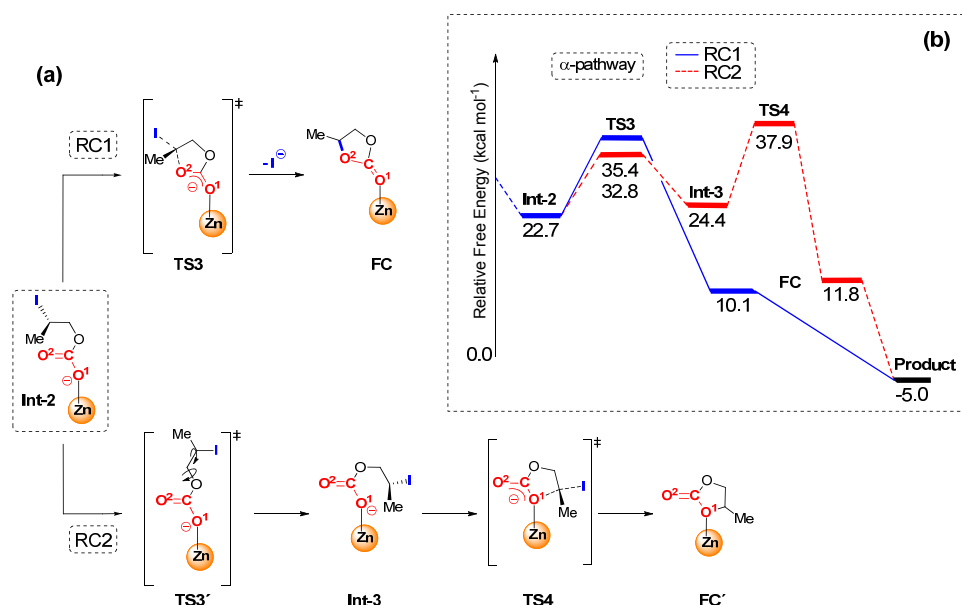


Figure 4.5 (a) Two possible ring-closing pathways (RC1 and RC2) for the intermediate Int-2 involving different O-atoms of the carbonate fragment (O1 and O2) in the formation of propylene carbonate. (b) Free energy profile for the ring-closing step in the α pathway for the conversion of propylene oxide **1** catalyzed by the binary Zn(salphen)/NBu₄ catalyst.

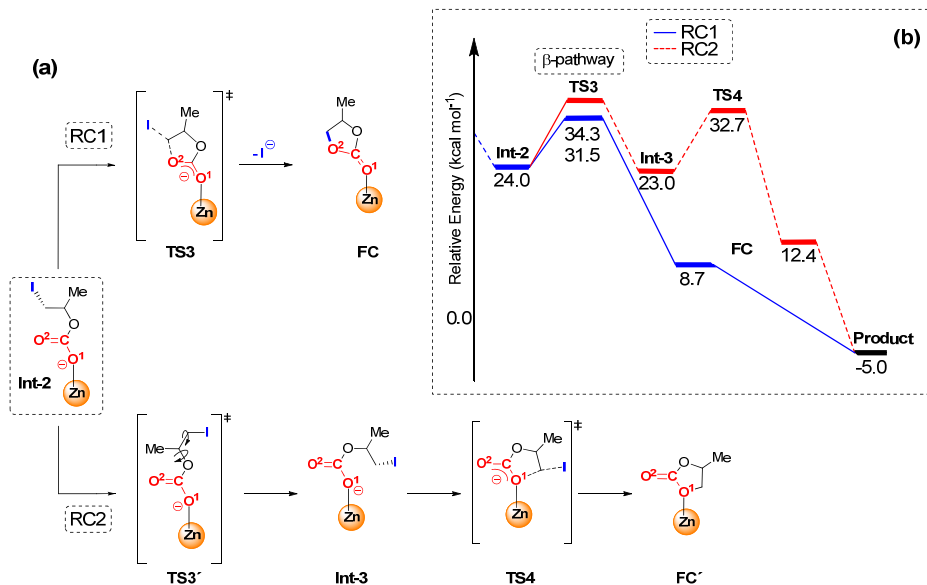


Figure 4.6 (a) Two possible ring-closing pathways (RC1 and RC2) for the intermediate Int-1 involving different O-atoms of the carbonate fragment (O1 and O2) in the formation of propylene carbonate. (b) Free energy profile for the ring-closing step in the β pathway for the conversion of propylene oxide **1** catalyzed by the binary Zn(salphen)/NBu₄ catalyst.

4.5.5 The Zn(salphen)/NBu₄Br catalyzed CO₂ addition reaction

Kleij and coworkers^[19a] previously observed that NBu₄I proved to be a better cocatalyst than NBu₄Br giving higher conversion levels when using 1,2-epoxyhexane as substrate. Therefore, the effect of using bromide as the nucleophile instead of iodide was evaluated for both the α and β pathway during the addition of CO₂ to propylene oxide **1**. The first two entries of Table 4.2 show that the α pathway is less energetically demanding compared to β pathway and the rate-determining step in the latter is, as calculated for the same pathway using iodide as nucleophile (Figure 4.3), the CO₂ insertion step (36.5 kcal·mol⁻¹). In the ring-opening step, bromide favors the nucleophilic attack at the β carbon by 2.6 kcal·mol⁻¹ compared with the α -carbon. When comparing both nucleophiles in the β pathway, the use of bromide (19.6 kcal·mol⁻¹) thus lowers the barrier for the ring-opening (**TS1**) of propylene oxide compared to iodide (22.4 kcal·mol⁻¹) but higher barriers are found for the other two steps, i.e. **TS2** and **TS3**. Thus, these results are in line with the experimental data obtained for the binary catalyst Zn(salphen)/NBu₄X (X = Br, I) showing generally somewhat higher activity when iodide is used as nucleophile, and in particular in the conversion of terminal epoxides through the β pathway that shows less dependency on the steric requirements of the catalyst.^[19,20]

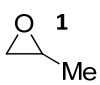
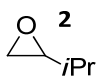
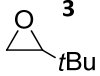
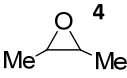
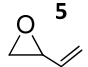
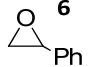
4.5.6 Effect of epoxide substituent

So far focus has been on the addition of CO₂ using propylene oxide **1** as substrate. In order to study the influence of the steric bulk/substitution pattern in the epoxide, further substrates **2-6** (Scheme 4.2, page 78) were considered. When the steric bulk of the C _{α} substituent is increased (methyl \rightarrow isopropyl \rightarrow *tert*-butyl), the barriers related to the transition states **TS1–TS3** significantly increase and thus reveal that conversion of more sterically encumbered substrates is more difficult in line with previous experimental findings using Zn(salphen)s as catalysts.^[19,20]

Furthermore, for the ring-opening of the epoxides **1-3** a clear increase in the difference in energy for **TS1** can be noted when comparing the α and β pathway in the series **1** \rightarrow **2** \rightarrow **3** (Figure 4.7), and overall the β pathway becomes more favourable. Similar to the calculated mechanism of **1** (Figure 4.3) we observe that with epoxides **2** and **3** the rate-limiting step

does not change and remains the CO₂ insertion for the β pathway and the ring-closing step for the α pathway.

Table 4.2 Calculated free-energy values for the three transition states in the addition of CO₂ to epoxides **1-6** at 25°C.^a

Substrate ^b		Nucleophile	TS1 ^c [kcal·mol ⁻¹]	TS2 ^c [kcal·mol ⁻¹]	TS3 ^c [kcal·mol ⁻¹]
	1α	Br	22.2	33.5	33.9
	1β	Br	19.6	36.5	32.0
	1α	I	24.3	30.9	35.4
	1β	I	22.4	34.4	31.5
	2α	I	26.9	31.2	33.7
	2β	I	23.1	38.4	34.5
	3α	I	31.0	41.1	41.2
	3β	I	25.8	44.4	36.3
	4	I	29.5	38.5	40.0
	5α	I	20.0	35.1	32.2
	5β	I	23.5	37.1	35.7
	6α	I	26.0	36.0	36.3
	6β	I	27.5	42.9	40.0

^a Transition states: **TS1** refers to the ring-opening of the epoxide, **TS2** to the CO₂ insertion step and **TS3** to the energetically most favored ring-closing pathway. ^b The α and β designations relate to their respective pathways. ^c The energies indicate a system in which the CO₂ pressure is 10 bar as previously used.^[19]

As an example of an internal epoxide, the reaction mechanism of *trans*-2,3-epoxybutane **4** has also been calculated as, experimentally, **4** has been shown to be a significantly less reactive substrate^[19] and as a result it was necessary to employ much harsher reaction conditions (i.e., higher temperatures and pressures) for successful conversion compared with terminal epoxides.^[20] As reported in Table 4.2, all the transition states of **4** have a relatively high energy compared with propylene oxide **1**, and thus the presence of two methyl substituents creates significant steric hindrance in the epoxide to

raise the energy barriers for all three steps. These barriers could be overcome by using supercritical CO₂ (conditions used: 80°C, *p*CO₂ = 80 bar) as reaction medium^[20] allowing for good conversion of **4** using Zn(salphen)/NBu₄Br as a binary catalyst.

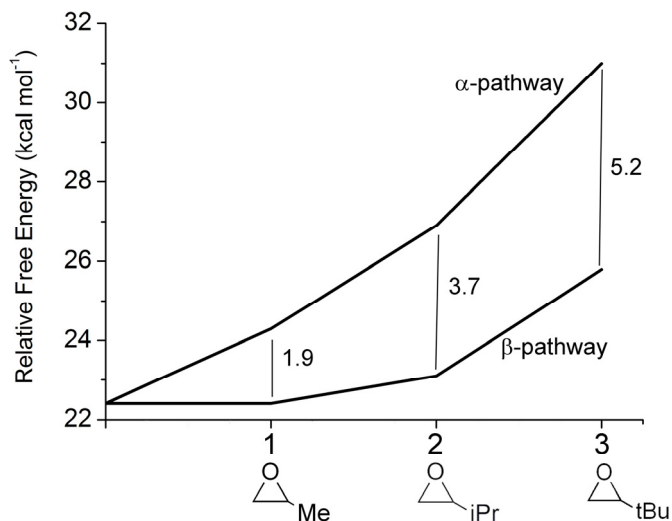


Figure 4.7 Free-energy differences between α pathway and β pathway in the ring-opening step for epoxides **1**, **2** and **3**.

From the computational data presented thus far, it seems reasonable to assume that for epoxide substrates **1-4** steric effects are dominant and electronic effects play a less important role. Whereas most terminal epoxides are easily converted into their respective cyclic carbonates, in general substrates **5** and **6** (Scheme 4.2, page 78) are slightly more sluggish and show lower conversion levels with various catalyst systems. Therefore, also the conversion of these substrates with the binary Zn(salphen)/NBu₄I catalyst was investigated in detail using DFT calculations (Table 4.2). In the case of 2-vinyloxirane **5** (Scheme 4.2, page 78), the presence of the vinyl functionality makes the ring-opening step more favorable on C_α unlike the clear preference for C_β observed with epoxides **1-3**. This is a result of a larger stabilization of **TS1** through delocalization of the charge in the linear alkoxide through the vinyl fragment; this is likely also the case in **Int-1** making the coordinated alkoxide less nucleophilic. In line with the lower reactivity is the higher barrier found for the CO₂ insertion step (**TS2**, 35.1 kcal·mol⁻¹) compared to 30.9 kcal·mol⁻¹ using **1** as substrate. Figure 4.8a shows the difference in the first transition states **TS1** for both

pathways using epoxide **5**. In the α pathway the four carbon atoms are lying in the same plane allowing π -conjugation and consequently higher stabilization of the system. In contrast with the trend seen for substrates **1-3**, for **5** the α pathway is more favorable compared with the β pathway and the CO₂ insertion step is rate-limiting.

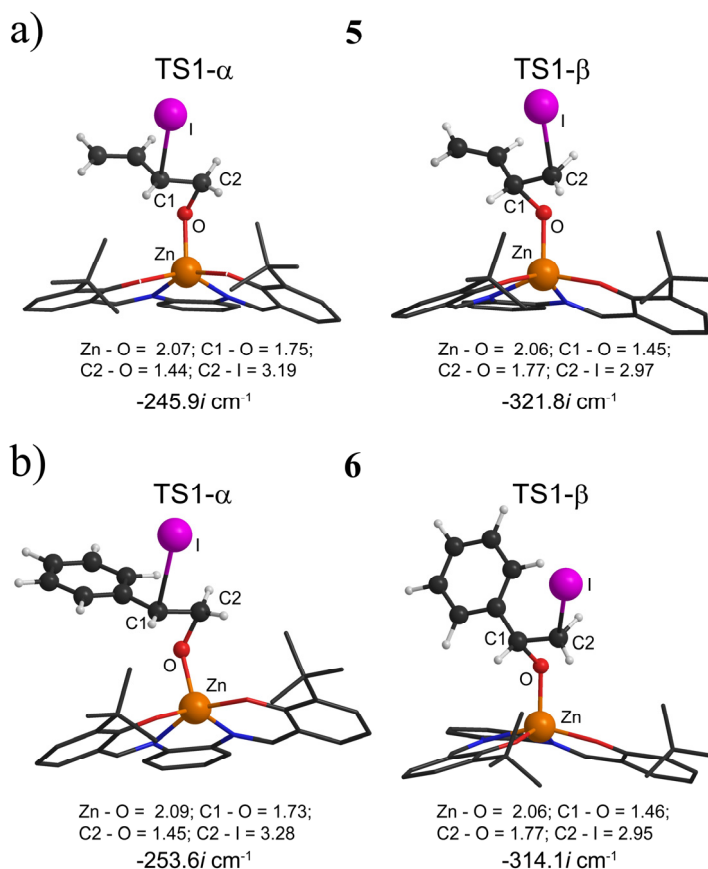


Figure 4.8 Optimized structures of **TS1** in α and β pathways for epoxides (a) **5** and (b) **6** together with the most relevant calculated bond distances (in Å), and value of the negative (imaginary) vibrational frequencies.

For styrene oxide **6** (Figure 4.8b) the presence of the phenyl substituent also favors the α pathway, and in particular the transition state **TS2** related to the CO₂ insertion step is markedly lower (36.0 kcal·mol⁻¹) compared to the β pathway (42.6 kcal·mol⁻¹) but again higher than observed with propylene oxide **1** (33.5 kcal·mol⁻¹). In the first transition state **TS1** similar to **5** a planar conformation allows the aromatic ring to stabilize the charge in

the coordinated alkoxide. In the transition state describing the ring-closing step **TS3-6 α** again the inductive effect of the phenyl group is responsible for stabilization of the charge resulting from the release of iodide. Experimental data with the binary Zn(salphen)/NBu₄I catalyst system^[19] are fully in line with these computational findings for substrates **5** and **6** and have shown that these latter epoxides have lower conversion levels compared to other terminal epoxides such as propylene oxide **1**. For **6** both **TS2** (CO₂ insertion) and **TS3** (ring-closing step) have similar (rate-determining) barriers of around 36.0 kcal·mol⁻¹. The preference for ring-opening at C _{α} in both **5** as well as **6** (i.e., the methine carbon) follows the observations from Darensbourg, Lu and coworkers who studied the Co^{III}-salen catalyzed formation of polycarbonates based on CO₂ and epichlorohydrin^[41] or styrene carbonate;^[42] in these cases a higher preference for the α pathway in these epoxides with electron-withdrawing groups was noted compared to propylene oxide **1**.

The DFT analysis suggest that for catalyst improvement, and specifically for those substrates that are sterically more demanding such as internal epoxides, metallosalen systems having a planar coordination environment cannot be effective mediators under mild reaction conditions. In order to create more space to facilitate both the sterically demanding CO₂ insertion and ring-closing steps (which have shown to be more challenging than the ring-opening of the epoxide, see Table 4.1) other ligand geometries (Figure 4.8) should be considered such as metal complexes comprising of a trigonal bipyrimidal (TBP) coordination environment.

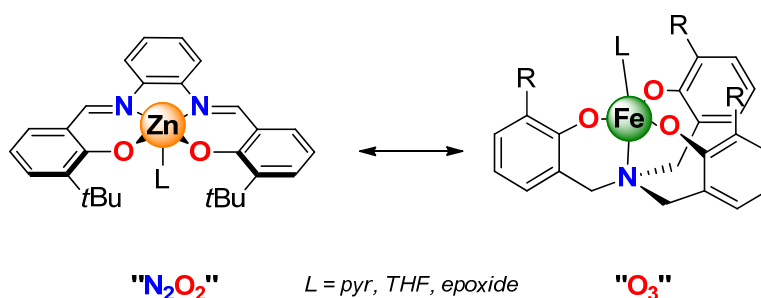


Figure 4.9 Schematic representation and comparison of the coordination geometry in the plane of the metal centres in Zn(salphen) complexes and Fe-based amino triphenolates.

Recent work from Kleij and coworkers concentrating on Fe^{III}-based amino triphenolate complexes^[3c,43] with these NO₃-chelating ligands in combination with an external ligand

such as pyridine, THF or an epoxide (Figure 4.9) provide a TBP coordination arrangement; these complexes have indeed proven to be more effective catalyst systems with lower metal loadings (0.1-0.5 mol% Fe versus 2.5 mol% Zn) and able to convert internal epoxides and oxetanes. Further chapters will address studies involving these kinds of complexes as potential and powerful catalytic systems for the formation of cyclic carbonates and also for the synthesis of polycarbonates.

4.5.7 Evaluation of the reaction with different DFT functionals

In order gain insights into the accuracy of the computational methodology used in this study, we computed free-energy profiles for the catalyzed CO₂ addition reaction by using the hybrid functional B3LYP and also a functional including somewhat dispersion such as M06. Table 4.3 collects the relative free energies obtained for all transition states and intermediates involved in the catalytic addition of CO₂ to propylene oxide **1** calculated at the B3LYP and M06 levels.

Only the β pathway was considered for calculating the reaction energy profile with the B3LYP functional, as shown in the first entry of Table 4.3. The estimated free energies resulted in slightly lower barriers (between 1.0 and 3.0 kcal·mol⁻¹) compared with those achieved with BP86 (Figure 4.3). However, similar mechanistic steps as described for the BP86 profile were obtained using B3LYP. In general, the CO₂ insertion step (**TS2**) was found to be rate-determining, with activation barrier of 33.1 kcal·mol⁻¹. The overall reaction (ΔG_r) resulted a bit exothermic by 3.0 kcal·mol⁻¹.

Table 4.3 Free-energy values (kcal·mol⁻¹) calculated for transition states and intermediates in the addition of CO₂ to epoxide **1** at the M06 and B3LYP levels.

Functional	Pathway	IC	TS1	Int-1	TS2	Int-2	TS3	FC	ΔG_r
B3LYP	1 β	4.7	21.6	17.4	33.1	22.0	29.4	3.7	-2.0
	1 α	-2.1	16.8	5.5	11.7	7.8	24.6	1.0	-1.4
M06	1 β	-2.1	14.9	4.0	14.7	5.6	22.4	0.8	-1.4

Similarly, the α and β pathways for propylene oxide **1** catalyzed by the Zn(salphen)/NBu₄I binary system were computed using the M06 functional. The relative energies of the different TS shown in Table 4.3 proved to lower and markedly different

(comparing **TS1** with **TS2/TS3**), though the **TS1** (i.e., ring-opening step) showed to be relatively more demanding.

Unlike for the mechanism calculated at both BP86 and B3LYP levels (Figure 4.3), for the M06 profile the initial coordination of the Zn(salphen) catalyst and the epoxide **1** (**IC**) is slightly exothermic by 2.1 kcal·mol⁻¹. Closer inspection of the **TS1** conformation shows that the M06 method favors the iodide attacking the coordinated epoxide from the side where the tBu groups of the Zn(salphen) are located (α pathway), as depicted in Figure 4.10. In the β pathway this observation is less pronounced. Thus, the use of M06 favors the steric bulk of the Zn(salphen), the coordinated epoxide and the incoming (large) iodide nucleophile to reside in the same area of space.

The use of dispersion favors the CO₂ insertion step (**TS2**), with bigger effect in the α pathway by 3.0 kcal·mol⁻¹ compared with the β pathway. The high free-energy barriers required to overcome **TS3** in both pathways (24.6 and 22.4 kcal·mol⁻¹ for the α and β pathways, respectively) indicates that the ring-closing step is rate-determining. The overall reaction is slightly exergonic with a release of 1.4 kcal·mol⁻¹.

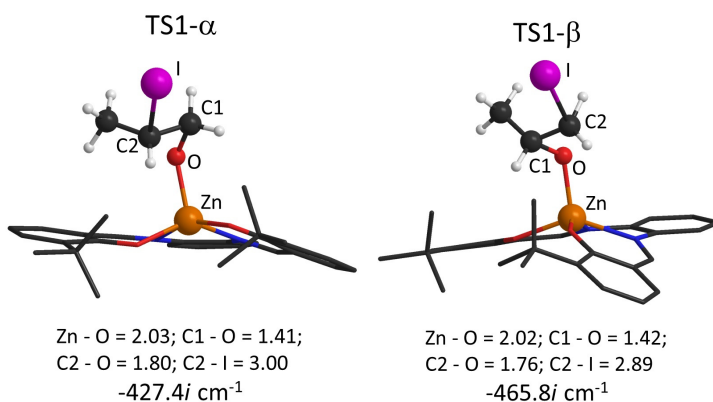
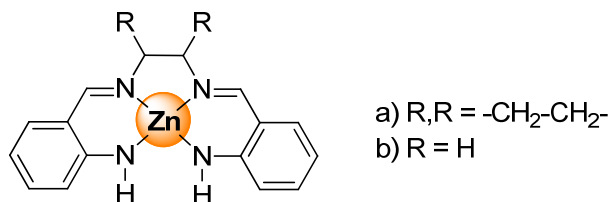


Figure 4.10 Optimized structures of **TS1** in α and β pathways for epoxide **1** together with the most relevant calculated bond distances (in Å), and value of the negative (imaginary) vibrational frequencies, calculated with the M06 functional.

4.5.8 The Zn-N₄(salen)/NBu₄I catalyzed CO₂ addition reaction

We also investigated the mechanism for the addition of CO₂ to propylene oxide **1** catalyzed by the binary system composed of a Zn(salen) complex containing N₄-donor Schiff base ligands (Scheme 4.3), in conjunction with NBu₄I. Experimentally, this catalyst system has

been found to be very active for the CO₂ addition reaction in dichloromethane solutions under mild conditions (p_{CO_2} =10 bar; T=100°C; 18h), affording epoxide conversions in a range of 82-97 and yields up to 96%, and low turnover frequencies (TOFs).^[44]



Scheme 4.3 Schematic representation of the Zn(salen) complexes containing N₄-donor Schiff base ligands.

In Figure 4.11 are illustrated the α and β pathways for the reaction mediated by the Zn-N₄(salen) complex **a** (from Scheme 4.3) calculated with the BP86 and M06 functionals, as well as the β pathway obtained using B3LYP. In general, the reaction follows the same mechanistic steps as that achieved with the Zn(salphen)/iodide catalyst system (i.e., ring-opening step, CO₂ insertion and ring-closing step). It is noteworthy that unlike for the latter system, with the Zn-N₄(salen) complex higher relative barriers were found for all the pathways; thus for example, Figure 4.11 shows the comparison with free energies (in parenthesis) calculated at the BP86 level for the β pathway of the Zn(salphen) catalyzed reaction. However, the α/β preference for the epoxide ring-opening and the rate-determining steps are maintained as further described.

The initial coordination of the epoxide to the Zn-N₄(salen) complex (**IC**) is endergonic in all the cases, which indicates that the salen complex containing N₄-donor Schiff base ligands is a less Lewis acid mediator than the Zn-salphen complex. Therefore, the subsequent barriers involved in the reaction mechanism are much more uphill.

Because the β carbon is more nucleophilic than the α one (see Table 4.1, page 86), the iodide attack occurs favorably on this carbon (**TS1- β** in Figure 4.12), as previously stated. Once formed the intermediate **Int-1** the following step (insertion of CO₂) affords the linear carbonate **Int-2** through the transition state **TS2** depicted in Figure 4.12. The last step is the concerted ring-closing reaction *via* the carbonyl oxygen of the carbonate through **TS3** (Figure 4.12) giving the final intermediate **FC**. This latter process is rate-determining for the

α pathway at the BP86 level (40.9 kcal·mol⁻¹) and also for the α and β M06 pathways by 28.5 and 26.1 kcal·mol⁻¹, respectively. Moreover, **TS2** corresponds to the rate-determining step of the β pathways calculated with BP86 and B3LYP functionals, with barriers of 41.8 and 37.2 kcal·mol⁻¹, correspondingly.

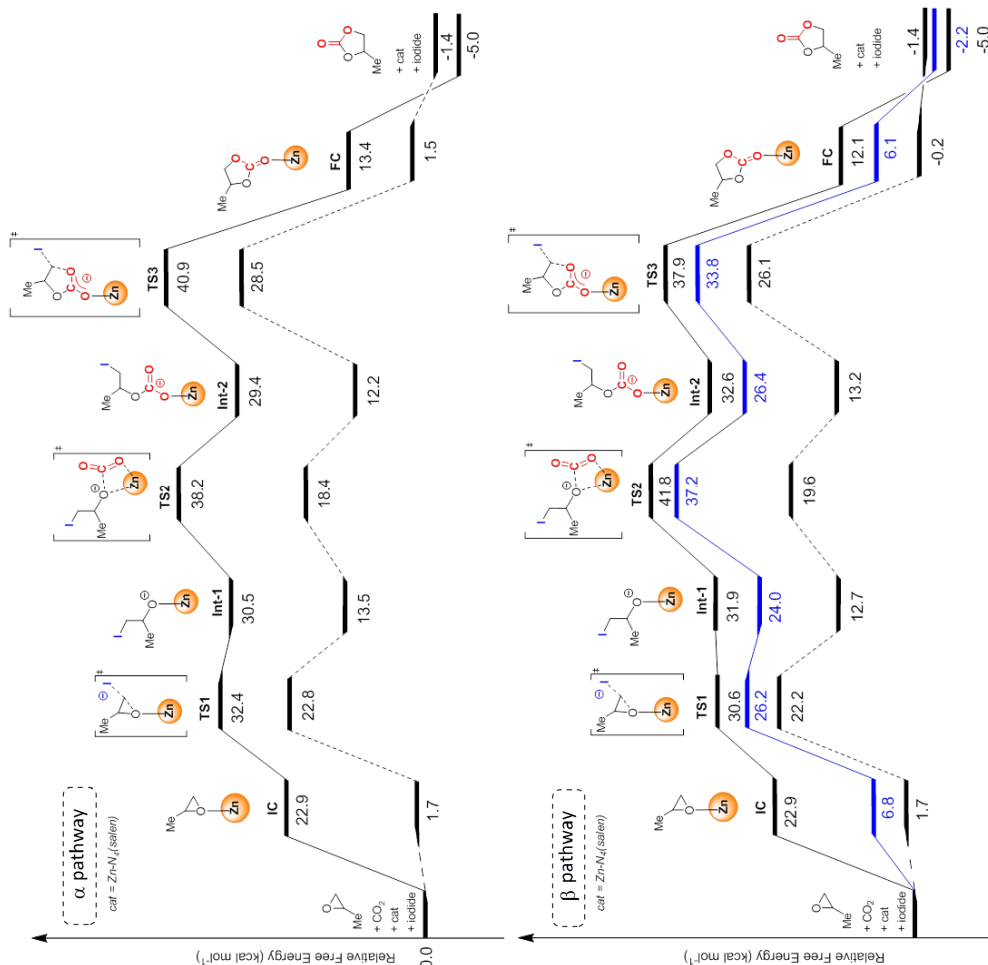


Figure 4.11 Free-energy profiles for the addition of CO₂ to propylene oxide **1** catalyzed by Zn-N₄(salen)/NBu₄I considering the α and β pathways at the BP86 (in solid line) and M06 (in dashed line) DFT levels. Free-energy values (at the BP86 level) for the reaction mediated by the Zn(salphen) complex are in parenthesis (in gray) for comparison with the Zn-N₄(salen). The β pathway calculated at the B3LYP level appears in blue color. **IC** stands for initial complex formation; **FC** stands for the final complex having the carbonate product coordinated.

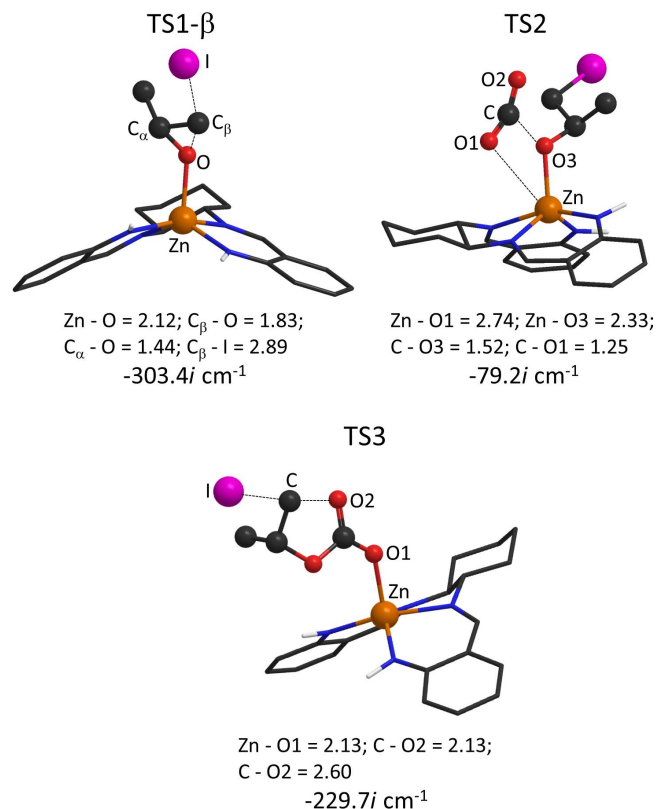


Figure 4.12 Optimized structures for the transition states **TS1–TS3** for the β pathway at the BP86 level, together with the most relevant calculated distances (in Å) and value of the negative (imaginary) vibrational frequencies using propylene oxide **1** as substrate.

The above results suggest that the catalytic system comprising the Zn-N $_4$ (salen) complex **a** is less active than the Zn(salphen) containing the “N $_2$ O $_2$ ” Schiff base ligands, for the formation of cyclic carbonates from CO $_2$ and propylene oxide. However, some caution may be needed when comparison between the outcome from different experiments (in which, different catalysts, substrates, and experimental conditions are used) is made. Our computed DFT activation energies are in line with the experimental results, at least in a qualitatively correct manner. Moreover, in some cases we can even reach quantitative agreement, as discussed below (Chapter 5).

4.6 Conclusions

The mechanism for the addition of CO₂ to epoxides catalyzed by the binary Zn(salphen)/NBu₄X (X = Br, I) catalyst system has been investigated and elucidated in detail by DFT methods.

Computational studies clearly explain the reasons why the addition of CO₂ to the benchmark substrate propylene oxide **1** proceeds in a much easier way in presence of Zn(salphen)/NBu₄I compared to the uncatalyzed or Zn(salphen) catalyzed route.

For substrates **1–3** ring-opening at the unsubstituted carbon atom (β pathway) is favored and this preference becomes more pronounced upon increasing the steric bulk at C _{α} . In general the β pathway is favored and the rate-limiting step for these substrates is the CO₂ insertion step in the coordinated linear alkoxide complex. In contrast to **1–3**, for substrates **5** and **6** the α pathway is favored with the CO₂ insertion step also being rate-determining.

For alkyl-substituted terminal epoxides **1–4** the reaction is predominantly controlled by steric factors, whereas for the vinyloxirane **5** and styrene oxide **6** electronic factors are more dominant.

The current results also explain why internal epoxides such as *trans*-2,3-epoxybutane **4** are more sluggish as all the involved calculated transition states (**TS1–TS3**) are significantly higher compared to those computed for propylene oxide **1**.

We believe that this comprehensive study based on the addition of CO₂ to various epoxides gives useful insights in the limitations of a very important family of catalysts (metalloalens) and provides a deeper understanding of this well-known CO₂ fixation reaction.

The catalyzed reaction involving the Zn-N₄(salen) complex resulted in higher relative free energies than those obtained for the Zn(salphen)/NBu₄I catalyzed route. This indicates that the Zn(salen) complex containing N₄-donor Schiff base ligands is a less active catalyst system for mediating the addition of CO₂ to epoxides.

Based on recent promising findings with other types of binary catalyst systems (amino trisphenolate complexes) having different coordination environments around the active metal center, the development of more active/selective catalysts for organic carbonate synthesis from epoxides and carbon dioxide should be feasible.

4.7 References and notes

- [1] a) *Carbon Dioxide as Chemical Feedstock*, M. Aresta (ed), Wiley-VCH, Weinheim **2010**; b) P. Markewitz, W. Kuckshinrichs, W. Leitner, J. Linsen, P. Zapp, R. Bongartz, A. Schreiber, T. E. Müller, *Energy Environ. Sci.* **2012**, *5*, 7281; c) T. Sakakura, J. C. Choi, H. Yasuda, *Chem. Rev.* **2007**, *107*, 2365.
- [2] a) R. Martín, A. W. Kleij, *ChemSusChem* **2011**, *4*, 1259; b) M. Peters, B. Köhler, W. Kuckshinrichs, W. Leitner, P. Markewitz, T. E. Müller, *ChemSusChem* **2011**, *4*, 1216; c) M. Cokoja, C. Bruckmeier, B. Rieger, W. A. Herrmann, F. E. Kühn, *Angew. Chem. Int. Ed.* **2011**, *50*, 8510.
- [3] For recent original contributions: a) M. North, C. Young, *Catal. Sci. Technol.* **2011**, *1*, 93; b) A. Coletti, C. J. Whiteoak, V. Conte, A. W. Kleij, *ChemCatChem* **2012**, *4*, 1190; c) C. J. Whiteoak, E. Martin, M. Martínez Belmonte, J. Benet-Buchholz, A. W. Kleij, *Adv. Synth. Catal.* **2012**, *354*, 469; d) T. Ohshima, J. Okudac, K. Mashima, *Catal. Sci. Technol.* **2012**, *2*, 509; e) T. Ema, Y. Miyazaki, S. Koyama, Y. Yano, T. Sakai, *Chem. Commun.* **2012**, *48*, 4489; f) J. Qu, C.-Y. Cao, Z.-F. Dou, H. Liu, Y. Yu, P. Li, W.-G. Song, *ChemSusChem* **2012**, *5*, 652; g) C. J. Whiteoak, A. Nova, F. Maseras, A. W. Kleij, *ChemSusChem* **2012**, *5*, 2032; h) Q.-W. Song, L.-N. He, J.-Q. Wang, H. Yasuda, T. Sakakura, *Green Chem.* **2013**, *15*, 110; i) C. Qi, J. Ye, W. Zeng, H. Jiang, *Adv. Synth. Catal.* **2010**, *352*, 1925; j) J. Sun, L. Han, W. Cheng, J. Wang, X. Zhang, S. Zhang, *ChemSusChem* **2011**, *4*, 502.
- [4] For a biography on phosgene and its derivatives see: a) D. D. Berolzheimer, *Ind. Eng. Chem.* **1919**, *11*, 263; b) A.-A. G. Shaikh, S. Sivaram, *Chem. Rev.* **1996**, *96*, 951.
- [5] a) T. Sakakura, K. Kohno, *Chem. Commun.* **2009**, 1312; b) A. A. G. Shaikh, S. Sivaram, *Chem. Rev.* **1996**, *96*, 951; c) B. Schöffner, F. Schöffner, S. P. Verevkin, A. Börner, *Chem. Rev.* **2010**, *110*, 4554; d) D. J. Darensbourg, S. J. Wilson, *Green Chem.* **2012**, *14*, 2665.
- [6] a) V. Caló, A. Nacci, A. Monopoli, A. Fanizzi, *Org. Lett.* **2002**, *4*, 2561; b) B. R. Buckley, A. P. Patel, K. G. Wijayantha, *Chem. Commun.* **2011**, *47*, 11888.

- [7] a) N. Kihara, N. Hara, T. Endo, *J. Org. Chem.* **1993**, *58*, 6198; b) L. Guo, C. Wang, X. Luo, G. Cui, H. Li, *Chem. Commun.* **2010**, *46*, 5960; c) M. Aresta, A. Dibenedetto, *J. Mol. Catal. A.: Chem.* **2002**, *182-183*, 399.
- [8] a) J. J. Peng, Y. Q. Deng, *New J. Chem.* **2001**, *25*, 639; b) H. Yang, Y. Gu, Y. Deng, F. Shi, *Chem. Commun.* **2002**, 274; c) H. Kawanami, A. Sasaki, K. Matsui, Y. Ikushima, *Chem. Commun.* **2003**, 896; d) J. Sun, S. Fujita, M. Arai, *J. Organomet. Chem.* **2005**, *690*, 3490.
- [9] a) Y. Xie, Z. Zhang, T. Jiang, J. He, B. Han, T. Wu, K. L. Ding, *Angew. Chem. Int. Ed.* **2007**, *46*, 7255; b) Y. B. Xiong, H. Wang, R. M. Wang, Y. F. Yan, B. Zheng, Y. P. Wang, *Chem. Commun.* **2010**, *46*, 3399.
- [10] a) W. J. Kruper, D. V. Dellar, *J. Org. Chem.* **1995**, *60*, 725; b) F. W. Li, C. G. Xia, L. W. Xu, W. Sun, G. X. Chen, *Chem. Commun.* **2003**, 2042; c) W. Clegg, R. W. Harrington, M. North, R. Pasquale, *Chem.–Eur. J.* **2010**, *16*, 6828; d) R. L. Paddock, S. T. Nguyen, *Chem. Commun.* **2004**, 1622.
- [11] M. L. Man, K. C. Lam, W. N. Sit, S. M. Ng, Z. Zhou, Z. Lin, C. P. Lau, *Chem. Eur. J.* **2006**, *12*, 1004.
- [12] a) H. Sun, D. Zhang, *J. Phys. Chem. A.* **2007**, *111*, 8036; b) Y. Ren, T. T. Meng, J. Jia, H. S. Wu, *Comput. Theor. Chem.* **2011**, *978*, 47; c) Z.-Z. Yang, Y.-N. Zhao, L.-N. He, J. Gao, Z.-S. Yin, *Green Chem.* **2012**, *14*, 519; d) R. A. Watile, D. B. Bagal, K. M. Deshmukh, K. P. Dhake, B. M. Bhanage, *J. Mol. Catal. A: Chem.* **2011**, 351, 196; e) Z.-Z. Yang, L.-N. He, C.-X. Miao, S. Chanfreau, *Adv. Synth. Catal.* **2010**, *352*, 2233.
- [13] M. J. Ajitha, C. H. Suresh, *Tetrahedron Lett.* **2011**, *52*, 5403.
- [14] F. Chen, X. Li, B. Wang, T. Xu, S. L. Chen, P. Liu, C. Hu, *Chem. Eur. J.* **2012**, *18*, 9870.
- [15] J.-Q. Wang, J. Sun, W.-G. Cheng, K. Dong, X.-P. Zhang, S.-J. Zhang, *Phys. Chem. Chem. Phys.* **2012**, *14*, 11021.
- [16] K. Roshith Roshan, G. Mathai, J. Kim, J. Tharun, G.-A. Park, D.-W. Park, *Green Chem.* **2012**, *14*, 2933.
- [17] J.-Q. Wang, K. Dong, W.-G. Cheng, J. Sun, S. J. Zhang, *Catal. Sci. Technol.* **2012**, *2*, 1480.
- [18] J. Ma, J. Liu, Z. Zhang, B. Han, *Green Chem.* **2012**, *14*, 2410.

- [19] a) A. Decortes, M. Martínez Belmonte, J. Benet-Buchholz, A. W. Kleij *Chem. Commun.* **2010**, 46, 4580; b) A. Decortes, A. W. Kleij, *ChemCatChem* **2011**, 3, 831.
- [20] M. Taherimehr, A. Decortes, S. M. Al-Amsyar, W. Lueangchaichaweng, C. J. Whiteoak, E. C. Escudero-Adàn, A. W. Kleij, P. P. Pescarmona, *Catal. Sci. Technol.* **2012**, 2, 2231.
- [21] a) A. Decortes, A. M. Castilla, A. W. Kleij, *Angew. Chem. Int. Ed.* **2010**, 49, 9822. For some other reviews see: b) P. P. Pescarmona, M. Taherimehr, *Catal. Sci. Technol.* **2012**, 2, 2169; c) M. North, R. Pasquale, C. Young, *Green Chem.* **2010**, 12, 1514. For a computational review on CO₂ conversion see: d) M. Drees, M. Cokoja, F. E. Kühn, *ChemCatChem* **2012**, 4, 1703.
- [22] L. Cuesta-Aluja, M. Djoufak, A. Aghmiz, R. Rivas, L. Christ, A. M. Masdeu-Bultó, *J. Mol. Catal. A: Chem.* **2014**, 381, 161.
- [23] L. Karamé, M. L. Tommasino, R. Faure, M. Lemaire, *Eur. J. Org. Chem.* **2003**, 7, 1271.
- [24] M. North, R. Pasquale, *Angew. Chem. Int. Ed.* **2009**, 48, 2946.
- [25] a) ADF2010, SCM, Theoretical Chemistry, Vrije Universiteit, Amsterdam, The Netherlands, <http://www.scm.com>; E.J. Baerends, T. Ziegler, J. Autschbach, D. Bashford, A. Bérces, F.M. Bickelhaupt, C. Bo, P.M. Boerrigter, L. Cavallo, D.P. Chong, L. Deng, R.M. Dickson, D.E. Ellis, M. van Faassen, L. Fan, T.H. Fischer, C. Fonseca Guerra, A. Ghysels, A. Giammona, S.J.A. van Gisbergen, A.W. Götz, J.A. Groeneveld, O.V. Gritsenko, M. Grüning, S. Gusarov, F.E. Harris, P. van den Hoek, C.R. Jacob, H. Jacobsen, L. Jensen, J.W. Kaminski, G. van Kessel, F. Kootstra, A. Kovalenko, M.V. Krykunov, E. van Lenthe, D.A. McCormack, A. Michalak, M. Mitoraj, J. Neugebauer, V.P. Nicu, L. Noodleman, V.P. Osinga, S. Patchkovskii, P.H.T. Philipsen, D. Post, C.C. Pye, W. Ravenek, J.I. Rodríguez, P. Ros, P.R.T. Schipper, G. Schreckenbach, J.S. Seldenthuis, M. Seth, J.G. Snijders, M. Solà, M. Swart, D. Swerhone, G. te Velde, P. Vernooijs, L. Versluis, L. Visscher, O. Visser, F. Wang, T.A. Wesolowski, E.M. van Wezenbeek, G. Wiesenekker, S.K. Wolff, T.K. Woo, A.L. Yakovlev; b) G. te Velde, F. M. Bickelhaupt, E. J. Baerends, C. Fonseca Guerra, S. J. A. van Gisbergen, J. G. Snijders, T. Ziegler, *J. Comput. Chem.* **2001**, 22, 931.

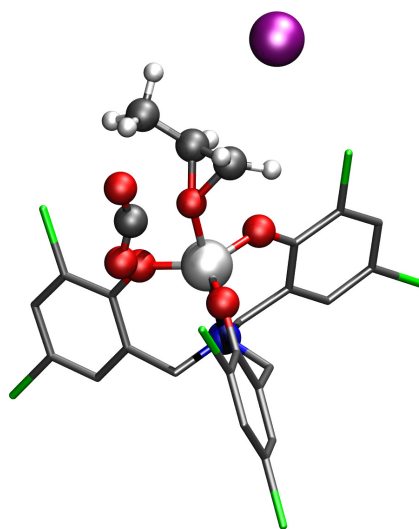
- [26] A. D. Becke, *Phys. Rev. A* **1988**, *38*, 3098.
- [27] a) J. P. Perdew, *Phys. Rev. B* **1986**, *33*, 8822; b) J. P. Perdew, *Phys. Rev. B* **1986**, *34*, 7406.
- [28] a) E. van Lenthe, E. J. Baerends, J. G. Snijders, *J. Chem. Phys.* **1993**, *99*, 4597; b) E. van Lenthe, E. J. Baerends, J. G. Snijders, *J. Chem. Phys.* **1994**, *101*, 9783.
- [29] *Atkins' Physical Chemistry*, Eds. P. Atkins, J. de Paula, 8th edition, Oxford University Press, Oxford UK **2006**, pp. 108-109.
- [30] A. Klamt, *J. Phys. Chem.* **1995**, *99*, 2224.
- [31] Gaussian, Revision A.02, M. J. Frisch, G. W. Trucks, H. B. Schlegel, G. E. Scuseria, M. A. Robb, J. R. Cheeseman, G. Scalmani, V. Barone, B. Mennucci, G. A. Petersson, H. Nakatsuji, M. Caricato, X. Li, H. P. Hratchian, A. F. Izmaylov, J. Bloino, G. Zheng, J. L. Sonnenberg, M. Hada, M. Ehara, K. Toyota, R. Fukuda, J. Hasegawa, M. Ishida, T. Nakajima, Y. Honda, O. Kitao, H. Nakai, T. Vreven, J. A. Montgomery, Jr., J. E. Peralta, F. Ogliaro, M. Bearpark, J. J. Heyd, E. Brothers, K. N. Kudin, V. N. Staroverov, R. Kobayashi, J. Normand, K. Raghavachari, A. Rendell, J. C. Burant, S. S. Iyengar, J. Tomasi, M. Cossi, N. Rega, N. J. Millam, M. Klene, J. E. Knox, J. B. Cross, V. Bakken, C. Adamo, J. Jaramillo, R. Gomperts, R. E. Stratmann, O. Yazyev, A. J. Austin, R. Cammi, C. Pomelli, J. W. Ochterski, R. L. Martin, K. Morokuma, V. G. Zakrzewski, G. A. Voth, P. Salvador, J. J. Dannenberg, S. Dapprich, A. D. Daniels, Ö. Farkas, J. B. Foresman, J. V. Ortiz, J. Cioslowski, D. J. Fox, **2009**, Gaussian, Inc., Wallingford CT.
- [32] D. Tian, B. Liu, Q. Gan, H. Li, D. J. Darensbourg, *ACS Catal.* **2012**, *2*, 2029. See also reference 24.
- [33] F. Jutz, J.-D. Grunwaldt, A. Baiker, *J. Mol. Catal. A: Chem.* **2008**, *279*, 94.
- [34] X.-B. Lu, B. Liang, Y.-J. Zhang, Y.-Z. Tian, Y.-M. Wang, C.-X. Bai, H. Wang, R. Zhang, *J. Am. Chem. Soc.* **2004**, *126*, 3732.
- [35] D. J. Darensbourg, A. I. Moncada, W. Choi, J. H. Reibenspies, *J. Am. Chem. Soc.* **2008**, *130*, 6523.
- [36] S. J. Wezenberg, G. A. Metselaar, E. C. Escudero-Adán, J. Benet-Buchholz, A. W. Kleij, *Inorg. Chim. Acta* **2009**, *362*, 1053.

- [37] For illustrative examples see: a) R. M. Haak, A. Decortes, E. C. Escudero-Adán, M. Martínez Belmonte, E. Martín, J. Benet-Buchholz, A. W. Kleij, *Inorg. Chem.* **2011**, *50*, 7934; b) J. A. A. W. Elemans, S. J. Wezenberg, E. C. Escudero-Adán, J. Benet-Buchholz, D. den Boer, M. J. J. Coenen, S. Speller, A. W. Kleij, S. De Feyter, *Chem. Commun.* **2010**, *46*, 2548; c) E. C. Escudero-Adán, J. Benet-Buchholz, A. W. Kleij, *Chem.–Eur. J.* **2009**, *15*, 4233; d) S. J. Wezenberg, E. C. Escudero-Adán, J. Benet-Buchholz, A. W. Kleij, *Chem.–Eur. J.* **2009**, *15*, 5695; e) E. C. Escudero-Adán, J. Benet-Buchholz, A. W. Kleij, *Eur. J. Inorg. Chem.* **2009**, *15*, 3562.
- [38] For some examples: a) A. L. Singer, D. A. Atwood, *Inorg. Chim. Acta* **1998**, *277*, 157; b) P.D. Frischmann, A. J. Gallant, J.H. Chong, M. J. MacLachlan, *Inorg. Chem.* **2008**, *47*, 101; c) M. Kuil, P. E. Goudriaan, A. W. Kleij, D. M. Tooke, A. L. Spek, P. W. N. M. van Leeuwen, J. N. H. Reek, *Dalton Trans.* **2007**, 2311. See also: d) C. J. Whiteoak, G. Salassa, A. W. Kleij, *Chem. Soc. Rev.* **2012**, *41*, 622.
- [39] E. C. Escudero-Adán, J. Benet-Buchholz, A. W. Kleij, *Inorg. Chem.* **2008**, *47*, 4256.
- [40] The high Lewis acidity is provoked by the rigid, planar coordination environment around the Zn metal center. See for applications: a) A. W. Kleij, D. M. Tooke, M. Kuil, M. Lutz, A. L. Spek, J. N. H. Reek, *Chem. Eur. J.* **2005**, *11*, 4743; b) S. J. Wezenberg, G. Salassa, E. C. Escudero-Adán, J. Benet-Buchholz, A. W. Kleij, *Angew. Chem. Int. Ed.* **2011**, *50*, 713; c) G. Salassa, M. J. J. Coenen, S. J. Wezenberg, B. L. M. Hendriksen, S. Speller, J. A. A. W. Elemans, A. W. Kleij, *J. Am. Chem. Soc.* **2012**, *134*, 7186. See also reference 38.
- [41] G.-P. Wu, S.-H. Wei, W.-M. Ren, X.-B. Lu, T.-Q. Xu, D. J. Darensbourg, *J. Am. Chem. Soc.* **2011**, *133*, 15191.
- [42] a) G.-P. Wu, S.-H. Wei, W.-M. Ren, X.-B. Lu, B. Li, Y.-P. Zua, D. J. Darensbourg, *Energy Environ. Sci.* **2011**, *4*, 5084; b) G.-P. Wu, S.-H. Wei, X.-B. Lu, W.-M. Ren, D. J. Darensbourg, *Macromolecules* **2010**, *43*, 9202.
- [43] a) C. J. Whiteoak, B. Gjoka, E. Martín, M. Martínez Belmonte, E. C. Escudero-Adán, C. Zonta, G. Licini, A. W. Kleij, *Inorg. Chem.* **2012**, *51*, 10639; b) E. C. Escudero-Adán, J. Benet-Buchholz, A. W. Kleij, *Eur. J. Inorg. Chem.* **2009**, 3562.
- [44] This study has not been published yet. A manuscript including both experimental and theoretical results is in preparation.

Chapter 5

A Highly Active Aluminium Catalyst for the Formation of Cyclic Carbonates from CO₂ and Epoxides

A detailed reaction mechanism for the catalytic formation of cyclic carbonates from CO₂ and epoxides, based on the [Al{amino-tris(phenolate)}]/NBu₄I binary system, has been investigated by using density functional theory (DFT) methods. A monometallic mechanism was envisaged and the main steps of the reaction have been described in detail. The energetic span model (δE) was used to theoretically determine the turnover frequencies (TOFs) of the catalytic cycles and thus evaluating the efficiency of the aluminium complex for mediating the CO₂ addition reaction. In addition to evaluate solvent effects, we also investigated the influence of the entropy changes in solution and the effect of parameterized and empirical dispersion corrections on the thermodynamics of the reaction. The resulting TOFs were found to be fully in line with the experimental results.



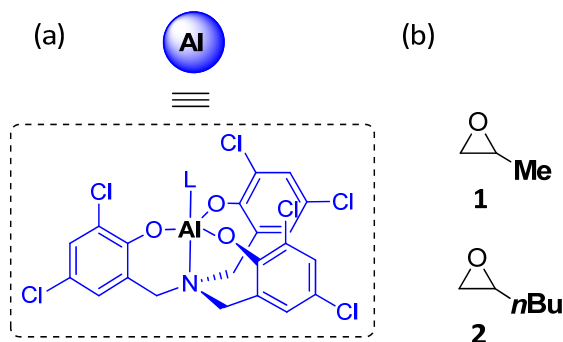
The study described in this chapter has been published: C. J. Whiteoak, N. Kielland, V. Laserna, F. Castro-Gómez, E. Martín, E. Escudero-Adán, C. Bo, A. W. Kleij, *Chem. Eur. J.* **2014**, *20*, 2264. A manuscript including entropic corrections in solution and evaluation of TOFs is in preparation: F. Castro-Gómez, W.M.C. Sameera, G. Nyman, A. W. Kleij, C. Bo, *in preparation*.

UNIVERSITAT ROVIRA I VIRGILI
THEORETICAL STUDIES ON TRANSITION METAL CATALYZED CARBON DIOXIDE FIXATION
Fernando Simón Castro Gómez

5.1 Introduction

As mentioned earlier in chapter 4, the fixation of CO₂ into epoxides to afford either organic polycarbonates or cyclic carbonates is a well-documented area of research. A widely number of different catalytic solutions have been proposed in order to mediate the reaction. Nonetheless, only in a limited amount of cases these catalytic efforts have resulted in systems with (very) high activity expressed in high turnover frequencies (TOFs) and high turnover numbers (TONs).

Kleij and coworkers recently reported on the pronounced activity and versatility of an Al^{III} complex containing amino-tris(phenolate) ligand scaffolds (Scheme 5.1a), in conjunction with NBU₄I as powerful binary catalysts for the addition of CO₂ to epoxides with initial activities among the highest reported so far in this area.^[1] From these previous studies using the [Al{amino-tris(phenolate)}]/NBU₄I binary system the authors demonstrated unprecedented activity (initial TOFs up to 36000 h⁻¹) and substrate scope.



Scheme 5.1 (a) Schematic drawing of the Al{amino-tris(phenolate)} catalyst; (b) substrates **1-2** used in this investigation.

Herein, it is reported the results of a computational study investigating the mechanism for the formation of cyclic carbonates from CO₂ and epoxides **1** and **2** (Scheme 5.1b) mediated by the [Al{amino-tris(phenolate)}]/NBU₄I binary system. We explore the catalytic cycle using density functional theory (DFT) methods and evaluate the influence of solvent, entropy changes in condensed phase, and the inclusion of dispersion-corrected functionals. In addition, the catalytic cycle is examined with the energetic span model (δE) developed by Kozuch and Shaik.^[2] This approach explains and predicts the efficiency of a catalyst in terms of its TOF on the basis of the transition state theory and fundamental rate

laws. For predicting TOFs the model takes the relative free energies of intermediates and transition states derived from the theoretically obtained energy profile. Extensive literature on the application of the energetic span model to heterogeneous^[3] and homogeneous^[4] catalysis has been reported at different level of depth. However, only few studies on the application of this approach for CO₂ addition reactions are currently available. Leitner and coworkers^[5] utilized the energetic span model to investigate the direct carboxylation of unactivated arene C–H bonds with CO₂ based on ruthenium(II) pincer complexes as catalysts of the reaction. Through catalyst screening and modification of some parameters, TOFs in the range of 105–107 h⁻¹ were predicted for the best systems. On the other hand, Ajitha and Suresh^[6] identified the smallest δE among six different pathways for the NHC-mediated CO₂ transformation reaction of epoxides affording cyclic carbonates.

In light of this, our study focuses on the quantitative analysis of the activity of the Al{amino-tris(phenolate)} catalyst as mediator of the formation of organic carbonates from CO₂ and epoxides. In order to reproduce experimental TOFs we take into account some critical factors like the solvation model employed for the calculations, changes of entropies in solution and the use of dispersion-corrected DFT methods, analyzing in detail how the previous parameters could affect the catalytic cycle and their direct relationship with the TOFs obtained with the energetic span model.

5.2 Motivation

Previous studies by Kleij and coworkers^[1] on the catalytic formation of cyclic carbonates from CO₂ and epoxides mediated by an Al^{III} complex containing amino-tris(phenolate) ligand scaffolds, in conjunction with NBu₄I, demonstrated that this binary system presents extraordinary activity, expressed in high turnover frequencies (initial TOFs up to 36000 h⁻¹).

Encouraged by these experimental results we turn our attention to the exploration of the mechanism operating for the aluminium catalyzed reaction, based on our previous findings for the Zn(salphen) catalyst.

Having experimental results on neat (solvent free) conditions, we also found fascinating the idea of being able to reproduce experimental TOFs of the reaction through theoretical

approaches such as the energetic span model by Kozuch and Shaik.^[2] Thus, in this chapter we will focus on a more quantitative evaluation of the performance of the catalytic cycle.

5.3 Objectives

One of the goals of this chapter is to theoretically explore the reaction mechanism for the addition of CO₂ into epoxides affording cyclic carbonates, based on [Al{amino-tris(phenolate)}]/NBu₄I binary system. We first focus on understanding the main steps of the reaction by identifying all the intermediates and transition state species, as well as the rate-determining barriers for the profile.

Secondly, we will evaluate the influence of using empirical dispersion on the accuracy of the thermodynamics of the CO₂ addition reaction.

Furthermore, free-energy profiles for the aluminium catalyzed reaction will be generated by applying standard state corrections to the entropy in solution.

For all the studied profiles, we will evaluate the efficiency of the reaction by calculating the theoretical TOFs.

5.4 Computational details

All calculations in this study were performed by using the Gaussian 09 package.^[7] The hybrid B3LYP functional,^[8] and also the M06-2X^[9] and ωB97XD^[10] dispersion-corrected functionals were employed. The standard 6-311G(d,p) basis set was used to describe the H, C, N and O atoms. The relativistic effective core pseudo potential LANL2DZ^[11] was used, together with its associated basis set, for Al, Cl and I atoms. Full geometry optimizations were performed without constrains. The nature of the stationary points encountered was characterized either as minima or transition states by means of harmonic vibrational frequencies analysis. Gibbs free energies were calculated at standard conditions (T=298.15 K, p=1 atm). In order to introduce solvent effects, single point calculations were performed on the gas-phase optimized structures by using the polarizable continuum model (PCM). Methyl ethyl ketone (MEK) was used as solvent model only for the first part of the results presented herein. Moreover, the dielectric constant (ε) of the polarizable medium was set to the value reported for the simplest epoxide, ethylene oxide (ε=12.42),^[12] as the reaction takes place in epoxide rich phase. The 1-hexanol solvent was

used for this purpose ($\epsilon=12.51$), as implemented in Gaussian. Since no standard approach at quantum mechanics level is available for accurate evaluation of entropy in solution, we adopted the following approaches: by neglecting the translational-entropy terms in the calculation of the entropy in solution,^[13] the approach proposed by Martin and coworkers,^[14] and the method described by Wertz^[15] and Cooper and Ziegler.^[16] The TOF values were calculated at 363.15 K (90°C) with the expressions of the energetic span model (δE), as implemented in the user-friendly AUTOF program.^[2, 17]

5.5 Results

5.5.1 The Al-catalyst/ NBu_4I catalyzed addition of CO_2 to propylene oxide

Considering a similar type of monometallic mechanism as described for the Zn(salphen) complex in previous chapter, we have further focused on some of the features of the operative mechanism when using the Al{amino-tris(phenolate)} complex as catalyst of the addition of CO_2 to propylene oxide **1** in MEK solution. The free-energy profile calculated for the β pathway (i.e., nucleophilic attack on the least substituted epoxide carbon) of the catalyzed reaction is shown in Figure 5.1.

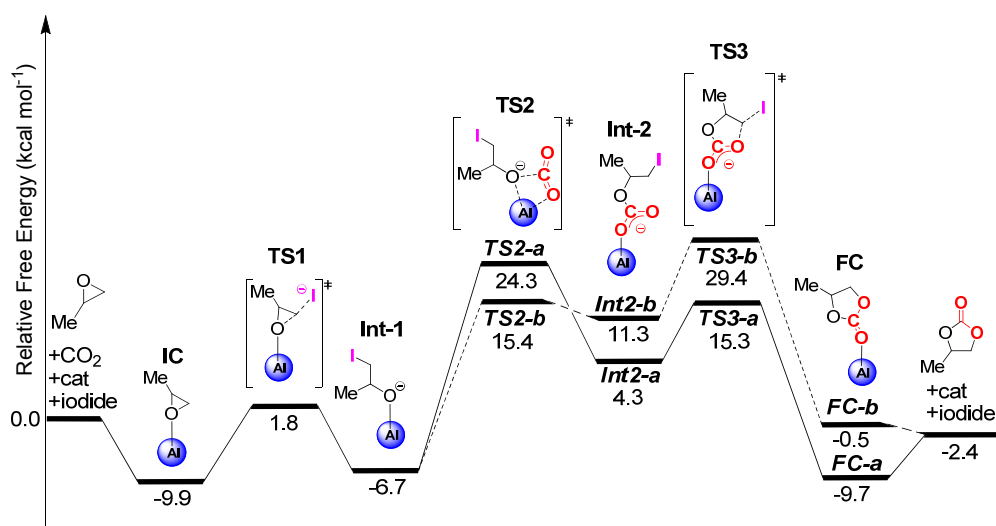


Figure 5.1 Free-energy profile for cyclic carbonate formation from CO_2 and propylene oxide **1** catalyzed by $[\text{Al}\{\text{amino-tris(phenolate)}\}]/\text{NBu}_4\text{I}$, calculated at the B3LYP level. MEK was used as solvent of the reaction at 25°C. IC stands for initial complex formation; FC stands for the final complex having the carbonate product coordinated.

The reaction starts with the coordination of the propylene oxide **1** with the aluminium catalyst, forming an initial complex **IC**. This complex is energetically more stable than the isolated reactants by 9.9 kcal·mol⁻¹, demonstrating that it is a powerful Lewis acid mediator that activates the epoxide for subsequent nucleophilic attack by the halide. The iodide mediates the ring-opening of the coordinated epoxide by nucleophilic attack on the β carbon of the substrate. This process involves the breaking of the C_β-O bond and the simultaneous formation of a C_β-I bond, through **TS1** (Figure 5.2), affording the metal-alkoxide intermediate **Int-1** with a total barrier of 11.7 kcal·mol⁻¹.

The next step is the insertion of the CO₂ molecule into the metal-oxygen bond of intermediate **Int-1**, leading to the formation of linear carbonate **Int-2** *via* the transition state **TS2** shown in Figure 5.2. This process involves two possible pathways, namely, the path-a and path-b depicted in Figure 5.1. Thus, two hexa-coordinated transition state structures (**TS2**) could be obtained depending on the relative orientation (cf., axial or equatorial coordination position of O1 in Figure 5.2) of the incoming CO₂ molecule with respect the metal centre, as shown in Figure 5.2. **TS2-b** would be the most favorable route due to the lower barrier required to afford **Int2-b** (with an energy difference of 8.9 kcal·mol⁻¹ compared to the pathway towards **Int2-a**). However, since axial-to-equatorial interconversion between intermediates **Int2-b** and **Int2-a** should be fairly easy, it is proposed that these species can undergo isomerization. Figure 5.3 shows that isomerization reaction proceeds *via* **TS-isom** and is characterized by decreasing of the angle O4-Al-O1 from 163° (**Int2-b**) to 96° (**Int2-a**), involving a relative barrier of 16.1 kcal mol⁻¹. Once the isomerization process takes place, the reaction should follow the path-a.

Along the reaction coordinate, the subsequent ring-closing occurs *via* the non-coordinating O-atom (O2) of the carbonate fragment (Figure 5.2) by means of concerted transition state **TS3**, giving the final complex **FC**. Similarly, transition states **TS3-a** and **TS3-b** also could afford intermediates **FC-a** and **FC-b**, respectively. Thus, path-a still continues being the most likely pathway because of the higher stability of **TS3-a** over **TS3-b** by 14.1 kcal·mol⁻¹. In addition, the isomerization reaction requires less energy than overcome **TS3-b** and obtain **FC-b** (by 13.3 kcal·mol⁻¹).

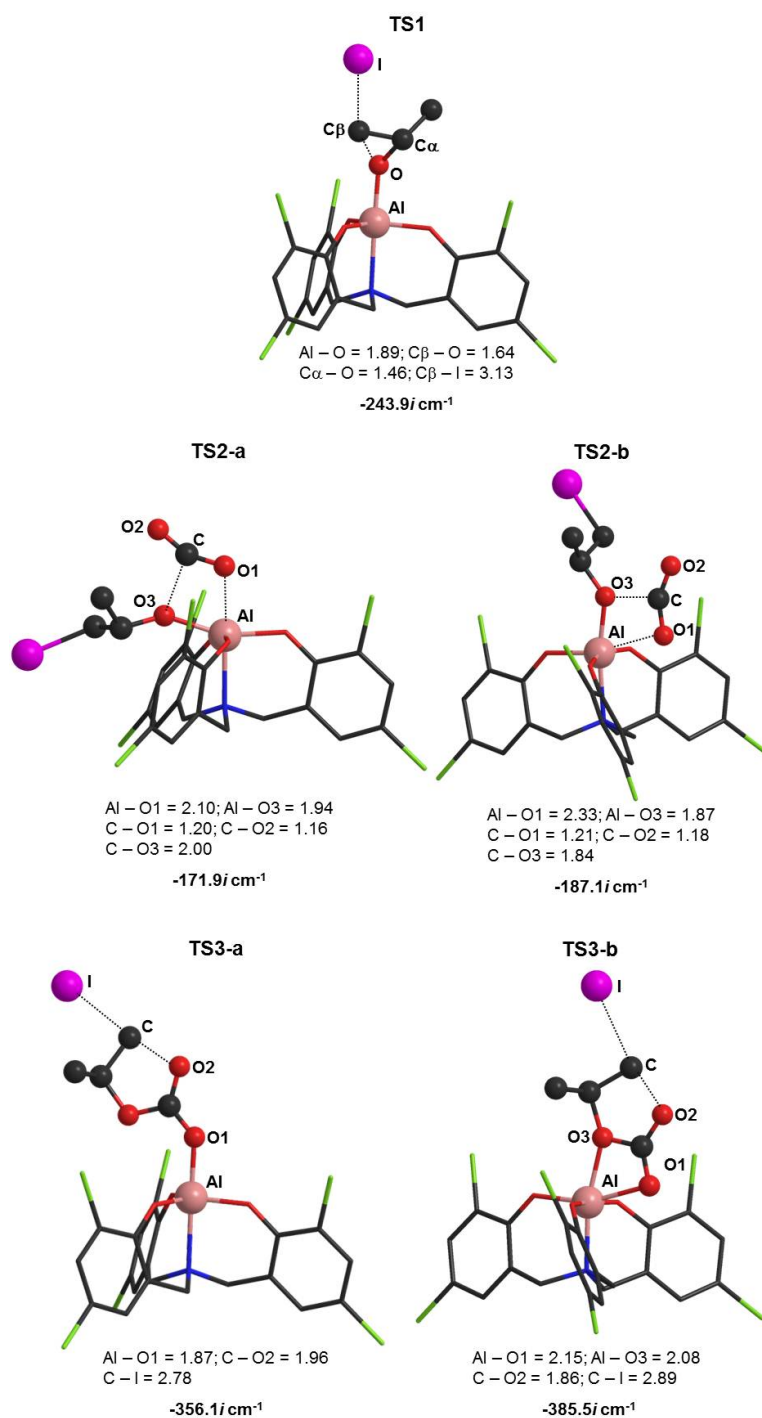


Figure 5.2 Optimized structures of the transition states **TS1–TS3** for the Al-complex/ NBu_4I catalyzed reaction, together with the most relevant calculated distances (in Å) and the values of the negative (imaginary) vibrational frequencies.

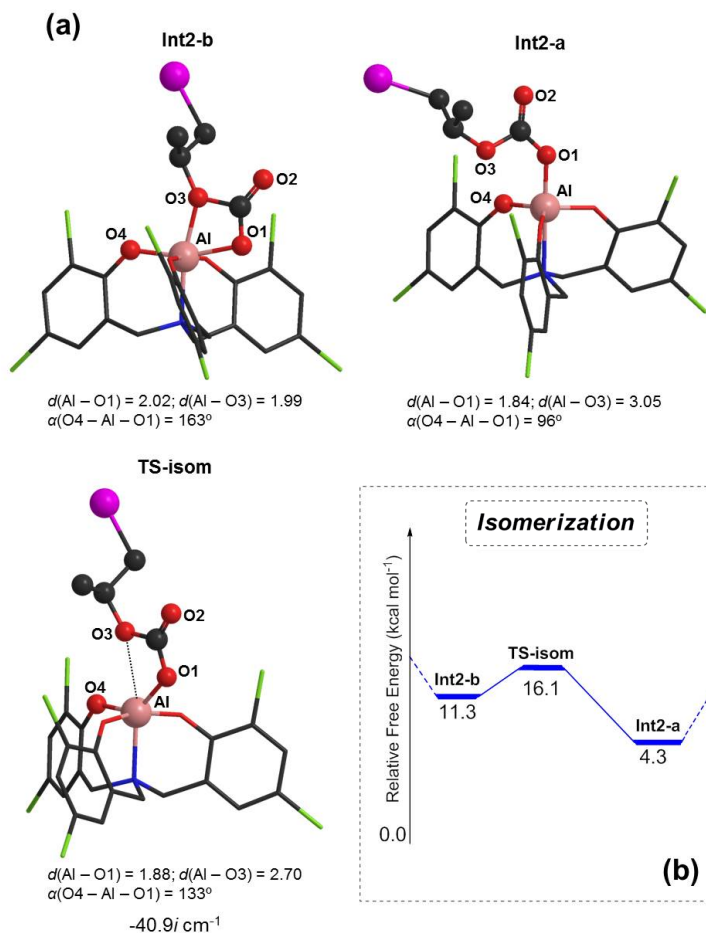


Figure 5.3 (a) Optimized structures of the intermediates **Int2-b** and **Int2-a** and transition state **TS-isom** involved in the isomerization, together with the most relevant calculated distances (in Å) and the values of the negative (imaginary) vibrational frequency; (b) Free-energy barrier for the isomerization process.

Path-a has an activation energy of 34.2 kcal·mol⁻¹ (calculated from the most stable intermediate, **IC**), with the CO₂ insertion being rate-limiting; whereas for path-b, a higher activation energy was obtained (39.3 kcal·mol⁻¹), with the ring-closing step (**TS3**) corresponding to the rate-limiting step. Once the coordinated cyclic carbonate is formed, it is released from **FC** allowing for further epoxide turnover. The overall reaction is exergonic with a release of 2.4 kcal·mol⁻¹.

Both pathways were examined by using the energetic span model (δE). Computed free-energy spans for path-a and path-b resulted fairly high by 34.2 and 39.3 kcal·mol⁻¹,

respectively. **IC** was found to be the TOF-determining intermediate (TDI) for both profiles, while **TS2-a** and **TS3-b** correspond to the TOF-determining TS (TDTS) of the alternative pathways. Calculating the turnover frequency (TOF) leads to values of $6.6 \times 10^5 \text{ h}^{-1}$ for path-a and $5.8 \times 10^8 \text{ h}^{-1}$ for path-b. The combination of both pathways (considering the most stable intermediates and transition state species, as well as the isomerization process) resulted in a smaller energetic span of $26.0 \text{ kcal}\cdot\text{mol}^{-1}$ and a TOF value of 3.3 h^{-1} . **IC** corresponds to the TDI and **TS-isom** to the TDTS. TOFs calculated so far either for the individually or combined profiles are much lower than that obtained experimentally (depending on reactants and catalyst system concentrations, $9.6 \times 10^2 \text{ h}^{-1}$ is the lowest value measured in the optimization studies of the activity of Al-catalyst, and $2.6 \times 10^4 \text{ h}^{-1}$ the highest value obtained in the stability studies using the Al-catalyst). As expected, a significant improvement in the TOF value was observed when considering the combined pathways.

It should be noted that the catalyzed CO_2 addition reaction was carried out experimentally under neat conditions (i.e., the reaction took place in epoxide rich phase), employing 1,2-epoxyhexane **2** as reactant (see Scheme 5.1b, page 109). Thus, further calculations were performed in order to study the mechanism at such conditions. These results are discussed in next section.

5.5.2 The Al-catalyst/ NBu_4I catalyzed addition of CO_2 to 1,2-epoxyhexane

A free-energy profile for the combined path-a and path-b was obtained for the aluminium catalyzed formation of cyclic carbonates from CO_2 and 1,2-epoxyhexane **2** acting as substrate and solvent model. As shown in Figure 5.4, the resulting relative barriers show the same trend as the profile established for the reaction involving propylene oxide **1** and MEK (see Figure 5.1). As usual, the reaction starts with exothermic coordination of the epoxide (by $8.9 \text{ kcal}\cdot\text{mol}^{-1}$) forming the initial complex **IC**. Then the epoxide ring-opening is mediated by iodide attack on the less substituted carbon of the substrate **2**, affording the metal-alkoxide intermediate **Int-1**, and comprising a total barrier of $10.6 \text{ kcal}\cdot\text{mol}^{-1}$. This is the least energetically demanding step of the catalytic reaction.

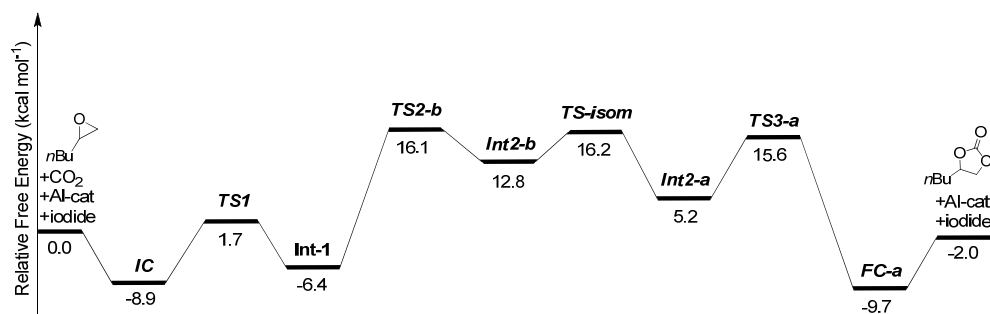


Figure 5.4 Free-energy profile for cyclic carbonate formation from CO₂ and 1,2-epoxyhexane **2** catalyzed by [Al{amino-tris(phenolate)}]/NBu₄, calculated at the B3LYP level. 1-hexanol was used as solvent of the reaction at 25°C. **IC** stands for initial complex formation; **FC-a** stands for the final complex having the carbonate product coordinated.

Next, the incoming CO₂ is inserted into **Int-1**, leading to formation of the hexacoordinated intermediate **Int2-b**. This process is achieved *via* **TS2-b** and requires a relative energy of 16.1 kcal·mol⁻¹; whereas the isomerization between **Int2-b** and **Int2-a** involves a similar barrier of 16.2 kcal·mol⁻¹. It is worth noting that the insertion of CO₂ and the isomerization reaction have closer activation energies (25.0 and 25.1 kcal·mol⁻¹, respectively), therefore, combination of both steps is considered rate-determining. The overall reaction is slightly exergonic, with a release of $\Delta G_r = -2.0$ kcal·mol⁻¹.

The resulting catalytic profile was examined with the energetic span model (δE). The computed free-energy span was found to be 25.1 kcal·mol⁻¹, which is indeed the activation energy of the isomerization. The initial complex (**IC**) corresponds the TOF-determining intermediate (TDI) of the reaction. Nevertheless, the exact position of the TOF-determining TS (TDTS) is not easy to determine owing to the small energy difference existing between **TS2-b** (16.1 kcal·mol⁻¹) and **TS-isom** (16.2 kcal·mol⁻¹). Thus, a similar degree of TOF control of 0.38 and 0.43 was observed for **TS2** and **TS-isom**, respectively. The calculation of TOF affords a value of 7.12 h⁻¹, which is 3.82 h⁻¹ larger than the value obtained with the substrate **1** and MEK (3.3 h⁻¹), but still lies out of the experimental results (9.6 x 10² - 2.6 x 10⁴ h⁻¹).

Since there is a close relationship between the calculated TOF and the obtained free energies, the above results encouraged us to take into account additional factors that have markedly influence on the free-energy barriers, such as the use of DFT methods including dispersion forces and/or the evaluation of entropic effects in solution.

5.5.3 Evaluation of dispersion corrections on the Al-catalyzed reaction

In the previous discussion, we have described the mechanism for the catalyzed CO₂ addition reaction without considering any kind of dispersion interactions for computing the free-energy profiles. The use of state-of-art DFT methods including these kind of interactions is currently indispensable in order to reach the so-called chemical accuracy.^[18] Indeed, the inclusion of dispersion has a markedly influence in the accuracy of the theoretical reaction thermodynamics.

In light of this, two different functionals (M06-2X and ω B97XD) were used for calculating the pathways of the Al-catalyzed reaction involving 1,2-epoxyhexane **2**, as shown in Figure 5.5. It should be noted that the use of dispersion significantly reduces the value of the relative free energies calculated with both dispersion-corrected DFT methods compared to those obtained at the B3LYP level (see Figure 5.4).

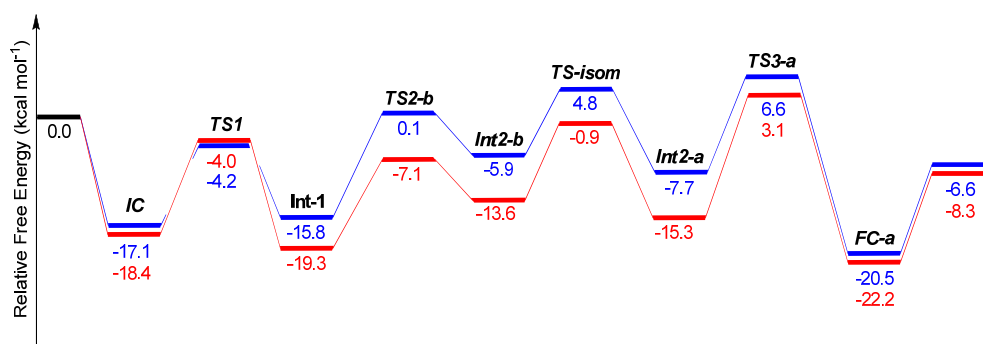


Figure 5.5 Free-energy profile for cyclic carbonate formation from CO₂ and 1,2-epoxyhexane **2** catalyzed by [Al{amino-tris(phenolate)}]/NBu₄I, calculated at the ω B97XD level (in blue) and M06-2X level (in red). 1-hexanol was used as solvent of the reaction at 25°C. **IC** stands for initial complex formation; **FC-a** stands for the intermediate complex having the carbonate product coordinated.

Unlike for the B3LYP pathway (see Figure 5.4), employing dispersion-corrected functionals the initial complexes **IC** are more exothermic by almost 9.0 kcal·mol⁻¹ (**IC**_{B3LYP} = -8.9 kcal·mol⁻¹). Afterwards, the absolute barrier for the ring-opening step was found to be 21.3 kcal·mol⁻¹ using ω B97XD, and 22.4 kcal·mol⁻¹ with M06-2X. These values are slightly higher than the corresponding step for the B3LYP profile by 2.3 kcal·mol⁻¹ and 3.8 kcal·mol⁻¹, respectively.

On the other hand, using dispersion, the insertion of CO₂ into the intermediate **Int-1** is favored by 10.3 kcal·mol⁻¹ for the M06-2X pathway; whereas with the ωB97XD, this energy difference is of 6.6 kcal·mol⁻¹ (total barrier **TS2**_{B3LYP}= 22.5 kcal·mol⁻¹). Isomerization between intermediates **Int2-b** and **Int2-a** involves a total energy of 10.7 kcal·mol⁻¹ at the ωB97XD level and 12.7 kcal·mol⁻¹ with M06-2X, which in turn, are higher in energy than that obtained with B3LYP by 7.3 kcal·mol⁻¹ and 9.3 kcal·mol⁻¹, respectively (**TS-isom**_{B3LYP}= 3.4 kcal·mol⁻¹).

The ring-closing reaction is rate-determining for both catalytic profiles. Thus, an activation barrier of 23.7 kcal·mol⁻¹ (calculated from **IC**) was found using the ωB97XD functional, while for the M06-2X profile, this energy is of 22.4 kcal·mol⁻¹ (calculated from **Int-1**). The overall reaction for both profiles is more exergonic ($\Delta G_r = -6.6$ kcal·mol⁻¹ for ωB97XD, and $\Delta G_r = -8.3$ kcal·mol⁻¹ for M06-2X) than the driving force obtained at the B3LYP level ($\Delta G_r = -2.0$ kcal·mol⁻¹).

In regards to the application of the energetic span model, slightly smaller δE were achieved using the dispersion-corrected functionals by 23.7 kcal·mol⁻¹ with ωB97XD and 22.4 kcal·mol⁻¹ with M06-2X. These values also correspond to the activation barrier of each profile. Furthermore, **TS3** was identified as the TDTS in both cases, whereas **IC** corresponds to the TDI for the ωB97XD catalytic cycle and **Int-1** for the M06-2X one. TOF values of 1.17×10^2 and 6.95×10^2 h⁻¹ were calculated for the ωB97XD and M06-2X profiles, respectively. Thus, a remarkable increment of two orders of magnitude is observed regarding the value calculated for the B3LYP pathway (TOF=7.12 h⁻¹). These data are in the same order of magnitude to the lowest TOF value measured in the experiments (9.6×10^2 h⁻¹), especially with the M06-2X pathway. The above results confirm that the use of dispersion is crucial to simulate catalytic systems more accurately, as stated.

5.5.4 Standard state corrections to the entropy in solution for the Al-catalyzed reaction

Solutions and solute-solvent interactions play an important role in homogeneous catalysis.^[19] As discussed in Section 2.6.2 of Chapter 2, one issue that has received much attention is the loss of translational entropy associated with the formation of a supramolecular complex when two molecules in solution interact. Thus, an overestimation of the translational entropy contributions in solution can be presented. Some approaches

for including entropy corrections have been reviewed in the same Chapter (Section 2.6.2). The most simple of these methods is by counting only the vibrational and rotational terms in the calculation of the total entropy in solution, i.e., just neglecting the translational entropy terms from the calculation of the gas-phase total entropy.^[13] The other two approaches employed herein are based on the fact that the equations used for calculating the thermodynamics of the reactions are applicable to a hypothetical ideal gas at concentrations (1/24.5 M) equivalent to standard state $P=1$ atm and $T=298.15$ K. However, in real experiments we do not have solutions whose concentration is 1/24.5 M, and therefore it is necessary to obtain results applicable at the concentration of the system studied. In light of this, Martin^[14] and Wertz^[15] and Ziegler^[16] introduced some empirical methods in order to successfully correct such overestimation to the entropy in solution.

Taking into account the above methodologies, we introduced the entropy corrections to all the free energy values obtained for the Al-catalyst/NBu₄I catalyzed addition of CO₂ into 1,2-epoxyhexane, using the different B3LYP, ωB97XD and M06-2X functionals. Results are shown in Figure 5.6.

Entropic corrections by considering only the vibrational and rotational contributions to the total entropy in solution lead to underestimation of the relative free energies (Figure 5.6). For the B3LYP profile (dashed black line), the barrier for the epoxide ring-opening (**TS1**) is lower than the formation of the initial complex (**IC**). The combination of the CO₂ insertion and isomerization reactions is rate-determining, with activation barrier (calculated from **Int-1**) of 11.5 kcal·mol⁻¹. In order to apply the energetic span model δE , all the barriers involved in a catalytic profile have to be above the reactants and products. This condition is not satisfied by the B3LYP pathway and hence, a TOF value for this profile was unable to evaluate.

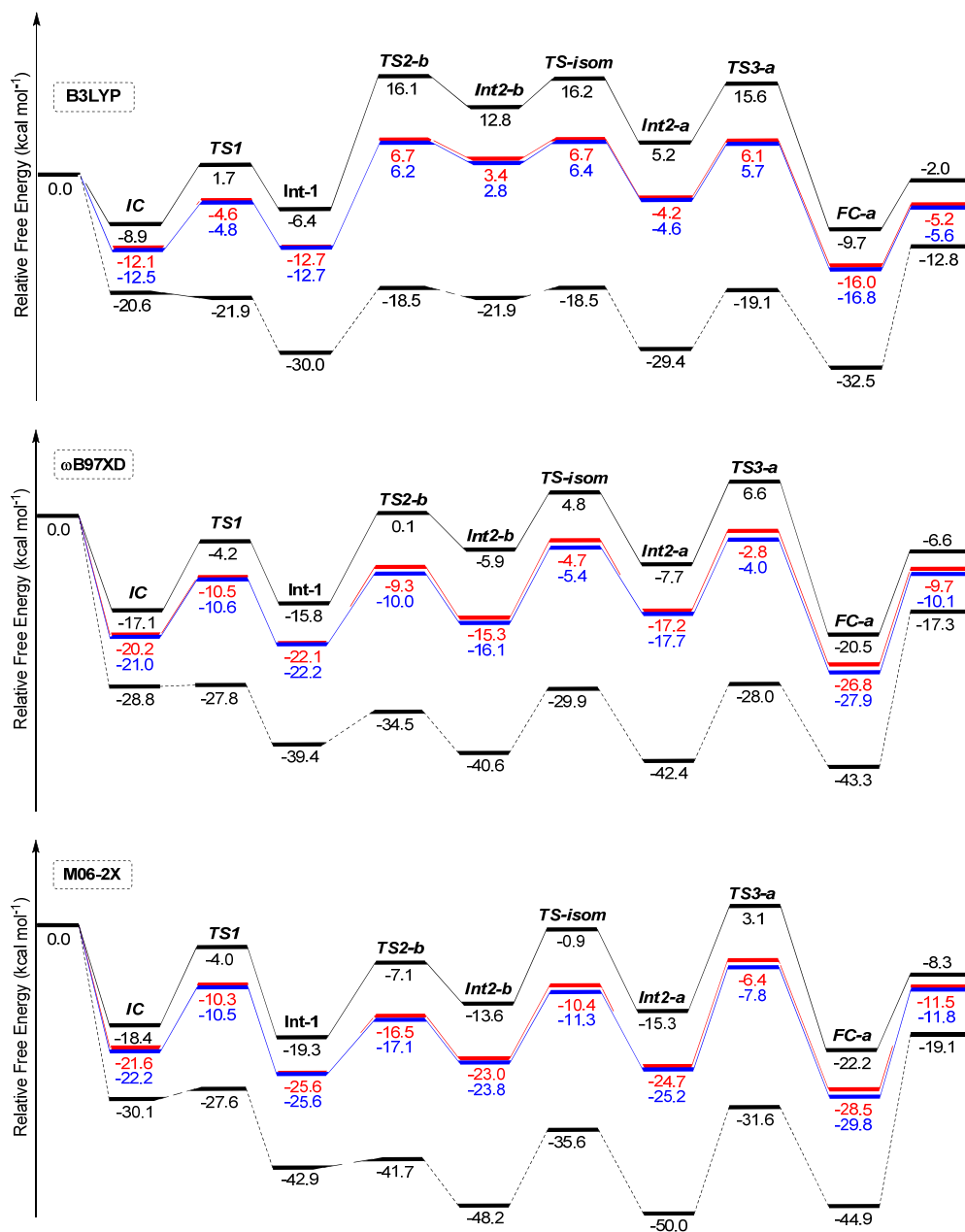


Figure 5.6 Free-energy profiles for cyclic carbonate formation from CO₂ and 1,2-epoxyhexane **2** catalyzed by [Al{amino-tris(phenolate)}]/NBu₄I, calculated at different levels. The solid black line represents the pathway without considering any kind of corrections for entropy in solution, whereas the dashed black line stands for the pathway including only the vibrational and rotational terms in the calculation of the total entropy in solution. The pathways considering entropy corrections by Martin, and Wertz/Ziegler appear in red and blue, respectively.

In contrast, for the ω B97XD and M06-2X pathways, the application of the energetic span leads to high span energies of 26.0 and 30.9 kcal·mol⁻¹, respectively (Table 5.1). Consequently, a decrease in the TOF values can be observed for both profiles (2.33 h⁻¹ with ω B97XD and 3.2 x 10⁻³ h⁻¹ with M06-2X, according to Table 5.1) compared with the value obtained without using any kind of entropic corrections (1.17 x 10² and 6.95 x 10² for ω B97XD and M06-2X, respectively). TOF-determining species were unable to determine for both profiles. These results suggest that some caution may be needed by neglecting the translational contributions for the calculation of total entropies in solution.

Table 5.1 TOFs, energetic spans, and TOF-determining species for the Al-catalyzed formation of cyclic carbonate from CO₂ and 1,2-epoxyhexane. S_v+S_r stands for the entropic corrections by neglecting the translational contributions; M, for Martin corrections; and W/Z, for Wertz and Ziegler corrections.

Entropic corrections	δE (kcal·mol ⁻¹)	TOF (h ⁻¹)	TDI	TDTS
B3LYP_none	25.1	7.12	IC	TS2-b/TS-isom
B3LYP_S _v +S _r	-	-	-	-
B3LYP_M	19.4	1.6 x 10 ⁴	Int-1	TS2-b/TS-isom
B3LYP_W/Z	19.1	2.2 x 10 ⁴	Int-1	TS-isom
ω B97XD_none	23.7	1.17 x 10 ²	IC	TS3-a
ω B97XD_S _v +S _r	26.0	2.33	-	-
ω B97XD_M	19.3	5.3 x 10 ⁴	Int-1	TS3-a
ω B97XD_W/Z	13.8	1.2 x 10 ⁵	Int-1/FC-a	TS3-a
M06-2X_none	22.4	6.95 x 10 ²	Int-1	TS3-a
M06-2X_S _v +S _r	30.9	3.2 x 10 ⁻³	-	-
M06-2X_M	19.2	5.3 x 10 ⁴	Int-1	TS3-a
M06-2X_W/Z	10.2	1.2 x 10 ⁵	FC-a	TS3-a

Exp. TOF = 9.6 x 10² h⁻¹ (lowest value measured in the optimization studies of the activity of Al-catalyst) and 2.6 x 10⁴ h⁻¹ (highest value obtained in the stability studies using the Al-catalyst) depending on reactants and catalyst system concentrations.

Now let us turn our attention to the application the approach by Martin and coworkers. According to our findings, a correction of approximately 3.16 kcal·mol⁻¹ applies to per component change for the reaction at 298.15 K and 1 atm, i.e., from *m*- to *n*- components, the reaction has an additional correction of (n - m) x 3.16 kcal·mol⁻¹. The Al-catalyzed addition of CO₂ into 1,2-epoxyhexane involves multicomponent change to form the corresponding cyclic carbonate product; the overall reaction is from four components (Al-

catalyst + I⁻ + CO₂ + 1,2-epoxyhexane) to three components (Al-catalyst + I⁻ + cyclic carbonate). In the formation of the initial complex (**IC**), there is a change from four to three components, therefore entropy overestimation of $-3.16 \text{ kcal}\cdot\text{mol}^{-1}$ ($(3 - 4) \times 3.16$) must be taken into account. In the case of the epoxide ring-opening (**TS1**) and the formation of the coordinated cyclic carbonate (**FC**), this correction is of $-6.32 \text{ kcal}\cdot\text{mol}^{-1}$ ($(2 - 4) \times 3.16$); whereas for the CO₂ insertion (**TS2-b**), isomerization (**TS-isom**) and ring-closing (**TS3-a**) reactions, a correction factor of $-9.48 \text{ kcal}\cdot\text{mol}^{-1}$ ($(1 - 4) \times 3.16$) is needed.

According to Table 5.1, an energy span of $19.4 \text{ kcal}\cdot\text{mol}^{-1}$ was found by applying the energetic span model on the B3LYP profile, affording a TOF of $1.6 \times 10^4 \text{ h}^{-1}$. This latter is in the same order of magnitude to the highest experimental value, as shown in Table 5.1. The TOF-determining intermediate (TDI) corresponds to **Int-1**. Although, **TS2-b** and **TS-isom**, having identical relative free energy ($6.7 \text{ kcal}\cdot\text{mol}^{-1}$), were found to be the TDTS with degrees of TOF control of 0.41. The TOFs calculated for the ωB97XD and M06-2X pathways using the Martin corrections have the same value of $5.3 \times 10^4 \text{ h}^{-1}$. In both cases, **Int-1** and **TS3-a** species are the TDI and TDTS, respectively. It should be emphasized that the resulting TOF lies in the same order of magnitude as the optimal value in the experiments.

In regards to the use of entropic corrections by Wertz and Ziegler, we could not establish an exact factor for correcting the entropy overestimation. This may be because the current approach considers many more experimental data (namely, the density of solvent and the gas-phase/liquid entropies, see Section 2.6.2 of Chapter 2) than that used by the Martin method (it involves only the density of solvent) for generating standard state corrections. However, according to the free-energy values obtained with the Wertz and Ziegler method (see blue profiles in Figure 5.6), such additional correction factor should be in range between 3.3 and $3.9 \text{ kcal}\cdot\text{mol}^{-1}$. Thus, for instance, with the B3LYP profile the rate-determining step (**TS-isom**, with activation barrier of $19.1 \text{ kcal}\cdot\text{mol}^{-1}$) comprises a correction of $-9.8 \text{ kcal}\cdot\text{mol}^{-1}$ which is approximately calculated from $(1 - 4) \times 3.26$. The same methodology could be applied for the remaining steps of the different pathways. Interestingly, the use of this method (cf. W/Z in Table 5.1) in order to correct the B3LYP free energies, leads to TOF of 2.2×10^4 that is fully in agreement with the highest value obtained in the stability studies using the Al-catalyst. Both TDTS and TDI are accurately defined and correspond to **TS-isom** and **Int-1**, respectively.

The lowest energetic spans were found for the ω B97XD (13.8 kcal·mol⁻¹) and M06-2X (10.2 kcal·mol⁻¹) profiles, leading to a high TOF of 1.2×10^5 h⁻¹. This exceeds the highest value obtained experimentally by one order of magnitude. Because of the equal degree of control of 0.46 obtained for **Int-1** and **FC** with the ω B97XD pathway, the exact position of the TDI cannot be determined; whereas **TS3-a**, corresponds to the TDTS. For the M06-2X profile, the TDTS and TDI are given by the **TS3-a** and **FC-a** species, respectively.

Bearing the results of this section in mind, we could conclude that the correction of the entropic contributions in solution plays an important role towards quantitative evaluation of the activity shown by the Al-catalyst for cyclic carbonate formation from CO₂ and epoxides.

5.6 Conclusions

The mechanism for the catalytic formation of cyclic carbonate products from CO₂ and epoxides based on the binary [Al{amino-tris(phenolate)}]/NBu₄I catalyst system has been investigated and elucidated in detail by DFT methods.

Four main steps were described for the Al-catalyzed CO₂ addition reaction, namely, the epoxide ring-opening, the insertion of CO₂, the isomerization reaction and the ring-closing process.

The reaction could follow two possible routes (path-a and path-b) depending on the coordination (axial or equatorial) of one oxygen atom from the incoming CO₂ to the Lewis acidic center of the complex. A markedly preference for path-a is envisaged once overcome the axial-to-equatorial interconversion of the hexacoordinated linear carbonate intermediate (isomerization reaction).

The combination of isomerization and the ring-closing reactions have been found to be rate-determining for the reaction involving either the propylene oxide or 1,2-epoxyhexane substrates at the B3LYP level. Small TOFs are calculated for both profiles.

The use of dispersion through the M06-2X and ωB97XD methods significantly reduced the values of the relative free energies in comparison to those obtained at the B3LYP level. The ring-closing reaction is rate-determining for both catalytic profiles.

Compared with the B3LYP pathway, a remarkable increment of two orders of magnitude was observed for the M06-2X and ωB97XD profiles, which is in agreement with the experimental TOF measured in the optimization studies of the activity of Al-catalyst.

Entropic corrections by neglecting the translational contributions to the total entropy in solution lead to underestimation of the relative free energies. High span energies were found using such corrections. Consequently, lower TOF are predicted with this method.

TOFs lying in the same order of magnitude as the optimal experiments were predicted for all the profiles obtained with the different DFT methods by using the Martin approach.

The use of entropic corrections by the Wertz and Ziegler methodology leads to TOFs exceeding the highest value obtained experimentally by one order of magnitude. However, exceptional matching was found for the B3LYP profile.

5.7 References and notes

- [1] C. J. Whiteoak, N. Kielland, V. Laserna, E. C. Escudero-Adán, E. Martin, A. W. Kleij, *J. Am. Chem. Soc.* **2013**, *135*, 1228.
- [2] a) S. Kozuch, S. Shaik, *Acc. Chem. Res.* **2010**, *44*, 101; b) S. Kozuch, *WIREs Comput. Mol. Sci.* **2012**, *2*, 795.
- [3] a) S. Kozuch, S. Shaik, *J. Am. Chem. Soc.* **2006**, *128*, 3355; b) S. Kozuch, S. Shaik, *J. Phys. Chem. A* **2008**, *112*, 6032; c) L. Yu, X. Pan, X. Cao, P. Hu, X. Bao, *J. Catal.* **2011**, *282*, 183.
- [4] a) A. Poater, X. Solans-Monfort, E. Clot, C. Copéret, O. Eisenstein, *J. Am. Chem. Soc.* **2007**, *129*, 8207; b) Z.-X. Yu, P. H.-Y. Cheong, P. Liu, C. Y. Legault, P. A. Wender, K. N. Houk, *J. Am. Chem. Soc.* **2008**, *130*, 2378; c) M. García-Melchor, M. C. Pacheco, C. Nájera, A. Lledós, G. Ujaque, *ACS Catal.* **2011**, *2*, 135; d) F. Nuñez-Zarur, X. Solans-Monfort, L. Rodríguez-Santiago, R. Pleixats, M. Sodupe, *Chem. Eur. J.* **2011**, *17*, 7506; e) S. Kozuch, J. M. L. Martin, *Chem. Commun.* **2011**, *47*, 4935; f) T. Mesganaw, A. L. Silberstein, S. D. Ramgren, N. F. F. Nathel, X. Hong, P. Liu, N. K. Garg, *Chem. Sci.* **2011**, *2*, 1766; g) T. G. Ostapowicz, M. Hölscher, W. Leitner, *Eur. J. Inorg. Chem.* **2012**, *2012*, 5632.
- [5] A. Uhe, M. Hölscher, W. Leitner, *Chem. Eur. J.* **2012**, *18*, 170.
- [6] M. J. Ajitha, C. H. Suresh, *Tetrahedron Lett.* **2011**, *52*, 5403.
- [7] Gaussian, Revision D.01, M. J. Frisch, G. W. Trucks, H. B. Schlegel, G. E. Scuseria, M. A. Robb, J. R. Cheeseman, G. Scalmani, V. Barone, B. Mennucci, G. A. Petersson, H. Nakatsuji, M. Caricato, X. Li, H. P. Hratchian, A. F. Izmaylov, J. Bloino, G. Zheng, J. L. Sonnenberg, M. Hada, M. Ehara, K. Toyota, R. Fukuda, J. Hasegawa, M. Ishida, T. Nakajima, Y. Honda, O. Kitao, H. Nakai, T. Vreven, J. A. Montgomery, Jr., J. E. Peralta, F. Ogliaro, M. Bearpark, J. J. Heyd, E. Brothers, K. N. Kudin, V. N. Staroverov, R. Kobayashi, J. Normand, K. Raghavachari, A. Rendell, J. C. Burant, S. S. Iyengar, J. Tomasi, M. Cossi, N. Rega, N. J. Millam, M. Klene, J. E. Knox, J. B. Cross, V. Bakken, C. Adamo, J. Jaramillo, R. Gomperts, R. E. Stratmann, O. Yazyev, A. J. Austin, R. Cammi, C. Pomelli, J. W. Ochterski, R. L. Martin, K. Morokuma, V. G. Zakrzewski, G. A. Voth, P. Salvador, J. J. Dannenberg, S. Dapprich, A. D. Daniels, Ö.

- Farkas, J. B. Foresman, J. V. Ortiz, J. Cioslowski, D. J. Fox, **2013**, Gaussian, Inc., Wallingford CT.
- [8] a) A. D. Becke, *J. Chem. Phys.* **1993**, *98*, 5648; b) C. Lee, W. Yang, R. G. Parr, *Phys. Rev. B* **1988**, *37*, 785.
- [9] Y. Zhao, D. Truhlar, *Theor. Chem. Acc.* **2008**, *120*, 215.
- [10] J.-D. Chai, M. Head-Gordon, *Phys. Chem. Chem. Phys.* **2008**, *10*, 6615.
- [11] P. J. Hay, W. R. Wadt, *J. Chem. Phys.* **1985**, *82*, 270.
- [12] *CRC Handbook of Chemistry and Physics*, D.R. Lide (ed), 84th Ed. CRC Press LLC, Florida **2003**.
- [13] R. Tanaka, M. Yamashita, L. W. Chung, K. Morokuma, K. Nozaki, *Organometallics* **2011**, *30*, 6742.
- [14] R. L. Martin, P. J. Hay, L. R. Pratt, *J. Phys. Chem. A* **1998**, *102*, 3565.
- [15] D. H. Wertz, *J. Am. Chem. Soc.* **1980**, *102*, 5316.
- [16] a) J. Cooper, T. Ziegler, *Inorg. Chem.* **2002**, *41*, 6614; b) G. Morales, R. Martínez, T. Ziegler, *J. Phys. Chem. A* **2008**, *112*, 3192.
- [17] A. Uhe, S. Kozuch, S. Shaik, *J. Comput. Chem.* **2011**, *32*, 978.
- [18] S. Grimme, *WIREs Comput. Mol. Sci.* **2011**, *1*, 211.
- [19] a) J. Hermans, L. Wang, *J. Am. Chem. Soc.* **1997**, *119*, 2707; b) Z.-X. Yu, K. N. Houk, *J. Am. Chem. Soc.* **2003**, *125*, 13825; c) Y. Chen, S. Ye, L. Jiao, Y. Liang, D. K. Sinha-Mahapatra, J. W. Herndon, Z.-X. Yu, *J. Am. Chem. Soc.* **2007**, *129*, 10773; d) Y. Liang, S. Liu, Y. Xia, Y. Li, Z.-X. Yu, *Chem. Eur. J.* **2008**, *14*, 4361; e) S. Qu, Y. Dang, C. Song, M. Wen, K.-W. Huang, Z.-X. Wang, *J. Am. Chem. Soc.* **2014**, *136*, 4974; f) M.-A. Courtemanche, M.-A. Légaré, L. Maron, F.-G. Fontaine, *J. Am. Chem. Soc.* **2014**, *136*, 10708.

UNIVERSITAT ROVIRA I VIRGILI

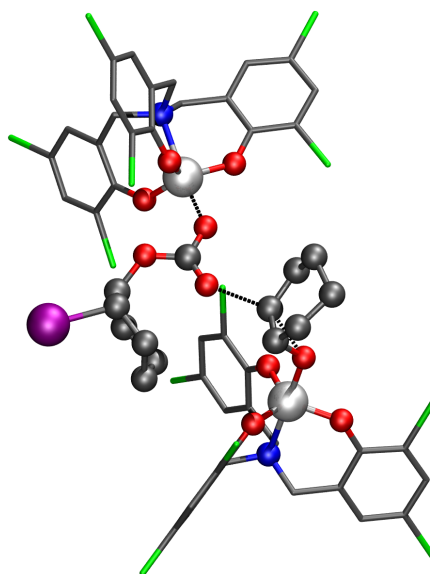
THEORETICAL STUDIES ON TRANSITION METAL CATALYZED CARBON DIOXIDE FIXATION

Fernando Simón Castro Gómez

Chapter 6

Aluminum Catalyzed Copolymerization of CO₂ and Cyclohexene Oxide

A detailed study on the mechanism for the alternating copolymerization of cyclohexene oxide (CHO) and CO₂ mediated by [Al{amino-tris(phenolate)}}]/NBu₄I binary system has been investigated using density functional theory (DFT) methods. Three potential mechanisms (one monometallic and two bimetallic) were considered for the first cycle of propagation of the CHO/CO₂ copolymerization, depending on the number of active Al-complexes involved in the reaction. For both bimetallic mechanisms, the isomerization of the linear carbonate intermediate in the initiation process was found to be rate-determining; whereas for the monometallic reaction, the epoxide ring-opening of the propagation was identified as the rate-determining step. Gibbs free energies calculated for the bimetallic reaction indicate that the alternating copolymerization was favored over the cyclic carbonate formation.

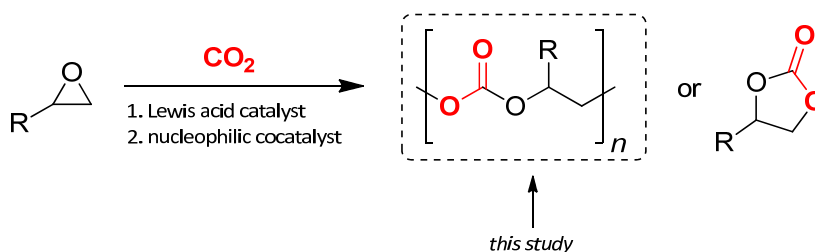


A manuscript including the results presented in this chapter is in preparation: F. Castro-Gómez, J. González-Fabra, A. W. Kleij, C. Bo, *in preparation*.

UNIVERSITAT ROVIRA I VIRGILI
THEORETICAL STUDIES ON TRANSITION METAL CATALYZED CARBON DIOXIDE FIXATION
Fernando Simón Castro Gómez

6.1 Introduction

The development of catalytic strategies enabling the use carbon dioxide (CO₂) as renewable and abundant C₁ source is of both academic and industrial relevance, yet remains as a challenging area.^[1] So far, there are only a limited number of efficient catalytic transformations that can overcome the low kinetic and high thermodynamic stability of the CO₂ molecule in order to generate valuable chemical products.^[2] Among of these transformations, the addition reaction of CO₂ into epoxides (Scheme 6.1) can lead to the formation of economically valuable polymers with useful properties.^[3] Aliphatic polycarbonates are considered a promising set of biodegradable polymers used as potential alternative for conventional engineering polymers; for preparing polyurethanes; and as elastomers for packaging material and coatings.^[4]



Scheme 6.1 The addition reaction of CO₂ to epoxides yielding poly- and cyclic-carbonates.

Many families of heterogeneous^[4e,5] and homogeneous^[6] catalyst systems have been used for the copolymerization of CO₂ and epoxides. The former are sluggish, present lower activity and/or selectivity, and operate under high CO₂ pressures; whereas the latter show better reactivity, with excellent activities and selectivities. Coates and coworkers^[6b] reported on the excellent activity of various Zn-based diketiminate complexes (β -diiminato) as substantial catalyst systems for mediating this reaction. A mononuclear mechanism for copolymerizing CO₂ and cyclohexene oxide (CHO) using Zn- β -diiminato catalysts was established *via* DFT calculations by Morokuma and coworkers; in that study the epoxide insertion was found to be the rate-determining step.^[7] Because of the Lewis acidity of Zn, some of these systems also catalyze the homopolymerization between epoxides, resulting in polyether impurities. However, earlier Zn-based catalysts have resulted in systems that provide polyether-free polycarbonate at low CO₂ pressures.^[5b,8] A combined experimental and computational investigation on the mechanism of CO₂/CHO

copolymerization using a dizing catalyst was published by Williams and coworkers.^[9] The authors determined the initiation and propagation reactions and identified the rate-determining step (i.e., the nucleophilic attack of the zinc-carbonate group on the epoxide); a close agreement between the calculated and experimental free energies was obtained.

Alternatively, porphyrins and salen complexes of aluminum, cobalt and chromium have also shown to efficiently catalyze the copolymerization reaction, either in the presence of a cocatalyst as nucleophile^[10] or bearing quaternary onium cation arms in the structure backbone allowing for bifunctionality.^[11] A concise computational review on the mechanism of polycarbonate formation from epoxides and CO₂ based on above catalysts has been recently published by Darensbourg and coworkers.^[12] In these studies emphasis was placed on the thermodynamics of polymer formation, and the kinetics of polymer growth and degradation. Despite some of the aforementioned catalysts have resulted in reasonably active systems for catalyzing the copolymerization, still need further improvements in both control of the selectivity, and in achieving high catalytic activity.

Recently, a new family of environmentally friendly catalysts based on aluminum(III) and iron(III) amino triphenolate complexes were reported to display remarkable activity and switchable selectivity in the conversion of a series of epoxides and oxetanes to cyclic carbonates^[13] and polycarbonates.^[14] Although very promising results were obtained with several substrates, the reaction of cyclohexene oxide with CO₂ lead to moderate conversions and generated a complex mixture of cyclic carbonates and polymeric species containing both carbonate and ether linkages. Cyclohexene oxide is an internal epoxide with substantial hindrance around the epoxide ring, which makes it a very challenging substrate for reaction with CO₂. Furthermore, the structure of cyclic cyclohexane carbonate contains a six-membered ring linked to a five-membered ring, and hence, is geometrically strained. This ring strain is probably the major factor which leads to the favorable production of copolymer instead of cyclic carbonate.^[15]

Herein, we present a detailed computational study on the mechanism for the copolymerization between CO₂ and CHO catalyzed by the [Al{amino-tris(phenolate)}]/NBu₄ binary system. Our study focuses on the description of the mechanistic steps involved in the copolymerization process, as well as the possible routes that can be followed by the catalytic reaction.

6.2 Motivation

In the preceding chapter we have established the (high) activity of the [Al{amino-tris(phenolate)}}/NBu₄I binary system as mediator for the formation of cyclic carbonate products from CO₂ and epoxides. Motivated by this outcome, we now turned our attention to the investigation of the mechanism operating for the copolymerization of CO₂ and epoxides. Since the cyclohexene oxide is the most successful substrate which leads to the favorable production of copolymer rather than cyclic carbonate, this epoxide was selected for performing our calculations.

To date, only few computational studies have been conducted towards mechanistic understanding of the CHO/CO₂ copolymerization.^[9,16] In those investigations, Zn-based complexes were employed as catalysts for the reaction, but nothing has been reported using aluminum complexes (at least, computationally).

Because of the above reasons, we become interested on explaining computationally the reaction mechanism for the alternating copolymerization of CO₂ and cyclohexene oxide mediated by the Al{amino-tris(phenolate)} catalyst.

6.3 Objectives

The main goal of the present study is to explore the reaction mechanism for the aluminium-catalyzed copolymerization of CO₂ and cyclohexene oxide through DFT calculations.

We will focus our attention on the thermodynamic description of the mechanistic steps for both the initiation process and the first cycle of propagation of the CHO/CO₂ alternating copolymerization. For this purpose, we will generate Gibbs free-energy profiles by calculation of all the intermediates and transition states involved in the reaction.

The last objective is to gain insights towards the favorability of achieving either the copolymer product or the thermodynamically stable cyclic carbonate from the Al-catalyzed addition of CO₂ to cyclohexene oxide.

6.4 Computational details

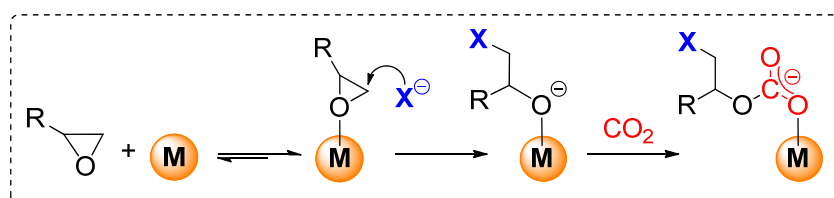
All calculations in this study were carried out using the Gaussian 09 package.^[17] It was employed the B97D3 functional,^[18] which includes empirical dispersion by Grimme. The

standard 6-311G(d,p) basis set was used to describe the H, C, N and O atoms. The relativistic effective core pseudo potential LANL2DZ was used, together with its associated basis set, for Al, Cl and I atoms. Full geometry optimizations were performed without constrains. The nature of the stationary points encountered was characterized either as minima or transition states by means of harmonic vibrational frequencies analysis. Gibbs free energies were calculated at standard conditions ($T=298.15$ K, $p=1$ atm). In order to introduce solvent effects, single point calculations were performed on the gas-phase optimized structures by using the polarizable continuum model (PCM). The dielectric constant (ϵ) of the polarizable medium was set to the value reported for the simplest epoxide, ethylene oxide ($\epsilon=12.42$),^[19] as the reaction takes place in the cyclohexene oxide rich phase. The 1-hexanol solvent was used for this purpose ($\epsilon=12.51$), as implemented in Gaussian.

6.5 Results

6.5.1 Understanding the mechanism of the copolymerization reaction

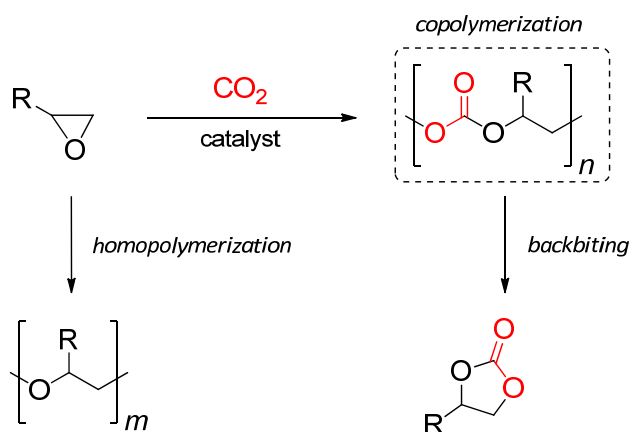
The type of copolymerization reaction studied herein begins with the coordination of an epoxide with a Lewis acid mediator. The epoxide substrate is activated by the Lewis acidic metal center and undergoes nucleophilic attack by a suitable initiator ligand (ring-opening step). Furthermore, a molecule of CO_2 reacts with the alkoxide intermediate formed in the previous step, leading to formation of a linear carbonate (Scheme 6.2).



Scheme 6.2 The initiation step for the general CO_2 /epoxide copolymerization reaction

Once the carbonate is formed, this serves as nucleophile for subsequent epoxide ring-opening reactions (copolymerization). Alternatively, two main side reactions can operate in the copolymerization of CO_2 and epoxides (Scheme 6.3), namely, the backbiting reaction

which yields to the thermodynamically stable cyclic carbonate, or consecutive insertion of epoxides allowing the formation of ether bonds in the copolymer (homopolymerization).



Scheme 6.3 Possible side reactions in the CO₂/epoxide copolymerization process.

Kleij and coworkers reported on the high activity presented by various iron(III) amino triphenolate complexes as mediators of the copolymerization between cyclohexene oxide (CHO) and CO₂.^[13] Recently, the Al{amino-tris(phenolate)} catalyst shown in Figure 6.1a has also demonstrated high power towards catalytic CHO/CO₂ copolymerization.

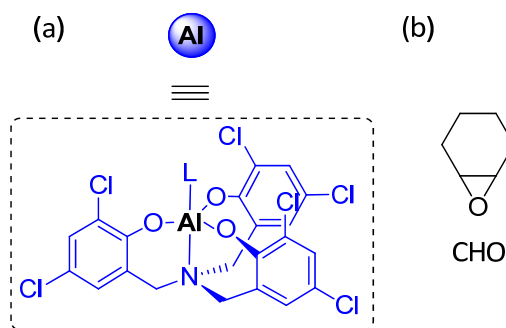


Figure 6.1 (a) Schematic drawing of the Al{amino-tris(phenolate)} catalyst used in this study; (b) cyclohexene oxide substrate.

In order to decrease the computational cost associated with the spin states of iron, in this thesis we focus on the investigation of the mechanism operating only for the copolymerization of CO₂ and CHO, based on the binary system catalyst composed of the [Al{amino-tris(phenolate)}] complex (Figure 6.1a), together with NBU₄ as cocatalyst.

We are currently conducting studies on the mechanism for the aluminum-catalyzed copolymerization of CO₂ and limonene oxide. Results on that investigation are not included in this thesis.

6.5.2 Initiation of the copolymerization reaction

The Figure 6.2 shows the free-energy profile obtained for the initiation process, as well as the barrier involved in the formation of the cyclic carbonate product. The starting point of the initiation reaction is the collective formed by four species: Al-complex + iodide + CHO + CO₂. Their total free energy is set to 0.0 kcal·mol⁻¹.

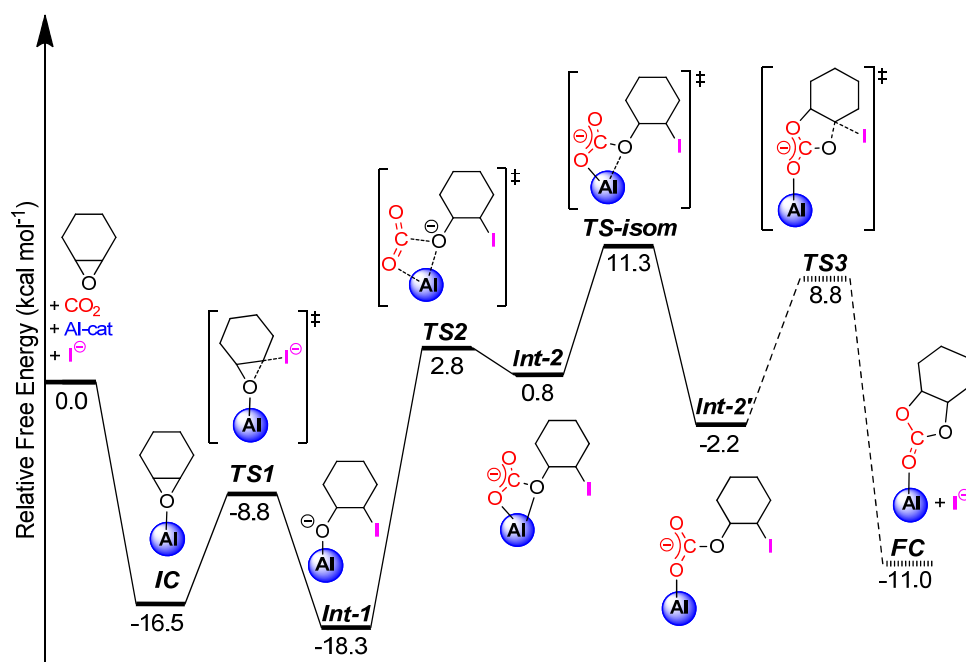


Figure 6.2 Free-energy profile for the initiation process of the CHO/CO₂ copolymerization catalyzed by the Al-complex/iodide binary system. The backbiting reaction for cyclic carbonate formation appears in dashed line.

As indicated above, the aluminum complex has the role of activating the CHO (by forming the initial complex, IC) towards nucleophilic attack by the halide anion affording the metal-alkoxide intermediate **Int-1**.

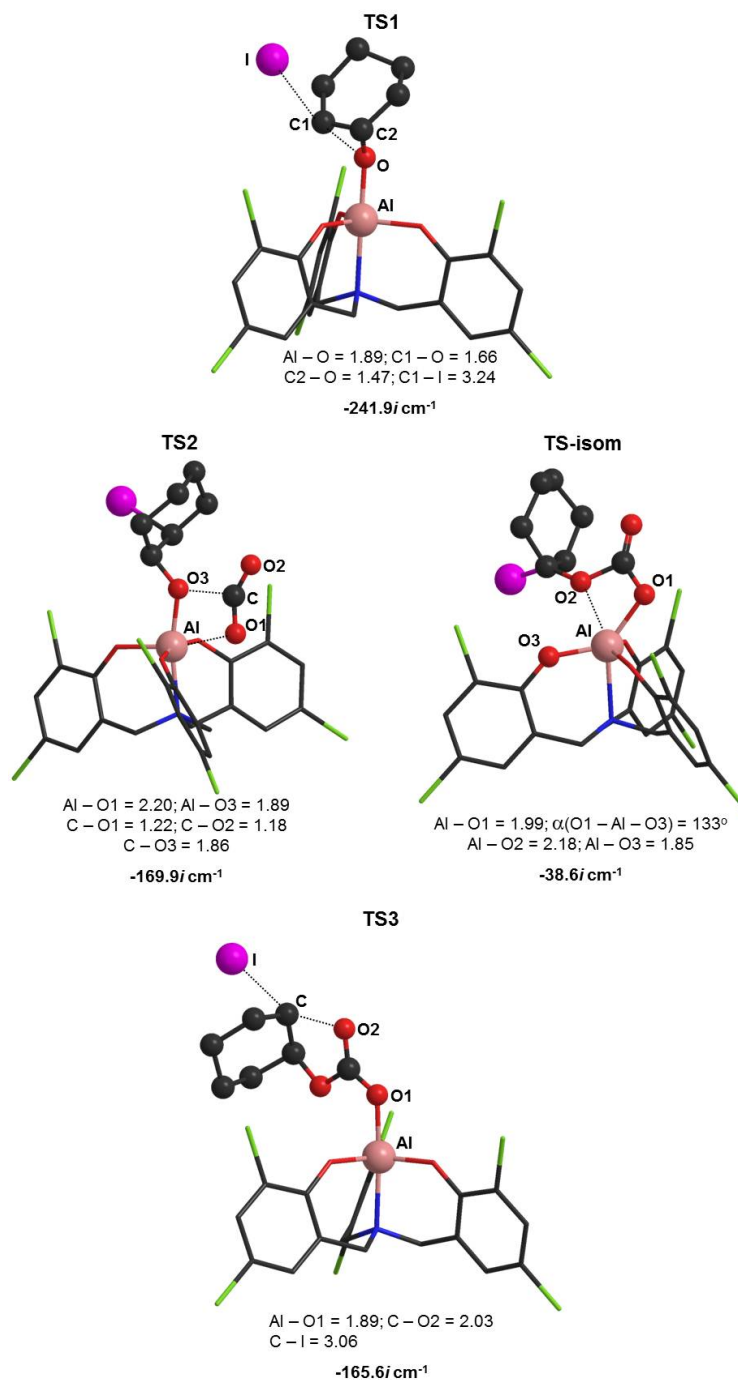
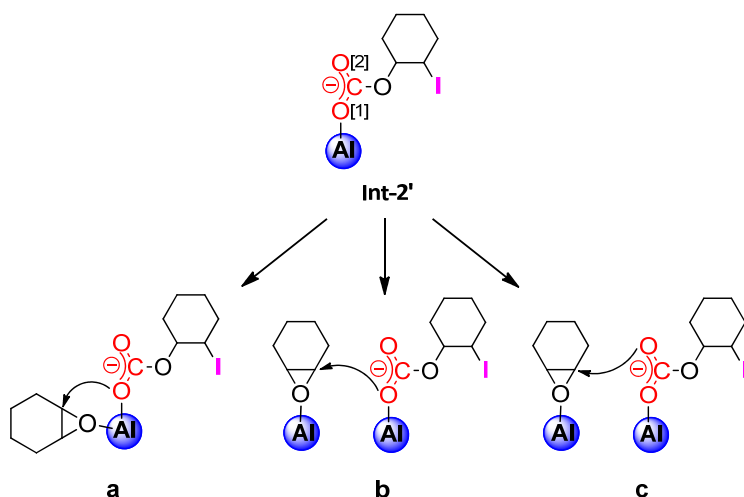


Figure 6.3 Optimized structures of the transition states **TS1–TS3** for the initiation process of the CHO/CO₂ copolymerization catalyzed by the Al-complex/iodide binary system, together with the most relevant calculated distances (in Å) and the values of the negative (imaginary) vibrational frequencies.

The epoxide ring-opening occurs *via* the concerted transition state **TS1** and implicates a barrier of 7.7 kcal·mol⁻¹. Then, the incoming CO₂ molecule is inserted into the metal-oxygen bond of the **Int-1**, through **TS2**, affording the linear carbonate **Int-2**. This step involves a free-energy barrier of 21.1 kcal·mol⁻¹. The intermediate **Int-2** suffers isomerization towards **Int-2'** through the transition state **TS-isom**. This process is the rate-determining step of the initiation reaction, with an activation barrier of 29.6 kcal·mol⁻¹ (calculated from **Int-1**). **TS-isom** results from the decrease of the angle $\alpha(\text{O1}-\text{Al}-\text{O3})$ shown in Figure 6.3.

At this point, two possible routes can be followed by the reaction: 1) backbiting of the linear carbonate **Int-2'**, giving the undesired cyclic carbonate formation or 2) consecutive insertion of the CHO and CO₂ monomers allowing for alternating copolymerization.

The backbiting reaction goes through the concerted transition state **TS3** (see dashed barrier in Figure 6.2), which is characterized by intramolecular ring-closing with concomitant release of the iodide nucleophile. This route has activation energy of 27.1 kcal·mol⁻¹, and leads to the formation of an intermediate complex having the *trans*-cyclohexene carbonate product coordinated to the Al-complex (**FC**).



Scheme 6.4 Possible routes for the propagation reaction of the copolymerization between CO₂ and cyclohexene oxide CHO, mediated by the Al-complex/iodide binary system.

In regards to the alternating copolymerization, three pathways could be possible once formed the intermediate **Int-2'** (Scheme 6.4). First, a monometallic mechanism is envisaged by means of the consecutive addition of a CHO monomer into the Al-center coordinative

vacancy, and the subsequent epoxide ring-opening due to nucleophilic attack of the oxygen bonded to the aluminum center (i.e., O[1] in Scheme 6.4).

The second and third copolymerization pathways involve bimetallic mechanisms. In these cases, either the oxygen bonded to the aluminum center or the carbonyl oxygen (O[1] and O[2], respectively) of the intermediate **Int-2'** shown in the Scheme 6.4, serve as nucleophile for opening the epoxide ring, and thus starting the first propagation cycle of the copolymerization reaction.

6.5.3 Propagation of the copolymerization reaction

In previous discussion we have described the mechanism for the initiation process of the CHO/CO₂ copolymerization, and held that once reached **Int-2'** the propagation might follow three different pathways. These latter are described in detail in further sections.

6.5.3.1 Monometallic mechanism

In Figure 6.4 is shown the free-energy profile including the first cycle of propagation for the copolymerization involving only one active aluminum center. The optimized structures of the transition states for this process are depicted in Figure 6.5.

The starting point of the monometallic propagation is the addition of a second CHO monomer into the aluminum center coordinative vacancy of **Int-2'** to form the adduct **IC-p**. The formation of this species implies a low barrier of 1.4 kcal·mol⁻¹, and is less energetically-demanding than the barrier for the backbiting reaction (**TS3**) by 9.6 kcal·mol⁻¹.

After formation of **IC-p**, the epoxide ring-opening occurs through nucleophilic attack of the carbonate oxygen O1 of the transition state **TS1-p** (Figure 6.5). As shown in Figure 6.5, the carbonate attack takes place from the bottom of the coordinated epoxide towards the carbon C and then an unstable twist-boat conformation can be observed for the cyclohexane substituent in the opened ring (**TS1-p**). This step yields the highest point on the free-energy profile (28.5 kcal·mol⁻¹). The epoxide ring-opening is rate-determining, involving a very high activation barrier of 46.8 kcal·mol⁻¹, calculated from the most stable intermediate of the initiation process (**Int-1**, in Figure 6.2, page 136).

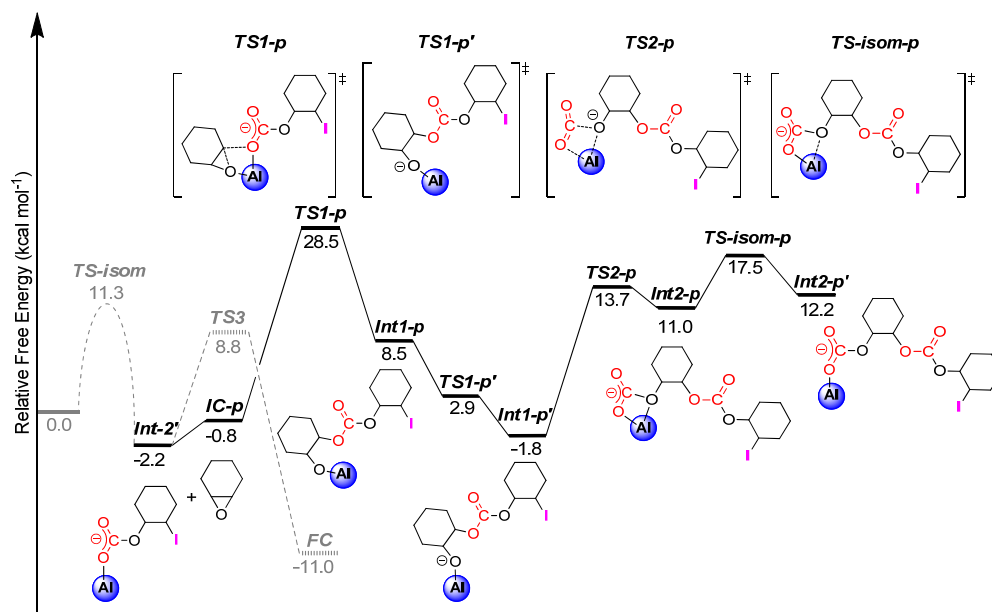


Figure 6.4 Free-energy profile for the first cycle of propagation of the monometallic copolymerization between CO₂ and CHO mediated by the Al-complex/iodide binary system. The barriers for the isomerization and backbiting reactions of the initiation process appear in gray dashed line.

Furthermore, the intermediate **Int1-p** can isomerize *via* **TS1-p'** affording a more stable species (**Int-1'**). The subsequent insertion of a second CO₂ monomer on the Al–O3 bond of **Int-1'** (**TS2-p**) leads to the formation of the poly(cyclohexene carbonate) **Int2-p**, which comprises a relative free energy of 13.7 kcal·mol⁻¹. Also, isomerization of this intermediate could be possible affording the product **Int2-p'**. As expected, this last isomer is thermodynamically less stable than the coordinated *trans*-cyclohexene carbonate (**FC**) by 23.2 kcal·mol⁻¹. It is worth noting that the poly(cyclohexene carbonate) formed in the monometallic copolymerization contains two different cyclohexane-substituent conformations (see **TS-isom-p** in Figure 6.5): one is the stable chair (that comes from the iodide attack in the initiation reaction) and another, the twist-boat (that comes from the attack of the carbonate oxygen O1 in the propagation). The above could explain the high energy found for the copolymer **Int2-p'**.

Since the proposed monometallic profile comprises high free-energy barriers for the propagation reaction (Figure 6.4), we should conclude that this mechanism might not operate for CHO/CO₂ alternating copolymerization.

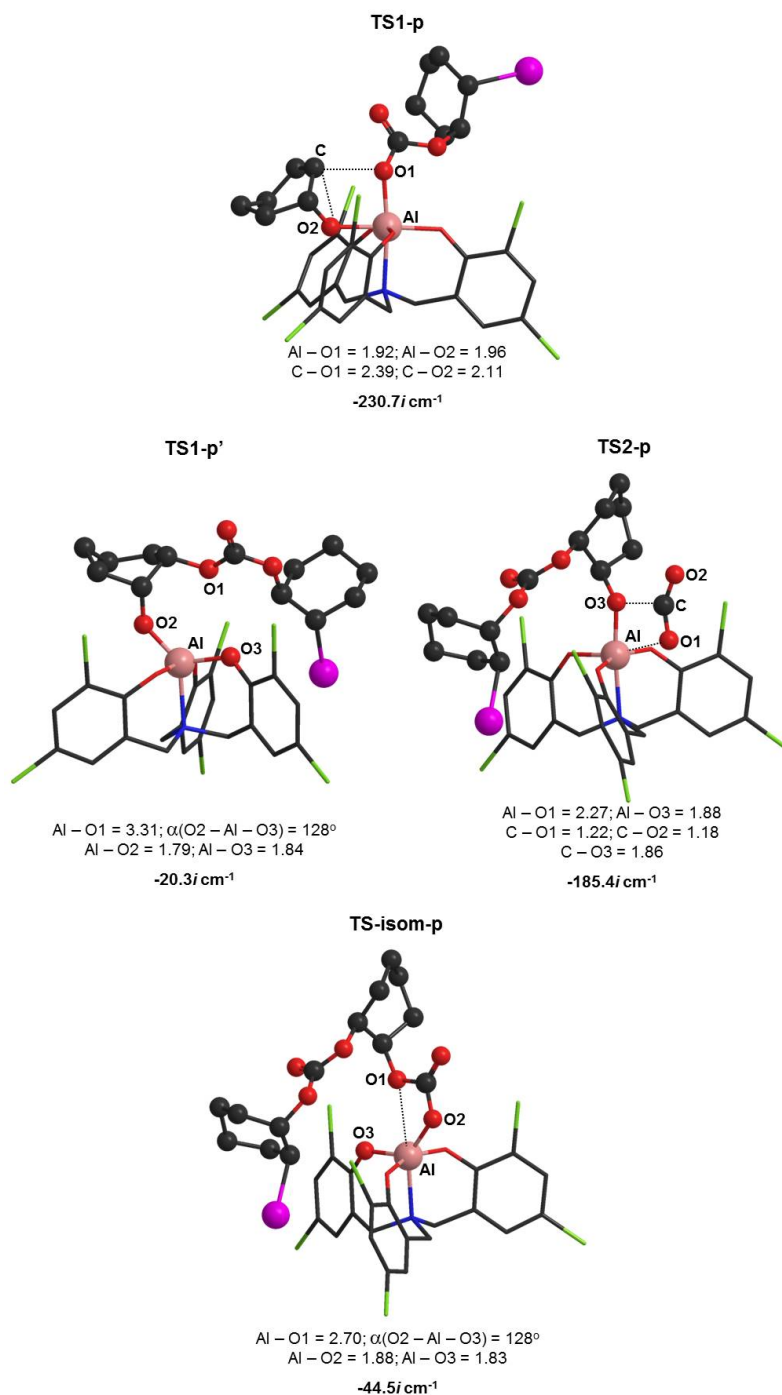


Figure 6.5 Optimized structures of the transition states **TS1-p**–**TS-isom-p** for the first cycle of propagation of the monometallic CHO/CO₂ copolymerization mediated by the Al-complex/iodide binary system. It is also shown the most relevant calculated distances (in Å), isomerization angle, and the values of the negative (imaginary) vibrational frequencies.

This result led us to the consideration of a second mechanism in which two active aluminum centers are capable of catalyzing the reaction.

6.5.3.2 Bimetallic mechanism based on the nucleophilic attack by the oxygen Al-O

The free-energy profile for the propagation reaction involving the bimetallic copolymerization of CO₂ and cyclohexene oxide is shown in Figure 6.6.

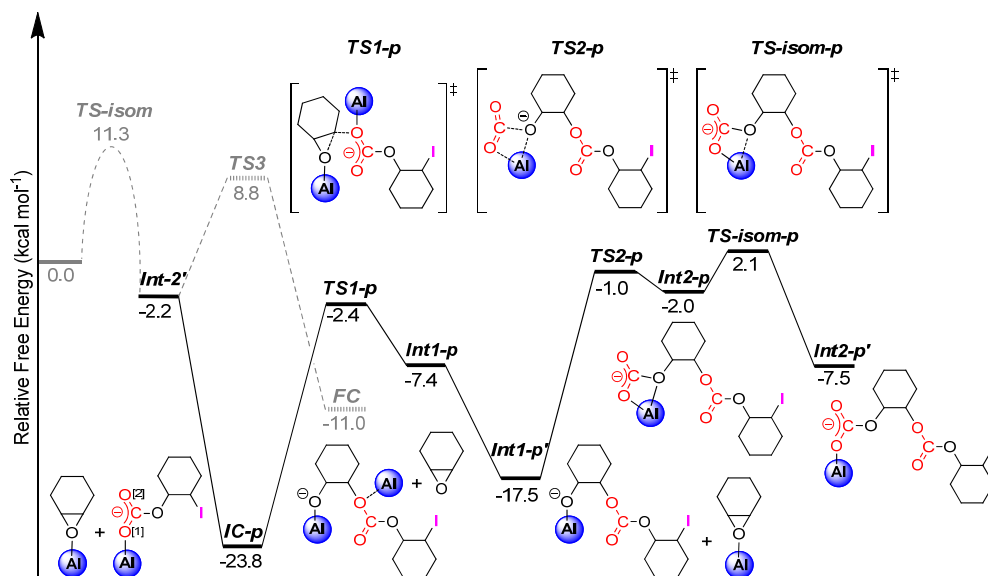


Figure 6.6 Free-energy profile for the first cycle of propagation of the bimetallic copolymerization between CO₂ and CHO mediated by the Al-complex/iodide binary system, and considering the nucleophilic attack by the oxygen bonded to the aluminum center (O[1]). The barriers for the isomerization and backbiting reactions of the initiation process appear in gray dashed line.

First, formation of a very stable adduct between the intermediate **Int-2'** and the complex having a CHO monomer coordinated to the Al-complex (**IC-p**), is observed. Natural bond orbital (NBO) population analysis on this complex affords small difference in the value of the charge assigned to the oxygen atoms of the carbonate **Int-2'**. Then, the oxygen bonded to the aluminium center (O[1]) exhibits a charge of -0.87; whereas the carbonyl oxygen (O[2]) shows a value of -0.69. This charge delocalization makes that the subsequent nucleophilic attack on the epoxide could occur by any of these two carbons.

In the mechanism described in this Section, the epoxide ring-opening is undertaken by nucleophilic attack of the oxygen bonded to the aluminum center in the intermediate **int-2'** (O[1]).

There is a substantial difference in energy between **IC-p** and the transition state **TS3**, with the former having relative energy of $-23.8 \text{ kcal}\cdot\text{mol}^{-1}$, while the latter has a relative barrier of $8.8 \text{ kcal}\cdot\text{mol}^{-1}$. The above indicates that the propagation of the CHO/CO₂ alternating copolymerization could be preferred over the formation of the coordinated *trans*-cyclohexene carbonate (**FC**) by $32.6 \text{ kcal}\cdot\text{mol}^{-1}$.

The epoxide ring-opening is conducted by the transition state **TS1-p**, which involves a total barrier of $21.4 \text{ kcal}\cdot\text{mol}^{-1}$ (with relative energy of $-2.4 \text{ kcal}\cdot\text{mol}^{-1}$). This structure is more stable than the transition state for the ring-closing reaction (**TS3**), which confirms the earlier trend towards the CHO/CO₂ alternating copolymerization, instead of cyclic carbonate formation. Unlike for the monometallic mechanism, in the bimetallic reaction, the nucleophilic attack takes place from the top of the coordinated epoxide towards the carbon C (see **TS1-p** in Figure 6.7), and then the stable chair conformation is observed for the cyclohexane substituent of the opened ring.

Once exceeded the barrier for **TS1-p**, the intermediate **Int1-p** is generated, in which both aluminum catalysts are still coordinated. The interaction between the oxygen of the alkoxide and the aluminium center in the complex (see Al1-O1 for **TS1-p** in Figure 6.7) is stronger than that observed for the oxygen of the coordinated carbonate **int-2'** (see Al2-O2 for **TS1-p** in Figure 6.7). Hence, it is proposed that **Int1-p** can evolve to the intermediate **Int1-p'** by releasing the Al-complex from the carbonate and allowing for new coordination with a third CHO monomer, thus generating the stable complex **IC** (having a relative energy of $-16.5 \text{ kcal}\cdot\text{mol}^{-1}$, according to Figure 6.2).

After formation of the alkoxide intermediate **Int1-p'**, the next step is the insertion of a second CO₂ monomer, *via* **TS2-p**, forming the poly(cyclohexene carbonate) **Int2-p**. The CO₂ insertion has an energy requirement of $16.5 \text{ kcal}\cdot\text{mol}^{-1}$. Then, **Int2-p** isomerizes to **Int2-p'** through a relative barrier of $2.1 \text{ kcal}\cdot\text{mol}^{-1}$ (**TS-isom-p**). The poly(cyclohexene carbonate) **Int2-p'** is more stable than the precedent isomer (**Int2-p**) by $6.5 \text{ kcal}\cdot\text{mol}^{-1}$, and in turn, less stable than the coordinated *trans*-cyclohexene carbonate (**FC**) by $3.5 \text{ kcal}\cdot\text{mol}^{-1}$.

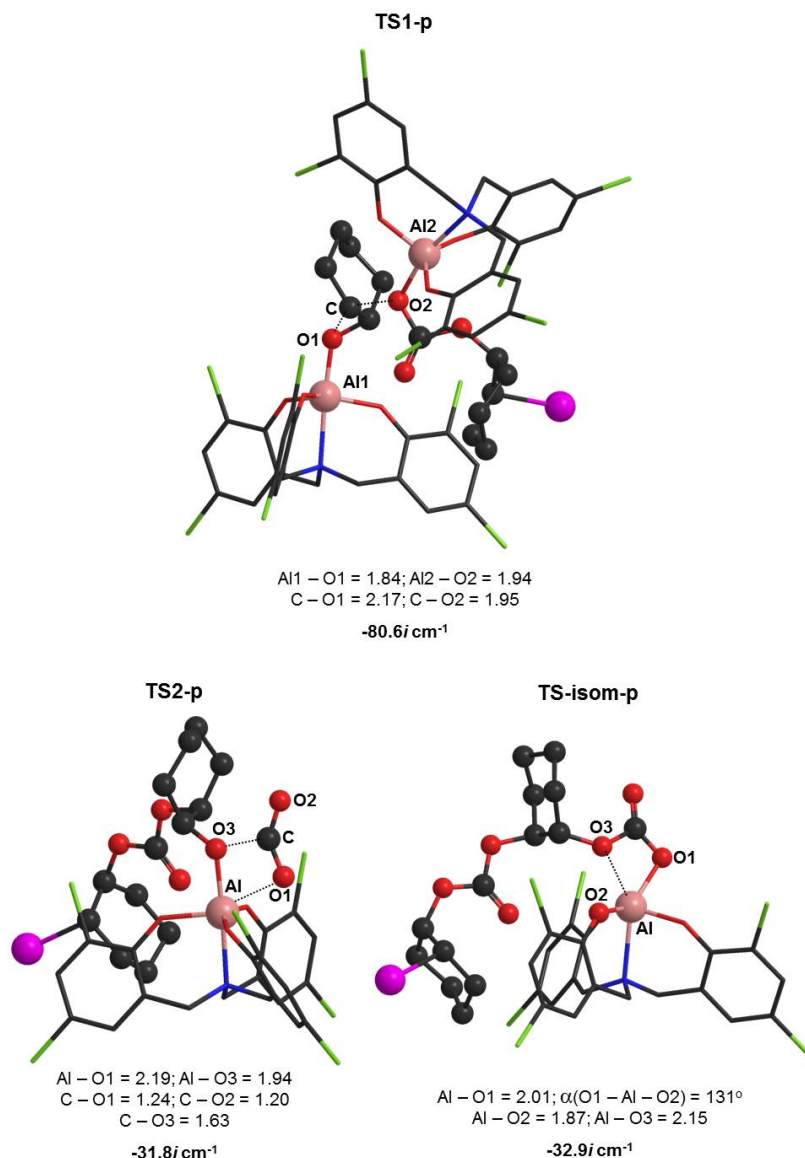


Figure 6.7 Optimized structures of the transition states **TS1-p**–**TS-isom-p** for the first cycle of propagation of the bimetallic CHO/CO₂ copolymerization mediated by the Al-complex/iodide binary system, and considering the nucleophilic attack by the oxygen bonded to the aluminum center. It is also shown the most relevant calculated distances (in Å), isomerization angle, and the values of the negative (imaginary) vibrational frequencies.

The above results, together the fact that all the relative barriers involved in the CHO/CO₂ alternating copolymerization are lower than that requires for the formation of the cyclic carbonate product, suggest that the former reaction could be the favored

pathway. Nevertheless, since slightly difference in the charge values for the carbonate oxygen of the adduct **IC-p** was found with the NBO population analysis, we now turned our attention to the study of a third mechanism involving the carbonyl oxygen attack for the propagation reaction.

6.5.3.3 Bimetallic mechanism based on the nucleophilic attack by the oxygen C=O

Figure 6.8 illustrates the free-energy profile for the propagation reaction comprising bimetallic copolymerization of CO₂ and cyclohexene oxide taking into account the nucleophilic attack of the carbonyl oxygen (O[2]) in the intermediate **int-2'**.

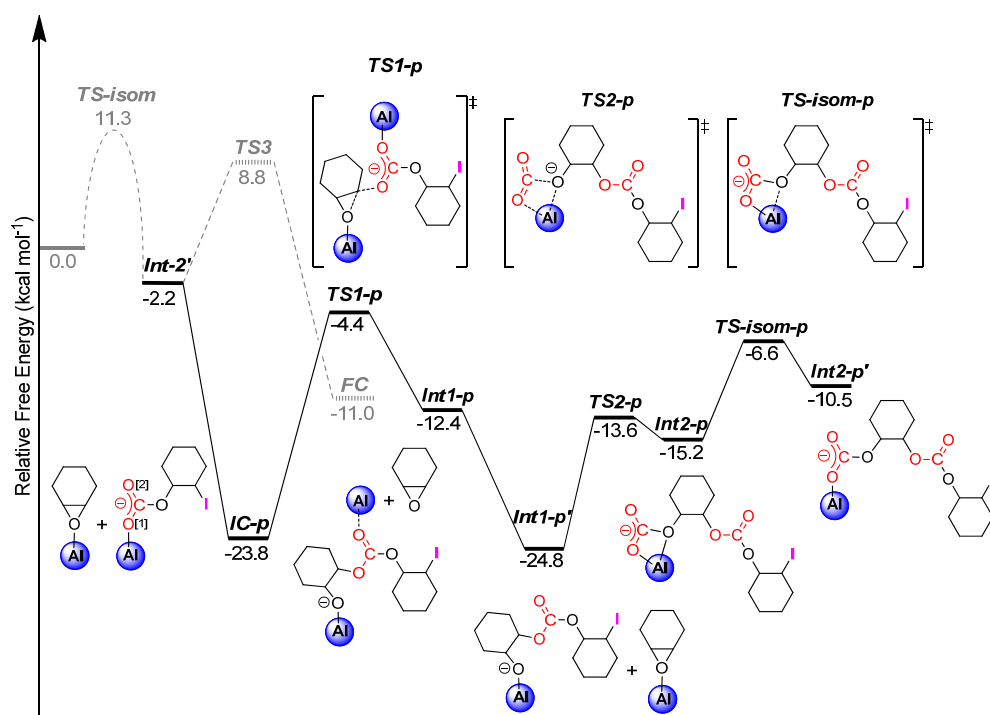


Figure 6.8 Free-energy profile the first cycle of propagation of the bimetallic copolymerization between CO₂ and CHO mediated by the Al-complex/iodide binary system, considering the nucleophilic attack by the carbonyl oxygen (O[2]). The barriers for the isomerization and the backbiting reactions of the initiation appear in gray dashed line.

Similar as for the bimetallic mechanism involving the oxygen bonded to the aluminum center (O[1]), the catalytic profile based on the carbonyl oxygen (O[2]) attack starts with the formation of the very stable adduct **IC-p**. Then, the epoxide ring-opening is mediated

by the transition state **TS1-p** illustrated in Figure 6.9. This step requires a slightly lower barrier (19.4 kcal·mol⁻¹) compared to the same step for the previous mechanism (21.4 kcal·mol⁻¹).

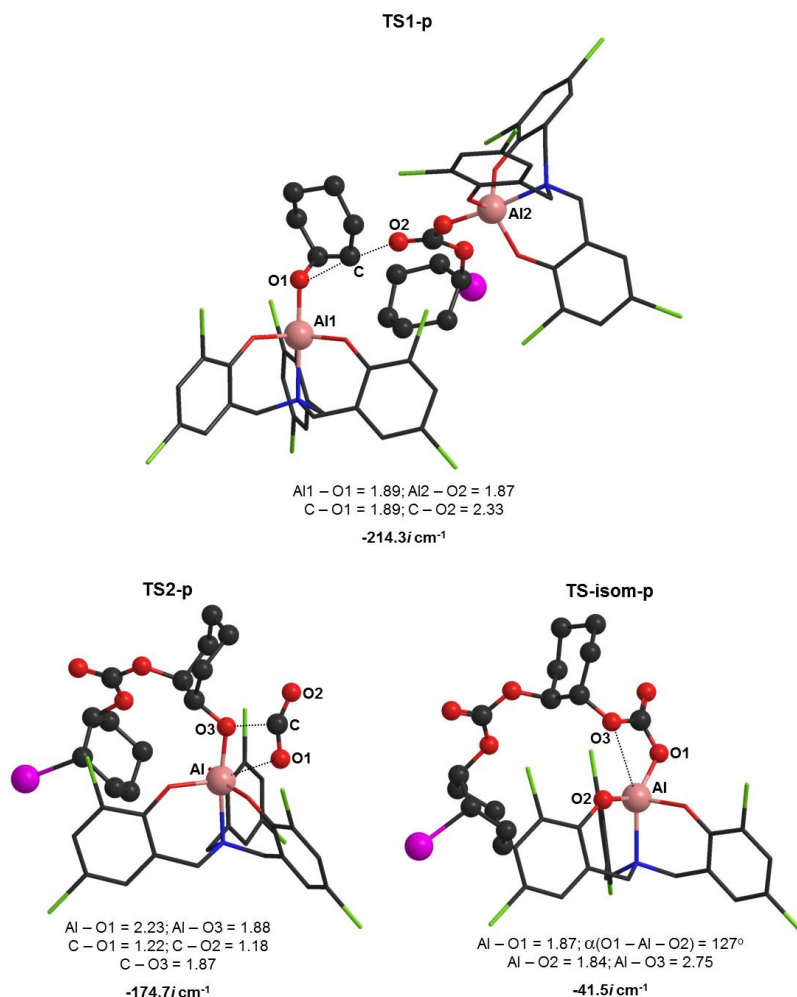


Figure 6.9 Optimized structures of the transition states **TS1-p**–**TS-isom-p** for the first cycle of propagation of the bimetallic CHO/CO₂ copolymerization mediated by the Al-complex/iodide binary system, and considering the nucleophilic attack by the carbonyl oxygen. It is also shown the most relevant calculated distances (in Å), isomerization angle, and the values of the negative (imaginary) vibrational frequencies.

The resulting alkoxide **Int1-p** is more stable than the corresponding intermediate derived from the attack of the oxygen O[1] by 5.0 (–12.4, –7.4) kcal·mol⁻¹, respectively. Also, it is suggested that the species **Int1-p** can lead to **Int1-p'** by releasing the carbonate

from the Al-complex, and subsequent coordination of the latter with a new CHO monomer. Hence, two species will be generated in this step: the alkoxide intermediate **Int1-p'** and the complex formed between the CHO monomer with the released Al-complex (**IC**).

The addition of a second CO₂ occurs through **TS2-p**, with a barrier of 11.2 kcal·mol⁻¹. The generated poly(cyclohexene carbonate) **Int2-p'** could isomerize to form the less stable species **Int2-p**. The energy difference between the isomer **Int2-p'** and the coordinated *trans*-cyclohexene carbonate (**FC**) is found to be very small by only 0.5 kcal·mol⁻¹, favoring the formation of the cyclic carbonate. It should be emphasized that isomer **Int2-p** is thermodynamically more stable than **FC** by 4.2 kcal·mol⁻¹, thus confirming the powerful activity of Al-complex/iodide binary system for mediating the CHO/CO₂ alternating copolymerization.

These results also demonstrate a clear trend towards alternating copolymerization of CHO and CO₂, which is reflected in the value of the relative barriers calculated.

6.6 Conclusions

The mechanism for the copolymerization of CO₂ and cyclohexene oxide (CHO) mediated by the binary [Al{amino-tris(phenolate)}]/NBu₄I catalyst system has been investigated and elucidated in detail by using DFT methods.

Two possible routes were described in the initiation process once formed the linear carbonate **Int-2'**, namely, the backbiting reaction giving the undesired cyclic carbonate formation, and the consecutive insertion of the CHO and CO₂ monomers allowing for alternating CHO/CO₂ copolymerization (propagation).

A monometallic mechanism was firstly investigated for the propagation reaction of the CHO/CO₂ copolymerization, in which a CHO monomer is inserted into the aluminum coordinative vacancy of the intermediate **Int-2'**, with subsequent epoxide ring-opening by the carbonate oxygen (Al-O) and addition of a new CO₂ molecule, generating the poly(cyclohexene carbonate). The second step (epoxide ring-opening) was found to be the rate-determining step of the monometallic propagation.

Two bimetallic mechanisms were also considered for the propagation, wherein either the oxygen bonded to the aluminum center or the carbonyl oxygen (O[1] and O[2], respectively) in the linear carbonate **Int-2'** act as nucleophile for the ring-opening of a CHO coordinated to the Al-complex (**IC**), followed by the addition of a CO₂ monomer, and thus leading to the formation of the poly(cyclohexene carbonate).

Calculations reveal that the isomerization of the linear carbonate **Int-2** to form **Int-2'** is the rate-determining step of the initiation reaction, and also for the bimetallic propagation.

In general, the free-energy barriers for the bimetallic propagation were found to be smaller than those obtained for the initiation reaction. The opposite effect was observed with the monometallic mechanism; thus suggesting that the alternating copolymerization take place through a bimetallic mechanism, which is the most favored pathway over the cyclic carbonate formation.

In all the cases, the obtained poly(cyclohexene carbonate) isomers **Int-2p'** resulted in species thermodynamically less stable than the coordinated *trans*-cyclohexene carbonate (**FC**), as expected. Interestingly, the isomer **Int2-p** of the bimetallic mechanism considering the carbonyl oxygen attack yields to a lower relative free-energy compared to **FC**.

6.7 References and notes

- [1] a) *Carbon Dioxide as Chemical Feedstock*, M. Aresta (ed), Wiley-VCH, Weinheim **2010**; b) M. Mikkelsen, M. Jørgensen, F. C. Krebs, *Energy Environ. Sci.* **2010**, *3*, 43; c) P. Markewitz, W. Kuckshinrichs, W. Leitner, J. Linssen, P. Zapp, R. Bongartz, A. Schreiber, T. E. Muller, *Energy Environ. Sci.* **2012**, *5*, 7281; d) T. Sakakura, J.-C. Choi, H. Yasuda, *Chem. Rev.* **2007**, *107*, 2365.
- [2] T. Sakakura, K. Kohno, *Chem. Commun.* **2009**, 1312.
- [3] a) R. Martín, A. W. Kleij *ChemSusChem* **2011**, *4*, 1259; b) M. Peters, B. Köhler, W. Kuckshinrichs, W. Leitner, P. Markewitz, T. E. Müller, *ChemSusChem* **2011**, *4*, 1216; c) M. Cokoja, C. Bruckmeier, B. Rieger, W. A. Herrmann, F. E. Kühn, *Angew. Chem. Int. Ed.* **2011**, *50*, 8510; D. J. Darensbourg, *Inorg. Chem.* **2010**, *49*, 10765.
- [4] a) G.-P. Wu, S.-H. Wei, W.-M. Ren, X.-B. Lu, T.-Q. Xu, D. J. Darensbourg, *J. Am. Chem. Soc.* **2011**, *133*, 15191; b) K. Nakano, S. Hashimoto, M. Nakamura, T. Kamada, K. Nozaki, *Angew. Chem. Int. Ed.* **2011**, *50*, 4868; c) D. J. Darensbourg, A. I. Moncada, S.-H. Wei, *Macromolecules* **2011**, *44*, 2568; e) G. A. Luinstra, *Polym. Rev.* **2008**, *48*, 192.
- [5] a) S. Klaus, M. W. Lehenmeier, C. E. Anderson, B. Rieger, *Coord. Chem. Rev.* **2011**, 255, 1460; b) M. R. Kember, A. Buchard, C. K. Williams, *Chem. Commun.* **2011**, 47, 141.
- [6] a) D. J. Darensbourg, *Chem. Rev.* **2007**, *107*, 2388; b) G. W. Coates, D. R. Moore, *Angew. Chem. Int. Ed.* **2004**, *43*, 6618; c) M. North, R. Pasquale, C. Young, *Green Chem.* **2010**, *12*, 1514.
- [7] Z. W. Liu, M. Torrent, K. Morokuma, *Organometallics* **2002**, *21*, 1056.
- [8] F. Jutz, A. Buchard, M. R. Kember, S. B. Fredriksen, C. K. Williams, *J. Am. Chem. Soc.* **2011**, *133*, 17395.
- [9] A. Buchard, F. Jutz, M. R. Kember, A. J. P. White, H. S. Rzepa, C. K. Williams, *Macromolecules* **2012**, *45*, 6781.
- [10] P. P. Pescarmona, M. Taherimehr, *Catal. Sci. Technol.* **2012**, *2*, 2169.
- [11] a) X. B. Lu, D. J. Darensbourg, *Chem. Soc. Rev.* **2012**, *41*, 1462; b) D. J. Darensbourg, S. J. Wilson, *Green Chem.* **2012**, *14*, 2665.

- [12] D. J. Darensbourg, A. D. Yeung, *Polym. Chem.* **2014**, *5*, 3949.
- [13] a) C. J. Whiteoak, E. Martin, M. Martínez Belmonte, J. Benet-Buchholz, A. W. Kleij, *Adv. Synth. Catal.* **2012**, *354*, 469; b) C. J. Whiteoak, B. Gjoka, E. Martin, M. Martínez Belmonte, E. C. Escudero-Adán, C. Zonta, G. Licini, A. W. Kleij, *Inorg. Chem.* **2012**, *51*, 10639; c) C. J. Whiteoak, N. Kielland, V. Laserna, E. C. Escudero-Adán, E. Martin, A. W. Kleij, *J. Am. Chem. Soc.* **2013**, *135*, 1228.
- [14] M. Taherimehr, S. M. Al-Amsyar, C. J. Whiteoak, A. W. Kleij, P. P. Pescarmona, *Green Chem.* **2013**, *15*, 3083.
- [15] D. J. Darensbourg, S. J. Lewis, J. L. Rodgers, J. C. Yarbrough, *Inorg. Chem.* **2003**, *42*, 581.
- [16] M. W. Lehenmeier, C. Bruckmeier, S. Klaus, J. E. Dengler, P. Deglmann, A. K. Ott, B. Rieger, *Chem. Eur. J.* **2011**, *17*, 8858.
- [17] Gaussian, Revision D.01, M. J. Frisch, G. W. Trucks, H. B. Schlegel, G. E. Scuseria, M. A. Robb, J. R. Cheeseman, G. Scalmani, V. Barone, B. Mennucci, G. A. Petersson, H. Nakatsuji, M. Caricato, X. Li, H. P. Hratchian, A. F. Izmaylov, J. Bloino, G. Zheng, J. L. Sonnenberg, M. Hada, M. Ehara, K. Toyota, R. Fukuda, J. Hasegawa, M. Ishida, T. Nakajima, Y. Honda, O. Kitao, H. Nakai, T. Vreven, J. A. Montgomery, Jr., J. E. Peralta, F. Ogliaro, M. Bearpark, J. J. Heyd, E. Brothers, K. N. Kudin, V. N. Staroverov, R. Kobayashi, J. Normand, K. Raghavachari, A. Rendell, J. C. Burant, S. S. Iyengar, J. Tomasi, M. Cossi, N. Rega, N. J. Millam, M. Klene, J. E. Knox, J. B. Cross, V. Bakken, C. Adamo, J. Jaramillo, R. Gomperts, R. E. Stratmann, O. Yazyev, A. J. Austin, R. Cammi, C. Pomelli, J. W. Ochterski, R. L. Martin, K. Morokuma, V. G. Zakrzewski, G. A. Voth, P. Salvador, J. J. Dannenberg, S. Dapprich, A. D. Daniels, Ö. Farkas, J. B. Foresman, J. V. Ortiz, J. Cioslowski, D. J. Fox, **2013**, Gaussian, Inc., Wallingford CT.
- [18] a) S. Grimme, *J. Comp. Chem.* **2006**, *27*, 1787; b) S. Grimme, S. Ehrlich, L. Goerigk, *J. Comp. Chem.* **2011**, *32*, 1456.
- [19] *CRC Handbook of Chemistry and Physics*, D.R. Lide (ed), 84th Ed. CRC Press LLC, Florida **2003**.

Chapter 7

General Conclusions

The detailed conclusions for the theoretical studies conducted on this thesis have been included at the end of the corresponding chapter. Therefore, only the main conclusions drawn from these studies will be summarized in this chapter.

Regarding the application of the theoretical methods comprising IM-MS, we have been able to acquire insights towards structural information of the transition metal complexes studied by means of their collision cross sections (CCSs). The accuracy of those methods reached the same level as that for the experiments, which is supported by the excellent agreement between experimental and calculated CCSs. Unfortunately, isomeric resolution could not be achieved because of the similarity on size and shape of the different isomers used. Though, some improvement is envisioned by employing more bulky and sophisticated ligands.

On the other hand, the reaction mechanism for the fixation of CO₂ into epoxides catalyzed by Zn(salen)-derived complexes and NBu₄X (X=Br, I) has been described in detail using DFT methods. The ring-opening step was found to be most favorable at the unsubstituted carbon atom (β) of the simplest epoxides. For alkyl-substituted terminal epoxides, the reaction is controlled by steric factors; whereas for vinyl- and phenyl-substituted substrates, electronic factors were dominant. Our findings suggest that for the formation of cyclic carbonates from CO₂ and propylene oxide, the catalytic system involving the Zn-N₄(salen) complex is less active than the Zn(salphen) containing the “N₂O₂” Schiff base ligands. The computed DFT activation energies are qualitatively in line with the experimental results.

Alternatively, the mechanism for the catalytic formation of cyclic carbonates from CO₂ fixation to epoxides, based on the binary [Al{amino-tris(phenolate)}]/NBu₄ catalyst system, has been computationally elucidated. Unlike for the Zn(salphen) complex, in the case of

the aluminium catalyst, a hexacoordinated transition state is observed for the CO₂ insertion step, which leads to two likely pathways and helps to decrease the energy requirement of this step. In addition to evaluate solvent effects, we also have studied the influence of the entropy changes in solution using hybrid and dispersion-corrected functionals. The latter was considered in order to assess the activity of the catalytic system through calculation of turnover frequencies (TOFs), resulting in a considerable increment of the TOF values compared to those calculated without using such corrections. The calculated TOFs lie in the same order of magnitude as the experimental outcome.

Finally, three different mechanisms have been reported herein for the alternating copolymerization of CO₂ and cyclohexene oxide based on the binary [Al{amino-tris(phenolate)}]/NBu₄I catalyst system. Remarkable results were obtained employing two active Al-complexes (bimetallic mechanism). In the case of the monometallic mechanism, the epoxide ring-opening for the propagation reaction was found to be rate-determining; whereas for the bimetallic mechanisms, the CO₂ insertion was crucial for the initiation reaction. According to the barriers calculated for the bimetallic mechanisms, the alternating copolymerization should be the favorable pathway over the formation of the five-membered cyclic carbonate product.

Overall, the combination of the computational methodologies used in this thesis and the outcome from the experiments has provided new insights towards catalytic reactions involving CO₂ fixation. Moreover, excellent agreement between both areas was achieved herein.

UNIVERSITAT ROVIRA I VIRGILI

THEORETICAL STUDIES ON TRANSITION METAL CATALYZED CARBON DIOXIDE FIXATION

Fernando Simón Castro Gómez

UNIVERSITAT ROVIRA I VIRGILI
THEORETICAL STUDIES ON TRANSITION METAL CATALYZED CARBON DIOXIDE FIXATION
Fernando Simón Castro Gómez